

https://dspace.org/

Optimization of zinc oxide electron transport layer in organic photovoltaic cells by co-doping with magnesium & gallium

Matsoha, Teboho C.

2021
https://hdl.handle.net/10539/36630

Downloaded from a DSpace repository. https://dspace.org/



UNIVERSITY OF THE
WITWATERSRAND,
JOHANNESBURG

Optimization of Zinc Oxide Electron Transport Layer in Organic Photovoltaic Cells by Co-doping with Magnesium & Gallium.

By

TEBOHO C. MATSOHA
(B.Sc. Hons)

A thesis submitted in partial fulfilment of the requirements for the degree

MAGISTER SCIENTIAE

As applicable in the

School of Physics
University of the Witwatersrand

South Africa

Supervisor: Prof O.M. Ntwaeaborwa
Co-Supervisors: Prof N. Moloto & Prof D. Wamwangi

Keywords

Zinc oxide, organic Solar Cells, Electron Transport Layer, Photovoltaics, Doping, Solution Processing, Power Conversion Efficiency, Nanoparticles.

Abstract

Organic solar cells show a remarkable combination of rapid improvement in performance and low cost which has led to much attention as a potential renewable energy competitor to traditional silicon cells. When metal oxides such as ZnO are introduced to these devices either as stand-alone electron transport layers or mixed with the active layer to facilitate electron transport, improvements in the performance arises through enhanced exciton dissociation and improved charge transport capabilities. In this study, to further improve the intrinsic properties of ZnO, magnesium and gallium dopants were incorporated into ZnO and their effects on the structure, particle morphology, optical and photoluminescence properties were analyzed.

Nanoparticles of ZnO were successfully synthesized using the sol-gel technique and then annealed at 500°C in a furnace. X-ray diffraction of the nanoparticles matched the peak positions of the samples to the hexagonal wurtzite structure of ZnO as indexed using ICSD card no. 180052. SEM and TEM have shown that the particle morphology comprises of rod-like structures which agglomerated to form nanoflowers. However, the Mg doped ZnO exhibited a deviant agglomerated nanosphere morphology. Energy Dispersive Spectroscopy revealed the weight percentages of the individual atoms in the nanoparticle and EDS mapping showing a non-homogeneous atomic composition distribution over the nanoparticles independent of their morphology. Raman spectroscopy measurements corroborated the structural phase identified by XRD having exhibited the vibrational modes associated with a wurtzite phase of ZnO. Nanoparticles sizes were found to increase upon annealing from room temperature to 500°C while the band gap decreased as the annealing temperature was increased from room temperature to 500°C.

Optical studies by diffuse reflectance confirmed band gap energies in the range of 3.11 – 3.18 eV for the annealed samples. An overall decrease in the band gap energies was observed upon annealing the samples from room temperature to 500°C and was attributed to the increase in crystallinity as observed from the sharpening of the X-ray diffraction peaks. Photoluminescence studies displayed both the characteristic near band emission (NBE) and broad band emission (yellow emission) from ZnO. The de-convoluted peaks of the broad emission band were associated with defect transitions such as zinc vacancies and oxygen interstitials.

At room temperature ZnO is diamagnetic as seen from the magnetic moment dependence on the applied field where the magnetic susceptibility is negative and can be estimated to have a magnetic permeability slightly less than 1. Temperature dependence of the induced moment in the presence of a magnetic field (20000 Oe) was evaluated. It was evident that upon annealing at higher temperature co-doped ZnO behaves like a diamagnetic material up to very low temperatures for which the incidence of super paramagnetism becomes apparent. This was seen when the experiment was repeated at a higher field, 2T, in which transition temperature shifted to higher values (4K).

The ZnO nanoparticles were then incorporated into organic solar cell as a constituent of the electron affinity layer as an acceptor. This was done by adding the nanoparticles to the active layer blend of P3HT:PCBM in the ratio 1:1 dissolved in chlorobenzene. In this way, the role of ZnO nanoparticles was to help in the electron extraction from the donor in the photoactive layer of the solar cell devices. The devices were then annealed to allow for interconnected network to form percolated layers. Raman spectroscopy analysis on the fabricated devices showed all modes associated with P3HT and micrographs depicted the distribution of nanoparticles over the surface of the devices. Absorption measurements gave spectra that were characterized by a broad absorption peak ranging from 438 – 570 nm with a maximum at 513 nm. A large decrease in the power conversion efficiencies was observed upon the introduction of the nanoparticles into the active layer blend. This drop can be attributed to the nanoparticles causing cracks probably due to differing particle sizes and non-homogeneous distribution which form alternative pathways for current to flow through the device, and they can also affect the contact between the active layer and the top aluminium electrode.

Acknowledgements

My most sincere gratitude goes to the School of Physics, University of the Witwatersrand and to the National Research Foundation for granting a scholarship that allowed me to pursue this degree. I would like to express my sincere thankfulness to my supervisors, Prof. M. Ntwaeaborwa, Prof. D. Wamwangi and Prof. N. Moloto for the roles each one of you played in guiding me through this journey and all the support you gave me. Your guidance, patience, encouragement, knowledge and critique were truly indispensable from the beginning to the end of this dissertation. I would also like to pass my gratitude to all research participants I met with in this journey, for their warm welcome into their labs as well as in their hearts.

Great thanks go to my family for the strength and patience they have shown throughout my whole time in graduate school. Their support has fueled the hardest climbs and has brought great comfort in times of difficulty. To my brother Mothebe, who has believed in me from the beginning and has been patient in teaching me how to conduct myself as a young man and to always be self- motivated to pursue my goals. To the most special woman in my life, Maleetse. You have been loving and caring and have always encouraged me to persist further beyond my limitations. I hope to be the person you see and believe in always. To my father, my hero and mentor. If I live my life to be but half the man you are and I will be truly content. I have respected your discipline and leadership from childhood to this day, I hope to make you very proud one day. To my Mother, your strength is why I am here today, for all this I am grateful.

A warm thank you to every role played by everyone not mentioned who also contributed to my development in one way or the other. I give thanks to the Almighty for blessing us each day with the gift of life, a chance to try again, to heal and to prosper.

Declaration

I (Teboho Matsoha) declare that the thesis hereby submitted by me for the master's degree at the University of the Witwatersrand is my own independent work and has not previously been submitted by me at another university/faculty. I furthermore, cede copyright of the thesis in favor of the University of the Witwatersrand.

Signature:……  ……..

Date:……04/10/2021……

Acronyms

AM	Air Mass
OSC	Organic Solar Cells
OPV	Organic Photovoltaics
XRD	X-ray Diffraction
HR-TEM	High Resolution Transmission Electron Microscopy
SEM	Scanning Electron Microscopy
EDS	Energy Dispersive X-ray Spectroscopy
PL	Photoluminescence
UV-Vis	Ultra Violet-Visible
eV	Electron Volts
FWHM	Full Width at Half Maxima
P3HT	Poly(3-hexylthiophene - 2,5 - diyl) regioregular
PCBM	[6,6] – phenyl – C_{61} – butyric acid methyl ester
PEDOT	Poly(3,4-ethylenedioxythiophene)
PSS	Poly(4-styrenesulfonate)

Table of Contents

Keywords 2
Abstract 3
Acknowledgements 5
Declaration 6
Acronyms 7
List of Figures 11
List of Tables 16
Chapter 1 17
1.1. Introduction 17
1.2. Motivation of this project/study 21
1.3. Statement of the problem 22
1.4. Research Aim 23
1.5. Research Aim 23
1.6. Thesis Layout 23
References 24
Chapter 2 - Literature Review 28
2.1. Introduction 28
2.2. Working Principle of Organic Solar Cells 28
2.3. Architecture of Bulk Heterojunction Devices 29
2.4. Zinc Oxide (ZnO) 31
2.4.1. Structure and Physical Properties 31
2.4.2. Electronic Band Structure and Optical Properties 33
2.4.3. ZnO Intrinsic Defects 35
Oxygen Vacancies 36
Zinc Vacancies 36
Oxygen Interstitials 37
Zinc Interstitials 37
Zinc Antisites 37
Oxygen Antisite 38
2.5. Phonon modes in Wurtzite ZnO 38

2.6. Doping of ZnO 41
2.6.1. Magnesium doping in ZnO 41
2.6.2. Gallium doping in ZnO 42
2.7. Photovoltaic parameters measurement 42
References 47
Chapter 3 – Material Preparation and Experimental Techniques 54
3.1. Introduction 54
3.2. Synthesis of Undoped and doped ZnO 54
3.3. Characterization Techniques 56
3.3.1. X-ray Diffraction 56
3.3.2. Raman Spectroscopy 60
Radiation source 60
Filters 61
Sample (Raman) Tube 61
Spectrograph 61
3.3.3. Transmission Electron Microscopy (TEM) 62
3.3.4. Scanning Electron Microscopy (SEM) 63
3.3.5. Energy-Dispersive X-ray Spectroscopy (EDS) 64
3.3.6. UV-Visible Spectrometry (UV-Vis) 65
3.3.7. Photoluminescence Spectroscopy 67
3.3.8. Physical Property Measurement System (PPMS) 69
References 71
Chapter 4 – Structural, Optical and Morphological Characterizations of Mg/Ga co-doped ZnO nanoparticles 74
4.1. Introduction 74
4.2. Morphological Studies 74
4.2.1. Scanning Electron Microscopy (SEM) 74
4.2.2. Energy Dispersive Spectroscopy 75
4.2.3. Transmission Electron Microscopy 78
4.3. X-Ray Diffraction (XRD) 78
4.4. Raman Spectroscopy 87
4.5. UV-Visible Spectroscopy 90
4.6. Photoluminescence Measurement 93

4.6.1. Photoluminescence Life-time measurements.....94
Conclusion.....96
References.....97
Chapter 5 – Magnetic Properties of pristine ZnO and co-doped ZnO.....101
5.1. Introduction.....101
5.2. Pristine co-doped ZnO (un-annealed).....102
5.3. Magnetic properties of annealed co-doped ZnO......105
Conclusion.....108
References.....109
Chapter 6 – Effect of Mg-Ga Co-doped ZnO nanoparticles on the Photovoltaic Properties of P3HT:PCBM Based Organic Solar Cells.....111
6.1. Introduction.....111
6.2. Experimental.....111
6.2.1. Device Fabrication.....111
6.3. Raman Spectroscopy.....113
6.4. UV-Vis spectroscopy.....114
6.5. Photoluminescence spectroscopy.....115
6.6. Current density – Voltage (J-V) curves.....116
Conclusion.....121
References.....122
Chapter 7 - Conclusions and Future Work.....125
Future Work.....126

List of Figures

Figure 1.1 Chart showing annual global installations of new power sources in gigawatts; over time, new energy supplies will come from renewable sources like solar panels and wind turbines (by BloombergNEF).

Figure 1.2 Projected Renewable energy demand distribution across Africa in 2013 and by 2030.

Figure 1.3 The NREL solar efficiency chart from August 2019. Emerging PV technologies which include organic solar cells are highlighted and enlarged

Figure 1.4 Structure of a bulk heterojunction (BHJ) solar cell.

Figure 2.1 Working principle in organic BHJ solar cells.

Figure 2.2 Conventional and inverted geometry of BHJ solar cells.

Figure 2.3 Stick and ball representation of ZnO crystal structures.

Figure 2.4 A schematic representation of wutzite ZnO, showing the tetrahedral coordination of ZnO neighboring atoms and the hexagonal wurtzite lattice.

Figure 2.5 The wurtzite structure of ZnO with the lattice parameters *a* and *c* shown in (a), and the band structure of ZnO calculated using the HSE hybrid functional in (b).

Figure 2.6 Typical photoluminescence spectrum of ZnO.

Figure 2.7 Schematic diagram of intrinsic defects in ZnO.

Figure 2.8 Unpolarized Raman spectrum of bulk ZnO.

Figure 2.9 AM1.5G Solar Spectrum.

Figure 2.10 current density – voltage (J-V) characteristics of solar cell under illumination.

Figure 2.11 Current density Vs Voltage curve depicting how series and shunt resistances can be calculated.

Figure 3.1 Schematic diagram of sol-gel synthesis of powder samples.

Figure 3.2 Diffraction of x-rays by a crystal.

Figure 3.3 The geometry of an x-ray diffractometer.

Figure 3.4 The Bruker D2 Phaser Bench-top Diffractometer.

Figure 3.5 Schematic diagram of Raman spectrometer.

Figure 3.6 Transmission Electron Microscope.

Figure 3.7 Primary building blocks of a scanning electron microscope.

Figure 3.8 Illustration of processes occurring during energy dispersive spectroscopy.

Figure 3.9 Schematic diagram of a UV-visible spectrophotometer.

Figure 3.10 Cary 500 UV-Vis spectrophotometer used in the study.

Figure 3.11 Principle of photoluminescence spectroscopy.

Figure 3.12 Schematic diagram of PL instrumentation.

Figure 3.13 Horiba PL system used in this study.

Figure 4.1 SEM images of undoped ZnO, 3% Mg doped ZnO, 3% Ga doped ZnO and 3% co-doped ZnO samples.

Figure 4.2 EDS mapping of 3% co-doped ZnO.

Figure 4.3 EDS spectra of undoped ZnO, 3% Mg doped ZnO, 3% Ga doped ZnO and 3% co-doped ZnO.

Figure 4.4 TEM images of undoped and 3% co-doped ZnO.

Figure 4.5 As prepared ZnO and ZnO annealed at 500°C XRD pattern stacked by Y offset.

Figure 4.6 XRD patterns of as prepared and 3% Mg doped ZnO with both samples annealed at 500°C.

Figure 4.7 XRD patterns of as prepared and 3% Ga doped ZnO with both samples annealed at 500°C.

Figure 4.8 XRD patterns of as prepared and 3% co-doped ZnO with both samples annealed at 500°C.

Figure 4.9 Sample Rietveld Refinement Run using FullProf Software.

Figure 4.10 Raman spectra of undoped ZnO, 3% Mg doped ZnO and 3% Ga doped ZnO all annealed at 500°C.

Figure 4.11 Raman spectra of undoped ZnO, and 3% co-doped ZnO both annealed at 500°C.

Figure 4.12 Diffuse reflectance plot of ZnO samples.

Figure 4.13 Bandgap energies of ZNO samples as deduced from the diffuse reflectance measurements.

Figure 4.14 Band gap energy Vs. annealing Temperature of ZnO undoped and doped samples.

Figure 4.15 Deconvoluted PL spectra of undoped and doped ZnO.

Figure 4.16 Energy diagram showing defect related transitions from ZnO samples in fig. 4.15.

Figure 4.17 Fluorescence decay measurements of 3% co-doped ZnO.

Figure 5.1 a) showing the magnetization dependence with temperature at 0.5T and b) 2T. It is evident that at room temperature pristine co-doped ZnO exhibit diamagnetic behavior.

Figure 5.2 a) Magnetization versus field dependence for pristine co-doped ZnO at 300 K. It is evident that the ZnO nanoparticles exhibit diamagnetic behavior even at higher applied fields. b) Isothermal magnetization versus field dependence curves for pristine co-doped ZnO at 2 K showing a mixed magnetic signatures of ferromagnetism with diamagnetic phases. The applied fields have been ramped between ±2 T.

Figure 5.3 Magnetization dependence on the temperature for co-doped ZnO upon cooling at 2T.

Figure 5.4 a) and b) Isothermal magnetization curves of co-doped ZnO annealed at 500C. At 2 K it is evident that the hysteresis depicts paramagnetic behavior owing to the lack of the coercive field.

Figure 6.1 Schematic diagram of layered device architecture.

Figure 6.2 Raman spectra of the reference, ZnO, Ga/ZnO and Mg-Ga/ZnO devices with inset showing Raman micrographs of the devices.

Figure 6.3 Absorbance measurements of fabricated devices.

Figure 6.4 ZnO nanoparticles incorporated P3HT:PCBM devices.

Figure 6.8 J-V curve for reference device. No sample added (P3HT:PCBM only).

Figure 6.9 J-V curve of ZnO:P3HT:PCBM.

Figure 6.10 J-V curve of 3% Ga/ZnO:P3HT:PCBM.

Figure 6.11 J-V curve of 3% Mg-Ga/ZnO:P3HT:PCBM.

Figure 6.12 Power conversion efficiencies of fabricated devices.

List of Tables

Table 2.1 Important physical properties of ZnO.

Table 2.2 Raman modes of ZnO and corresponding shift values.

Table 4.1 Crystallographic parameters extracted from XRD analysis of ZnO, as prepared and annealed at 500°C.

Table 4.2 Lattice parameters of 3% Mg doped ZnO samples.

Table 4.3 Lattice parameters of 3% Ga doped ZnO samples.

Table 4.4 Lattice parameters of 3% co-doped ZnO samples.

Table 4.5 Elemental composition of ZnO samples.

Table 6.1 Summary of performance parameters for the fabricated devices.

Chapter 1

1.1. Introduction

In one way or the other, all energy sources have some negative impact on our environment. However, fossil fuels such as oil, coal and other non-renewable sources of energy do substantially more harm than renewable energy sources. Among other things, the harmful effects include water pollution, air contamination, disturbances to wildlife and habitat loss, not excluding public health, land use, and global warming emissions. Whenever the topic of climate change comes up, renewable sources of energy usually top the list of changes the world can implement to mediate the worst effects of rising temperatures. That is because renewable energy sources such as wind and solar do not emit directly the greenhouse gases that contribute to global warming effects [1]. Figure 1.1 shows a chart of projected annual installations of new power sources in gigawatts. From the figure it is clear that there is an increase in renewable energy installations while fossil fuel sources such as coal or gas become increasingly rare.

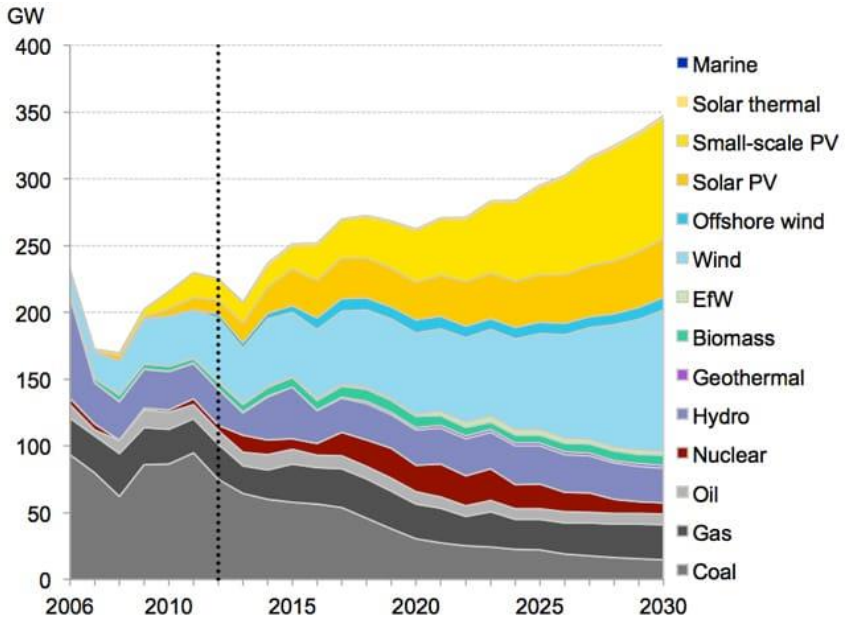

Figure 1.1. Chart showing annual global installations of new power sources in gigawatts; over time, new energy supplies will come from renewable sources like solar panels and wind turbines (by BloombergNEF [1]).

The maturing sector of renewable/clean energy is capable of creating jobs, reducing dependence of power from grids therefore minimizing chances of load shedding, and improving remote energy

access in African countries. Additionally, the flexibility as standalone technologies can mitigate the rising energy costs and energy bills at remote areas. A study carried out by the International Renewable Energy Agency (IRENA) suggests energy demand of up to 610 GW by 2030 with the southern part of Africa largely relying on distributed solar photovoltaic (PV) systems. This is depicted in the chart in figure 1.2 below [2]. For the past century, mankind has relied heavily on non-renewable sources to power everything from light bulbs to factories[3]. Fossil fuels play a crucial part in nearly all our energy demands and, as a result, the greenhouse gases emitted from the burning of those fuels have risen to historically new levels. Heat that would otherwise escape to outer space as a result of these gases is trapped in the atmosphere causing the average temperature on the surface of the earth to rise by up to 1.1°C by the year 2100[4].

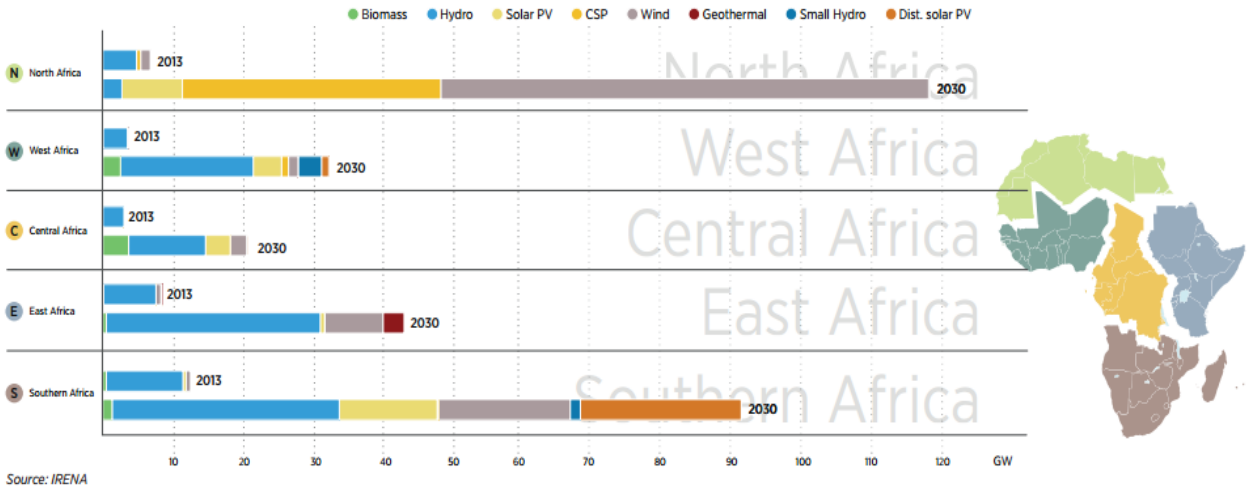

Figure 1.2. Projected Renewable energy demand distribution across Africa in 2013 and by 2030.[2]

In an effort to reduce the effect of these climate changes by replacing non-renewable sources with renewable sources, the photovoltaic industry have made huge advancements in the past decade to improve the performance of renewable energy devices. In particular, organic photovoltaic cells (OPVs) have attracted a great deal of attention as possible alternatives to their inorganic counterparts (Silicon and Cadmium Telluride) [5] based solar cells. Figure 1.3 depicts the National Renewable Energy Laboratory (NREL) solar efficiencies as of August 2019. The diagram shows that between 2000 and 2020 the efficiency of organic solar cells has increased considerably from ~4 to ~17%.

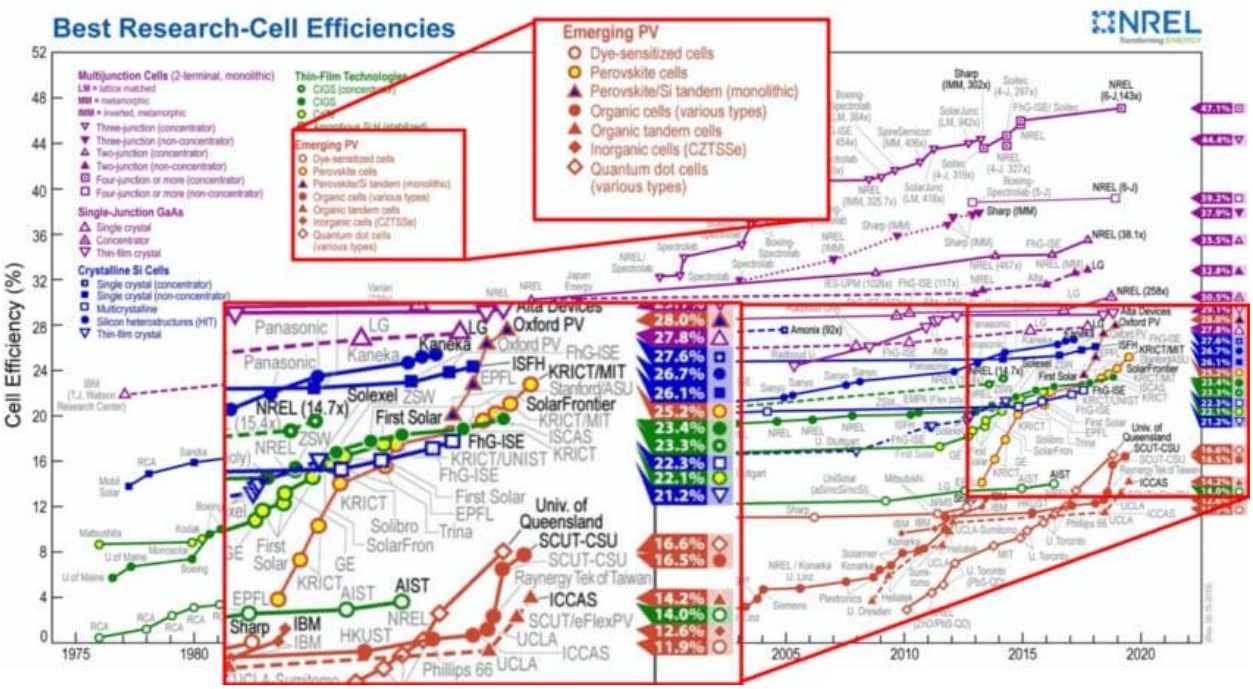

Figure 1.3 The NREL solar efficiency chart from August 2019. Emerging PV technologies which include organic solar cells are highlighted and enlarged [6]**.**

Bulk heterojunction based OPVs are photovoltaic devices that use two electronically dissimilar conductive organic polymers or small organic molecules for light absorption, exciton generation and charge transport to produce electricity [7]. Currently, the reported solar conversion efficiency of this generation of PV cell is ≥16% [8]. The high solar conversion efficiency is attributed to recent research on new acceptor molecules that are non-fullerene based. Additionally, the incorporation of a third organic polymer to form a ternary bulk heterojunction has reportedly attracted intensive research interests since the third component increases the overlap of the absorption with solar emission spectrum [9]. Despite these enormous efforts towards low cost solution-processable organic based PV devices, their performance parameters such as efficiency and lifetime are significantly lower when compared to the commercially viable inorganic photovoltaics in which the reported efficiencies of the conventional silicon solar cells are in the range of 15 - 40%[10]. To date, there are three types of OPVs, which are single layer, bilayer and the bulk heterojunction (BHJ) OPV devices, with the BHJ being the most efficient of the three. Therefore, only the BHJ is discussed in this study.

The basic architecture of the BHJ solar cell is shown in Figure 1.4. It comprises of a cathode, electron transport layer (ETL), active layer (electron donor and acceptor layer), hole transport layer

(HTL) and the anode. The active layer is the main component of the device where photo-excitation occurs, and the electrodes connect the cell to the outer circuit where there is a load[11]. The electron transport and hole transport layers improve the ohmic contact with electrodes as well as modifying the work function of the electrodes[12]. Since their discovery in the mid 1990's, BHJ solar cell, in which a mixture of polymer acceptor (e.g. P3HT) and fullerene (e.g. PCBM) is inserted as the active layer, has generated research interest worldwide due to continually demonstrating relatively high power conversion efficiencies (PCEs).

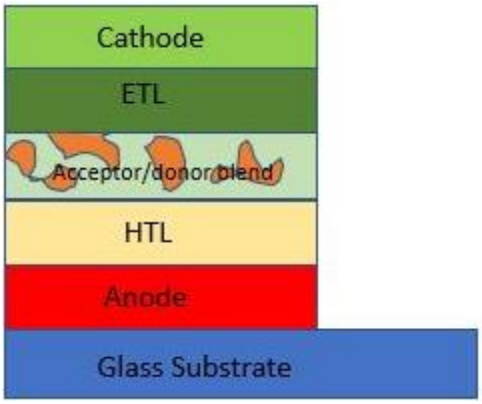

Figure 1.4 Structure of a Bulk Heterojunction Solar Cell

To improve the efficiencies of OPVs, various parameters can be investigated, these include but are not limited to, device geometry, particle morphology of metal oxide electron transporting layer inserted between the top electrode and photoactive layer and the sequence of thermal annealing [10]. In particular, the electron transport layer (ETL), has been manipulated in various ways in an attempt to improve their PCE by improving electron mobility to the cathode and also by protecting the active layer from photo-degradations such as those caused by oxygen and moisture penetrating through the device from the top electrode [13]. Doped metal oxides used as electron transport layers have previously shown improved device performance relative to their un-doped counterparts [14]. Interest has recently been shown in fabricating hybrid devices where the metal oxide used as the electron transport layer is blended together with the active layer components in an attempt to facilitate electron transport. This leads to chances of having reduced exciton recombination and shorter diffusion lengths for improved charge transport. This study focused on zinc oxide (ZnO),

a metal oxide semiconductor used in OPV as electron transport layer. The idea is to enhance the fundamental properties of ZnO through doping with magnesium (Mg) and gallium (Ga) and blending together with the active layer materials in order to enhance the efficiencies of BHJ organic solar cells. We expect the Mg/Ga doped ZnO nanoparticles to improve the electron accepting capability from the donor molecule of the photoactive layer.

1.2. Motivation of this project/study

Although the photoactive layer in OPV devices represents the major component and thus attracts a lot of attention due to its potential in improving the PCEs, other device layers such as the buffer layers (ETL and HTL) between the active layer and electrodes play a key role in the determination of the overall performance of the devices. These interface layers may, apart from enhancing the device performance, also help improve the overall stability of the devices [15]. Among the many ETL materials such as PbO and TiO_2, ZnO has shown great superiority due to its relatively high electron mobility, among other things. The n-type ZnO with its high electron mobility (200 cm^2/Vs) and a wide band gap (3.37 eV) allows for absorption of shorter wavelengths of the electromagnetic spectrum [16]. Furthermore, the electron acceptor molecule of the photoactive layer must have higher electron affinity and electron extraction capability. A comprehensive review of the structure and optical properties of ZnO has been reported by M. Kahouli et al [17]. Preference of ZnO over other wide band gap semiconductors as either electron transport layer or electron acceptor may include merits such as:

I. Transparent and highly conducting oxides – a property which is useful in applications such as transparent conducting electrode in photovoltaic cells;
II. Non-toxicity and availability in abundance – implying friendliness to the environment and cost effective production.
III. High resistance to the hydrogen plasma that is often used in the preparation of silicon based photovoltaic devices.
IV. High electron mobility
V. Absorption of UV photons that could otherwise cause photo-oxidation and degradation.

The ability to tune its electrical conductivity and optical absorption through tailoring the bandgap and adding impurities through simple doping methods further stamps on the nobility of this metal oxide [18].

When doped with group II and III elements such as magnesium (Mg) and Gallium (Ga), the optical and electrical properties of ZnO can be enhanced [19]. When doped with magnesium, the band gap of ZnO can be altered therefore allowing the semiconductor to be used in a variety of applications including solar cells, displays and light emitting diodes [20]. Also, due to the comparable size of the ionic radius of Mg^{2+} (0.57Å) and that of Zn^{2+} (0.6 Å), the inclusion of Mg in the lattice of ZnO does not cause significant distortion [20]. When Ga^{3+} is doped into ZnO, the Fermi level of ZnO increases making the injection of electrons to metallic electrode easier thus improving the electrical properties of ZnO [21]. The lengths of the covalent bonds of Ga–O and Zn-O are similar at 1.92 and 1.97Å respectively, and because the electronegativity's of Zn and Ga ions are close, it is expected that they form Ga–doped ZnO phase which brings about crystal defects [22]. Also, Ga^{3+} with ionic radius of 0.62Å is still comparable to that of $Zn^{2+}$and again no significant distortion of the lattice.

1.3. Statement of the problem

Lately, the design and development of electron acceptors in OPV devices is an important factor in improving the power conversion efficiency of the devices. While some researchers have resorted to non-fullerene molecules as electron acceptors due to low cost, optoelectronic tunability, and high thermal and chemical stability, the electron accepting capability of traditional fullerene molecules can be improved by blending with inorganic metal oxide nanoparticles such ZnO. This project set out to improve the power conversion and hence the general performance of the BHJ OPV devices by blending the P3HT:PBCM active layer with Mg-Ga co-doped ZnO nanoparticles. We expect the Ma-Ga doped ZnO to improve electron withdrawal from the polymer (P3HT) donor molecule, and also to improve the stability and reduce photo-degradation [23]. The BHJ OPVs of this nature hold a promise for higher efficiencies due to improved interface morphology of the active layer [24], among other things, and improved charge separation and transport. The choice of ZnO in these devices was based on the fact that it has got relatively high electron mobility and strongly absorbs photons in the UV which may cause photo-oxidation and degradation.

1.4. Research Aim

To investigate the structure, and physical properties of solution processed magnesium/ gallium doped zinc oxide nanoparticles and their effect as electron absorber on the PCE of BHJ OPV cells.

1.5. Research Aim

- To synthesize Mg/Ga doped ZnO nanoparticles using the sol-gel process.
- To examine the structure, particle morphology, optical, magnetic and luminescent properties of the Mg/Ga doped ZnO nanoparticles
- To evaluate the effect of the Mg/Ga ZnO nanoparticles when incorporated into the active layer of the BHJ OPV devices.

1.6. Thesis Layout

Chapter 2:

The literature review on organic photovoltaic cells working principles. It also highlights the theory of fundamental principles of ZnO and the role magnesium and gallium doping play in the improvement of its physical properties.

Chapter 3:

The chapter presents a theory behind the characterization techniques used in the study.

Chapter 4:

Reports the structure, particle morphological and optical properties of Mg/Ga doped ZnO synthesized by sol-gel method.

Chapter 5:

Discusses findings from magnetic measurements of pristine and co-doped ZnO

Chapter 6:

Discusses the device fabrication, characterization and current-voltage characteristics of organic solar cells incorporating ZnO nanoparticles.

Chapter 7:

Presents Conclusions and future work.

References

[1] "Environmental Impacts of Renewable Energy Technologies | Union of Concerned Scientists." https://www.ucsusa.org/resources/environmental-impacts-renewable-energy-technologies (accessed Jan. 18, 2020).

[2] IRENA, "A Renewable Energy Roadmap Report," *Irena*, no. June, p. 173, 2014, [Online]. Available: www.irena.org/remap.

[3] "Renewables sector challenges Eskom over load-shedding | ITWeb." https://www.itweb.co.za/content/KA3Wwqdl5ROqrydZ (accessed Jan. 18, 2020).

[4] S. A. Asongu, M. O. Agboola, A. A. Alola, and F. V. Bekun, "The criticality of growth, urbanization, electricity and fossil fuel consumption to environment sustainability in Africa," *Sci. Total Environ.*, vol. 712, Apr. 2020, doi: 10.1016/j.scitotenv.2019.136376.

[5] "Green Energy and Technology | SpringerLink." https://link.springer.com/bookseries/8059 (accessed Dec. 17, 2020).

[6] E. Welch, "First principle modeling of hybrid halide perovskites for optoelectronic applications," no. December, 2019.

[7] V. D. Mihailetchi, H. Xie, B. De Boer, L. J. A. Koster, and P. W. M. Blom, "Charge transport and photocurrent generation in poly(3-hexylthiophene): Methanofullerene bulk-heterojunction solar cells," *Adv. Funct. Mater.*, vol. 16, no. 5, pp. 699–708, 2006, doi: 10.1002/adfm.200500420.

[8] L. Meng *et al.*, "Organic and solution-processed tandem solar cells with 17.3% efficiency," *Science (80-.).*, vol. 361, no. 6407, pp. 1094–1098, Sep. 2018, doi:

10.1126/science.aat2612.

[9] T. Ameri, P. Khoram, J. Min, C. J. Brabec, and M. O. E. L. U. Mo, “Organic Ternary Solar Cells : A Review,” pp. 4245–4266, 2013, doi: 10.1002/adma.201300623.

[10] E. D. Using, “T Andem S Olar C Ells Deposited Using,” *Energy*, vol. 1, no. September, pp. 21–25, 2009.

[11] K. A. Vivek and G. D. Agrawal, “Organic Solar Cells : Design , Architecture and Novel Concepts,” *Energy Technol. Ecol. Concerns A Contemp. Approach*, pp. 87–91, 2015.

[12] M. Ikram, R. Murray, A. Hussain, S. Ali, and S. Ismat Shah, “Hybrid organic solar cells using both ZnO and PCBM as electron acceptor materials,” *Mater. Sci. Eng. B Solid-State Mater. Adv. Technol.*, vol. 189, pp. 64–69, 2014, doi: 10.1016/j.mseb.2014.08.005.

[13] A. Tournebize *et al.*, “Crucial Role of the Electron Transport Layer and UV Light on the Open-Circuit Voltage Loss in Inverted Organic Solar Cells,” 2017, doi: 10.1021/acsami.7b09059.

[14] S. Zheng, G. Wang, T. Liu, L. Lou, S. Xiao, and S. Yang, “Materials and structures for the electron transport layer of efficient and stable perovskite solar cells,” *Science China Chemistry*, vol. 62, no. 7. Science in China Press, pp. 800–809, Jul. 01, 2019, doi: 10.1007/s11426-019-9469-1.

[15] X. Huang, H. Yu, S. Shi, and C. Huang, “Improving the performance of inverted polymer solar cells by the efficiently doping and modification of electron transport layer-ZnO,” *Org. Electron.*, vol. 65, pp. 311–320, Feb. 2019, doi: 10.1016/j.orgel.2018.11.030.

[16] M. M. Ansari, M. Arshad, and P. Tripathi, “Study of ZnO and Mg doped ZnO

nanoparticles by sol-gel process," in *AIP Conference Proceedings*, Jun. 2015, vol. 1665, p. 050123, doi: 10.1063/1.4917764.

[17] M. Kahouli, A. Barhoumi, A. Bouzid, A. Al-Hajry, and S. Guermazi, "Structural and optical properties of ZnO nanoparticles prepared by direct precipitation method," *Superlattices Microstruct.*, vol. 85, pp. 7–23, 2015, doi: 10.1016/j.spmi.2015.05.007.

[18] A. Janotti and C. G. Van De Walle, "Fundamentals of zinc oxide as a semiconductor," *Reports Prog. Phys.*, vol. 72, no. 12, 2009, doi: 10.1088/0034-4885/72/12/126501.

[19] A. Alexandrov, M. Zvaigzne, D. Lypenko, I. Nabiev, and P. Samokhvalov, "Al-, Ga-, Mg-, or Li-doped zinc oxide nanoparticles as electron transport layers for quantum dot light-emitting diodes," *Sci. Rep.*, vol. 10, no. 1, pp. 1–11, 2020, doi: 10.1038/s41598-020-64263-2.

[20] M. Caglar, Y. Caglar, and S. Ilican, "Investigation of the effect of Mg doping for improvements of optical and electrical properties," *Phys. B Condens. Matter*, vol. 485, pp. 6–13, Mar. 2016, doi: 10.1016/j.physb.2015.12.049.

[21] H. H. Kim *et al.*, "Optimization of the electron transport in quantum dot light-emitting diodes by codoping ZnO with gallium (Ga) and magnesium (Mg)," *RSC Adv.*, vol. 9, no. 55, pp. 32066–32071, 2019, doi: 10.1039/c9ra06976c.

[22] A. Alexandrov, M. Zvaigzne, D. Lypenko, igor nabiev, and pavel Samokhvalov, "2 Laboratory of Electronic and Photonic Processes in Polymeric Nanostructural Materials, A.N. Frumkin Institute of Physical Chemistry and Electrochemistry of the Russian Academy of Sciences," vol. 115409, no. 3, 1190, doi: 10.1038/s41598-020-64263-2.

[23] V. I. Madogni, B. Kounouhéwa, A. Akpo, M. Agbomahéna, S. A. Hounkpatin, and C. N. Awanou, “Comparison of degradation mechanisms in organic photovoltaic devices upon exposure to a temperate and a subequatorial climate,” *Chem. Phys. Lett.*, vol. 640, pp. 201–214, 2015, doi: 10.1016/j.cplett.2015.09.023.

[24] S. R. Ferreira, R. J. Davis, Y. Lee, P. Lu, and J. W. P. Hsu, “Effect of device architecture on hybrid zinc oxide nanoparticle : poly (3-hexylthiophene) blend solar cell performance and stability,” *Org. Electron.*, vol. 12, no. 7, pp. 1258–1263, 2011, doi: 10.1016/j.orgel.2011.04.008.

Chapter 2 - Literature Review

2.1. Introduction

To meet the emerging need for sustainable energy, the production in large scales of cheap and easy to process solar cells is of utmost importance. This has necessitated the rapid development of carbon-based semiconductors (small molecules and conjugated polymers) for use in what is today known as organic photovoltaic cells (OPVs) for generation of clean and inexhaustible energy. These materials are characterized by efficient light absorption and other fundamental properties that can be tuned through chemical synthesis. Furthermore, the fabrication of the carbon-based photovoltaics is almost entirely solution processable [1] and therefore cost-effective.

There has been significant progress in organic photovoltaics in the past three decades. OPVs have numerous advantages such as high-throughput roll-to-roll solution processing, non-toxicity and potential to be an affordable technology which can compete with current photovoltaic technologies [2]. They are light in weight, can be fabricated on flexible plastic substrates [3], can be transparent or color-tunable, which makes them ideal integrated components for a wide variety of applications [4]. Although power conversion efficiencies (PCE) of more than 11% have been reported, a significant work needs to be done in order to translate lab-scale developments to the industrial scale [3]. Several strategies are being adopted in an attempt to attain higher PCEs such as, controlling the morphology of the active layer, implementing new device architectures, employing interfacial layers that serve as electron transport layers (ETL) and/or hole transport layer (HTL), fabricating hybrid devices by blending active layer and electron transport layer materials and synthesizing new donor and accepter materials.

2.2. Working Principle of Organic Solar Cells

Generally, the working principle of OPVs involves four fundamental steps; (i) absorption of photons to generate Frenkel excitons, (ii) diffusion and dissociation of the excitons at the donor :acceptor interface, (iii) charge transport and (iv) charge collection [2]. In bulk-heterojunction OPV, where the active layer is a blend of donor and acceptor materials, the incoming sunlight is absorbed by the electron donating material (donor), which in most cases is a conjugated polymer.

Photons excite electrons from the highest occupied molecular orbital (HOMO) to the lowest unoccupied molecular orbital (LUMO) of the donor material. Since the dielectric constant of OPV's is small, the excitation is mostly governed by Frenkel excitons with life-times in the range of nanoseconds [5]. Therefore, there should be an offset between the donor LUMO and the acceptor LUMO in the range of 0.1 – 1.4 eV [6] which is the driving force for effective exciton dissociation. The exciton then diffuses to the donor-acceptor interface where it dissociates to free charge carriers due to a potential energy gradient. The free charge carriers are then transported to their respective electrodes via bi-continuous interpenetrating pathways. These steps are illustrated in figure 2.1.

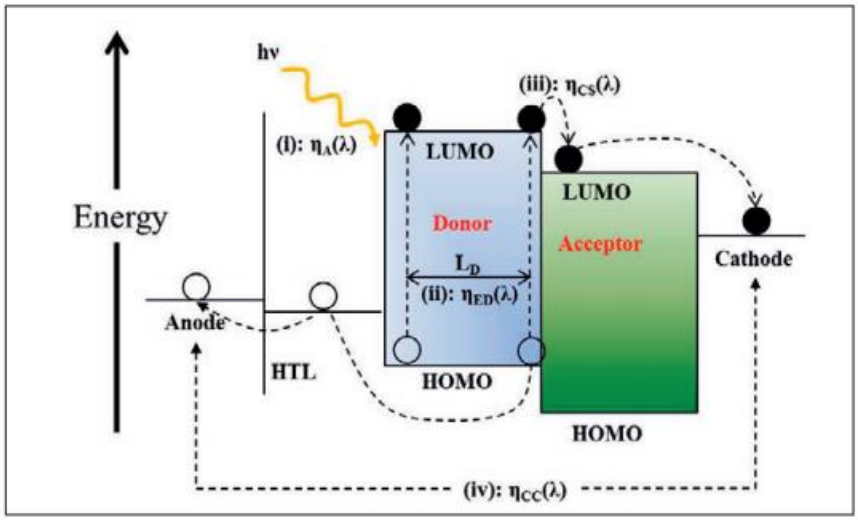

Figure 2.1. Working principle in Organic Heterojunction Solar Cells[4]

2.3. Architecture of Bulk Heterojunction Devices

Since the inception of OPVs, several materials and structures have been used in their design and fabrication in order to improve their stability and efficiency, and hence their general performance. When constructing a working Bulk Heterojunction (BHJ) solar cell, the photoactive layer commonly consisting of a blend of polymer and conjugate carbon derivate is the most important component of the BHJ solar cell. According to latest design, the standard BHJ OPV conventional geometry is comprised of an indium tin oxide (ITO) pre-coated glass substrate, a hole transport layer (usually PEDOT:PSS), the active layer (usually can be a blend of P3HT:PCBM), an electron transport layer (e.g. ZnO or TiO_2) and the top electrode (usually Ag or Al) [7]. In the inverted

geometry, an electron transport layer follows the ITO (cathode) which is then followed successively by the active layer, hole blocking layer, and either gold (Au, 5.1 eV) or silver (Ag, 5.0 eV) that serves as an anode in the top electrode. A conjugated polymer, PEDOT:PSS is commonly used for the hole blocking layer and TiO_2/ZnO for the electron transport layer. Figure 2.2 below depicts the (a) conventional and (b) inverted geometry of the BHJ OPV. The inverted OPV has been studied by several groups, owing to their compatibility with roll-to-roll processing on a large scale, avoiding costly vacuum deposition techniques required for the conventional geometry.

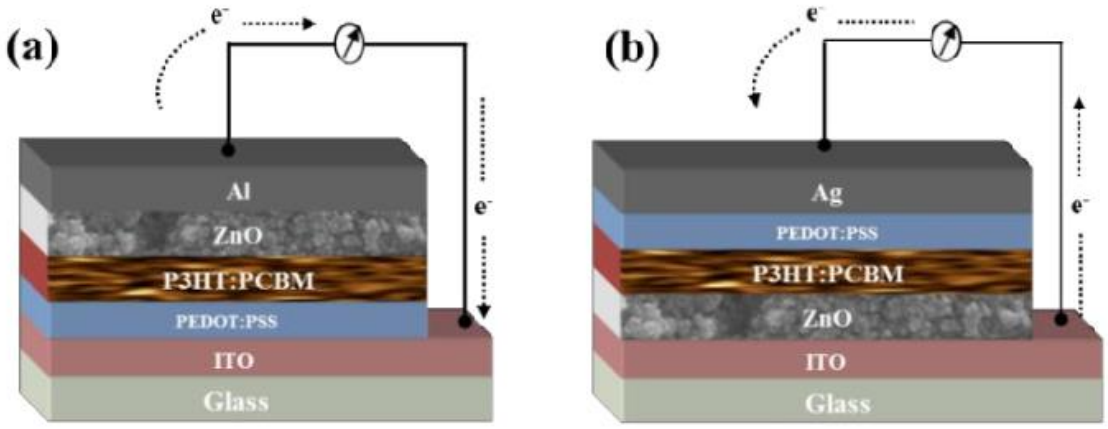

Figure 2.2. (a) conventional geometry, (b) Inverted geometry[7]

Furthermore, the use of TiO_2/ZnO as ETL has been reported by numerous researchers. H. Kim et al [8] reported improved performance of P3HT-PBCM BHJ solar cell device when TiO_2 nanoparticles were used as ETL between the photoactive layer and the top electrode. L. Qian et al [9] reported 30-80% PCE improvement in PH3T-CdSe based hybrid solar cell devices when ZnO nanoparticles were inserted as the ETL. O.M.Ntwaeaborwa et al. [10] and P.S. Mbule et al. [11] recorded 60% increase in the PCE of P3HT-PBCM based BHJ solar cell when ZnO nanoflakes were used as ETL. Although considerable increase in the PCE of BHJ solar cell devices incorporating ZnO ETL has been reported, the PCE values obtained are still lower than 20 - 40% PCE of the conventional silicon photovoltaic cells, which are relatively expensive. The presence of intrinsic defects such as zinc/oxygen interstitials, and zin/oxygen vacancies impacted negatively on optical properties of ZnO. These defects inhibit excitons dissociation at the photoactive

layer/ZnO interface, serve as recombination centre, and also the low valence energy level unfavourable for the hole blocking capabilities of the ZnO ETL [12]. Furthermore, ZnO nanoparticles have been added to a blend of P3HT:PBCM photoactive layer to improve the activy of the electron absorbing molecule. Some researchers have proposed doping ZnO with transition elements in order to balance charge transfer and improve exciton dissociation. In this study, we co-doped ZnO with magnesium (Mg) and gallium (Ga) and we evaluated the physical properties of the co-doped system. We evaluated the performance of this system when added to the P3HT:PBCM layers as electron acceptor in BHJ solar cell devices. In the next section, we discussed the fundamental properties of undoped and doped ZnO.

2.4. Zinc Oxide (ZnO)

2.4.1. Structure and Physical Properties

ZnO is a group II-VI compound semiconductor with an ionicity that resides in the border line between ionic and covalent semiconductors [13]. It exists in three polymorphs, namely, wurtzite, zinc blende, and rocksalt as shown in figure 2.3. The thermodynamically stable phase under ambient conditions is the wurtzite structure. The rock salt structure is a high pressure phase while the zinc blende phase is stabilized only by growing on cubic substrates [11]. We discuss only the wurtzite structure.

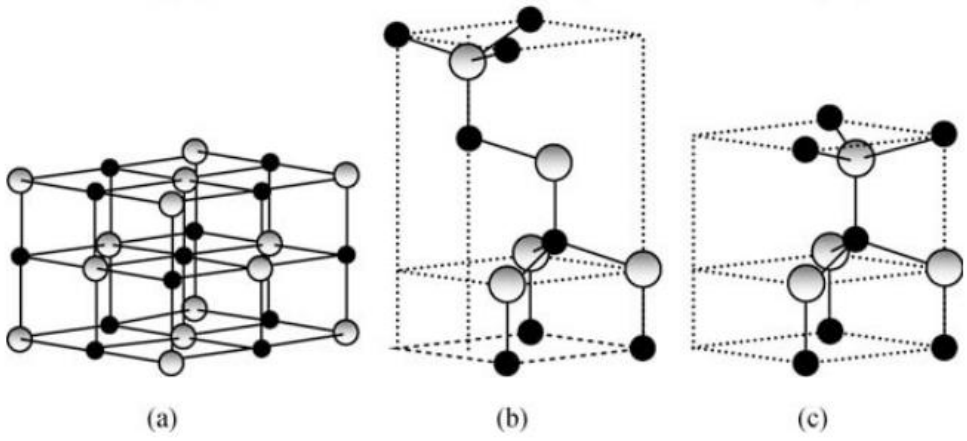

Figure 2.3. Stick-and-ball representation of ZnO crystal structures (a) Rocksalt, (b) Zinc Blende, (c) Wurtzite[14]

The schematic representation of atom and their occupancy in the conventional unit cell is depicted in figure 2.4 (a) and b). From the figure 2.3 (a), it is clear that every atom of each kind is surrounded

by four (4) of the other kind, which are located at the edges of a tetrahedron. The wurtzite structure of ZnO is made of two interpenetrating hexagonal close packed (hcp) sub-lattices with anion (O) and cation (Zn). The hexagonal unit cell corresponding to the wurtzite structure consists of two lattice parameters *a* and *c* of ratio c/a =$\sqrt{8/3} = 1.633$. It belongs to space group $P6_3mc$ in the Hermann-Mauguin notation and $C_{6\upsilon}^4$ in the Schoenflies notation[14].

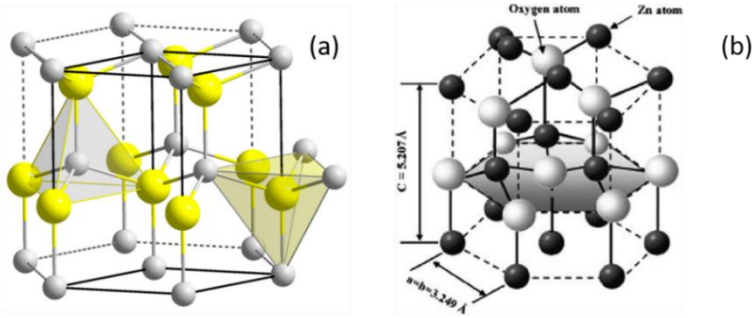

Figure 2.4. A schematic representation of wutzite ZnO. (a) Tetrahedral coordination of ZnO neighboring atoms (b) hexagonal lattice. [15]

The structure is made of two interpenetrating hexagonal closed-packed (hcp) each consisting of one type of atom that is displaced with respect to the other type of atom along the threefold c-axis by the amount u = 3/8 = 0.375 in fractional coordinates with the ABAB stacking sequence. The lattice parameters of the wurtzite structure are characterized by a = b varying between 3.2475 Å and 3.2501 Å, while the lattice constant c varies between 5.2042 Å and 5.2075 Å. Ozgür and Morkoc have reported that in the actual ZnO crystals, a deviation is seen from the atomic arrangements in the ideal wurtzite structure, and is observed by changes in the ratios c/a which yield 1.602 which is close to that of 1.633 of the ideal hcp unit cell [16]. The deviation is likely caused by factors which include stability, ionicity, internal or external strain introduced by impurities as well as intrinsic point defects such as zinc antisites and oxygen vacancies may also contribute to increased lattice constants. Lattice constants of crystalline materials are measured by x-ray diffraction (XRD) which is discussed in chapter 3. A summary of the physical properties of ZnO is presented in table 2.1.

Table 2.1. Important physical properties of ZnO

Physical Parameter	Value
Lattice parameters in nm at 300K	
a	0.32495
c	0.52069
c/a	1.6024
u	0.380
Density (g/cm^3)	5.606
Stable phase	Hexagonal, Wurtzite
Melting point (ºC)	1975
Thermal conductivity $(W/K.cm)$	0.6 – 1.2
Linear expansion coefficient (/ ºC)	a: 6.5×10^{-6} c: 3.0×10^{-6}
Static dielectric constant	8.656
Refractive index ($\boldsymbol{\lambda}$ = 0.5μm)	2.008 – 2.029
Energy band gap (eV)	3.3714, direct
Exciton binding energy (meV)	60
Electron effective mass (m_0)	0.24
Electron hall mobility (cm^2/Vs)	200
Hole effective mass (m_0)	0.59
Hole hall mobility (cm^2/Vs)	5 – 50

2.4.2. Electronic Band Structure and Optical Properties

The electronic band structure plays an important role in correlating the optical and electronic properties of a material. In ZnO, the conduction band (CB) minimum and the maximum of the valence band (VB) are found in the same wave vector ($\vec{\boldsymbol{k}}$) in the Brillouin zone. In this case the wave vector value, $\vec{\boldsymbol{k}}$(0,0,0), is zero (also referred to as the Γ point in figure 2.5) [17]. This is the

reason why ZnO is known as a direct band gap semiconductor. The band gap can be tuned by the intentional addition of impurities to the semiconductor matrix, a process known as doping [18]. Changes which occur in the band gap of ZnO due to doping can be analyzed by comparing the luminescence properties before and after doping and by studying the optical spectroscopy at low temperature.

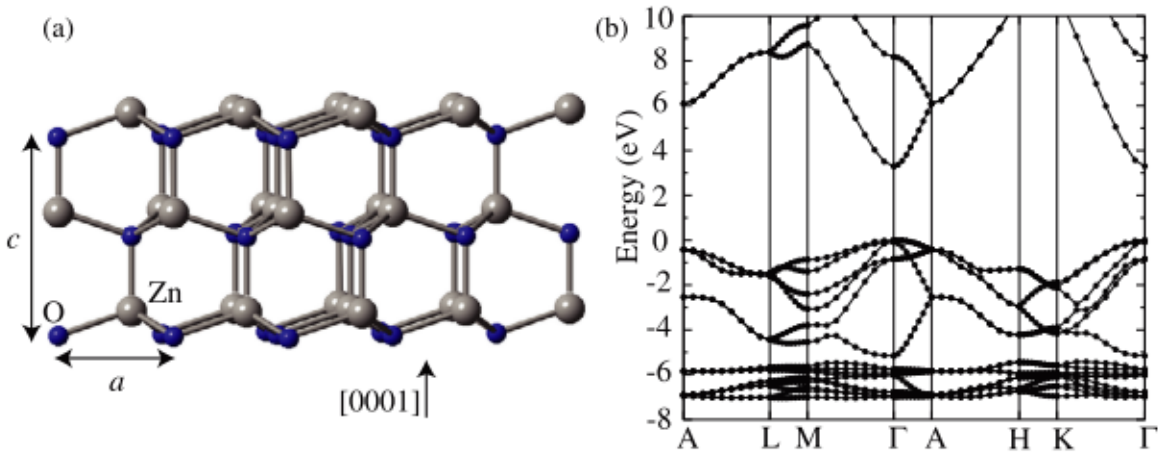

Figure 2.5. The wurtzite structure of ZnO with the lattice parameters a and c shown in (a), and the band structure of ZnO calculated using the HSE hybrid functional in (b) [19]

Luminescence is the process which involves the absorption of energy that is subsequently emitted as light. ZnO is one of the materials that exhibit this phenomenon, it emits energy in the form of light when excited with radiation [20] whose energy is higher than that of the bandgap of the material. The absorption of incident photon with energy higher than the threshold energy of ZnO leads to energy transfer to an electron in the valence band which is excited to a higher energy state (conduction band). By a series of processes this electron will start to de-excite to its ground state (valence band). If light is given off during this de-excitation process, it is called 'radiative emission' and if no light is emitted it is termed 'non-radiative relaxation' [21]. The excitation source determines the type of luminescence that occurs. As an example, when a voltage is applied as a source, the process is known as electroluminescence and when light is used, it is called photoluminescence (PL). In this study PL spectroscopy was used to examine the optical properties of ZnO. Through analysis of optical transitions, this characterization technique helps in identifying defect levels and types of impurities in the materials as well as their respective emission properties.

Photoluminescence studies have been useful in identifying emissions of ZnO. A typical photoluminescence spectrum of ZnO at room temperature exhibits two luminescence bands as shown in figure 2.6. The narrow band-edge emission located at the absorption edge in the short wavelength band in ZnO [22] is associated with excitonic recombination, While the broad band between 420 – 700 nm incorporates the broad wavelength band assigned to deep level emission that results from native point defects such as V_{Zn}, O_i, Zn_i and V_O . [23]

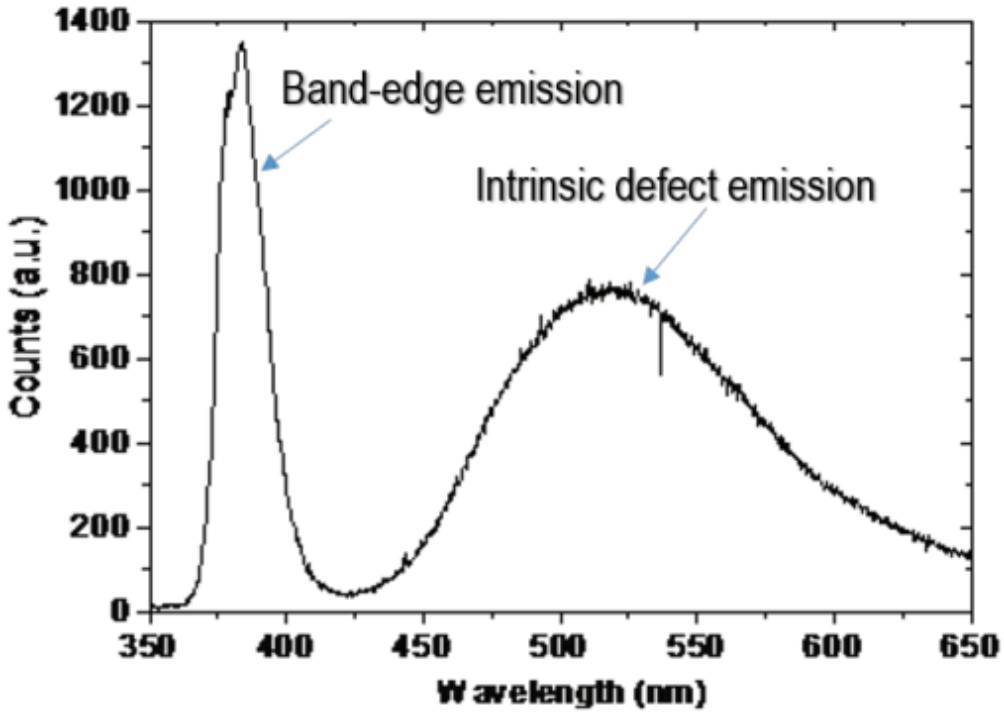

Figure 2.6. Typical photoluminescence Spectrum of ZnO[21]

2.4.3. ZnO Intrinsic Defects

Intrinsic or native defects can be regarded as imperfections in the lattice which involve only the constituent atoms [24]. These include:

- Interstitials, which are additional atoms that occupy interstices in the lattice.
- Vacancies, which signifies the absence of atoms at regular lattice sites.

- Antisites, which are A (such as Zn) atoms occupying B (such as O) lattice sites or vice versa for a binary compound.

Intrinsic defects within a crystal strongly affect their optical and electrical properties. Hence the determine the luminescence efficiency, minority carrier lifetime and identity of the doping species [25]. It is therefore of utmost importance to understand the behavior and incorporation of ZnO point defects and their formation energies which depend on chemical potentials for a possible application in semiconductor devices.

The exact energy positions and nature of defects in the ZnO band gap responsible for emission in the broad band is not fully understood. It is however generally accepted that recombination of radiative centers such as oxygen vacancies (V_O), Zinc vacancies (V_{Zn}), Oxygen interstitials (O_i), Zinc interstitials (Zn_i), Oxygen antisites (O_{Zn}) and Zinc antisites (Zn_O) represent the origin of the broad band emission of ZnO [23].

Oxygen Vacancies

Oxygen vacancies (V_O) were previously believed to be the cause of the n-type conductivity in ZnO but theoretical calculations have shown that it is actually a deep double donor with a high formation energy (3.5 eV) in an n-type ZnO. In the n-type state, the Fermi level lies near the bottom of the conduction band, while the V_O is the neutral charge state positioned at ~1 eV below the conduction band minimum (CBM). In the p-type ZnO, the formation energy can be much lower, it has a 2+ charge state qualifying it as a source of compensation in p-type ZnO [19].

Zinc Vacancies

Zinc vacancies (V_{Zn}) are double acceptors and are regarded as important compensating defects in n-type ZnO. Experimental results have shown that V_{Zn} are responsible for "red" PL in the 1.6 – 1.8 eV range. Zinc vacancies are a result of n-type samples which are synthesized in oxygen-rich environments [19]. They behave as compensating centers and occur in modest concentrations in ZnO. In p-type materials, they are found in low concentrations and have high formation energies (3.7 eV). In experiments, V_{Zn} can be identified with a weak and broad green luminescence that is centered around 2.4-2.5 eV [26].

Oxygen Interstitials

Oxygen vacancies (O_i) occur as a result of excess oxygen atoms being accommodated in the ZnO lattice. O_i may occupy octahedral sites, tetrahedral interstitial site or create split interstitials. The O_i is a deep double acceptor at the octahedral site [27]. At the tetrahedral interstitial site, due to being unstable, relaxes into a split-interstitial arrangement sharing a lattice site with a substitutional oxygen atom as a nearest neighbor.

Zinc Interstitials

Zinc interstitials (Zn_i) are shallow double donor as suggested by numerous first principle calculations [27]. They can be found in two occupancies in the hexagonal wurtzite structure of ZnO, namely at:

- The octahedral interstitial site which is the channel that runs along the c axis equidistant from 3 oxygen and 3 zinc atoms.
- The tetrahedral interstitial site where one oxygen and zinc are nearest neighbor atoms, though this occupancy is usually unstable due to geometric constraints [28].

Zinc Antisites

The intrinsic defect in ZnO known as the zinc antisite (Zn_O) is formed whenever an oxygen atom is substituted by a zinc atom in its lattice site. The formation energies of this defect are higher than those of the Zn_i and demonstrate high thermal stability. Janotti et al have suggested that the diffusion mechanism can be separated into V_O and Zn_i components [12]. These defects are associated with zinc rich conditions with the condition for the endothermic reaction described by the following equation at formation energy of ~2.8 eV. This leads to difficulty in annihilating Zn_O compared to Zn_i.

$$Zn_O^{2+} \rightarrow Zn_i^{2+} + V_O^0 \quad \ldots\ldots\ldots\ldots\ldots\ldots \quad (2.1)$$

Oxygen Antisite

The oxygen antisite (O_{Zn}) defect occurs when an oxygen atom occupies a site in the zinc sub-lattice. The formation energy of O_{Zn} is the highest in all native point defects, even under oxygen rich conditions. O_{Zn} antisites are unstable deep acceptors that can potentially arise under non-equilibrium conditions such as ion implantation or under irradiation. Figure 2.7 depicts the energy level positions of intrinsic point defects in ZnO relative to the valence band maximum (VBM) and conduction band minimum (CBM). The positive and negative integers represent the charged defect state. Oxygen interstitials of the octahedral and split configuration are shown, with the split configuration offering the most stable sites.

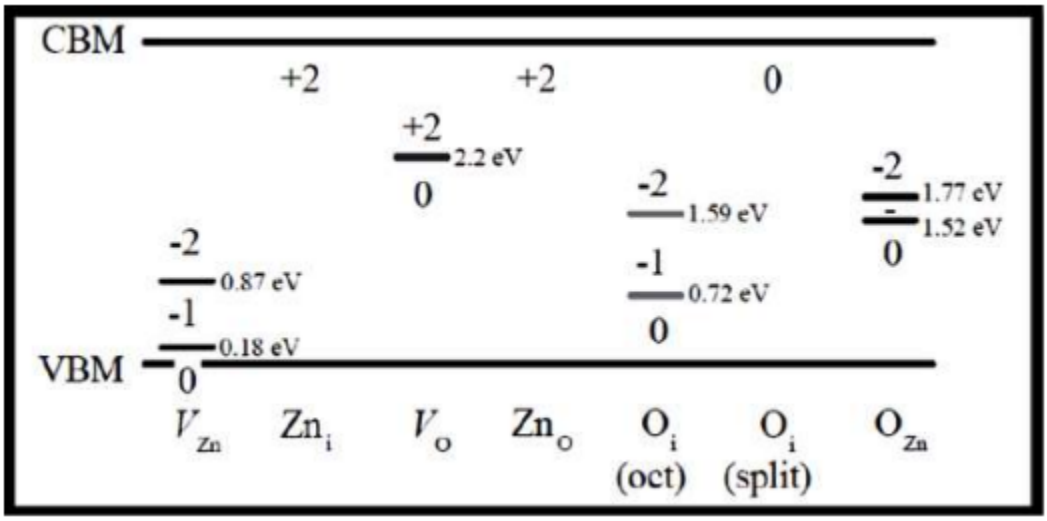

Figure 2.7. Schematic diagram of intrinsic point defects in ZnO [23]

2.5. Phonon modes in Wurtzite ZnO

The vibrational properties of ZnO enable understanding of the thermal and electronic properties which may impede some of its applications [29]. The lattice vibrations of materials are described by the corresponding phonon dispersion relations and can be used to determine the thermal properties of ZnO [30]. As photons interact with electrons in the lattice, Raman scattering measurements can be used to determine the vibrational structure and electronic properties of the ZnO. Raman spectroscopy is discussed in more detail in chapter 3.

At ambient temperature and pressure, ZnO crystallizes in the hexagonal wurtzite phase [14]. The 4 atoms that make up the hexagonal unit cell result in 12 phonon branches, 3 acoustic and 9 optical phonons [29]. These are classified by the irreducible representation from group theory: $\Gamma = 2A_1 + 2B_1 + 2E_1 + 2E_2$. One E_1 pair (E_1 (TO) and E_1 (LO)) and one A_1 mode are acoustic phonons. The 9 optical phonons arise from one doubly degenerate E_1 branch (Raman and IR active), one A_1 branch (Raman and IR active), two doubly degenerate E_2 branches (Raman active), and two inactive B_1 branches. There are therefore four Raman active phonon modes at the center of the Brillouin zone [31].

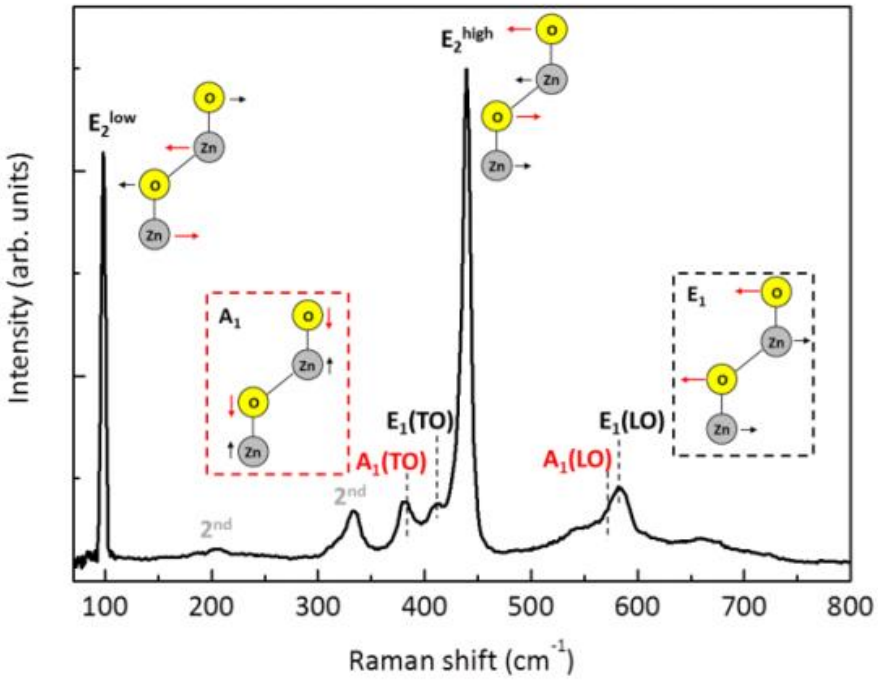

Figure 2.8. ***Un-polarized Raman spectrum of bulk ZnO, λ_{exc} = 532nm. Raman active modes with the corresponding vibrations of the ions are indicated. The red arrows specify the dominant ions displacements*** [32]

The Raman spectrum of ZnO displays six first-order peaks instead of the four active modes as depicted in figure 2.8. Here, Russo et al. gives an un-polarized spectrum of bulk ZnO along with atomic displacement sketches of the modes [30]. The two most prominent peaks at 99 cm^{-1} and 437 cm^{-1} are the E_2 low and E_2 high modes respectively. The E_2 low mode is dominated by vibrations of heavy Zn sub-lattice while the E_2 is mostly vibrations from oxygen atoms. As atoms

in each sub-lattice move perpendicular to the c-axis, the neighboring ions move in opposite directions giving a net displacement of ions as zero and no net polarization. For this reason, these two modes are known as non-polar modes. A_1 and E_1 phonons, on the contrary, are polar modes that are oxygen dominated. These atoms move perpendicular or parallel to the c-axis in the E_1 and A_1 symmetry respectively. This happens in such a way that the net displacement induces an oscillating polarization of the Zn sub-lattice with respect to the oxygen sub-lattice. This results in a splitting of these modes into longitudinal optical and transverse optical components [33]. Therefore, the associated Raman peaks become four, i.e. A_1(TO) at 380 cm^{-1}, E_1(TO) at 407 cm^{-1}, A_1(LO) at 574 cm^{-1}, E_1(LO) at 583 cm^{-1}, which account for the 6 detectable peaks together with the two E_2 modes. These are shown in table 2.2 below.

Table 2.2. Raman modes of ZnO and corresponding shift values [32]

Symmetry	Frequency (cm^{-1})
A_1 -TO	378 – 380
E_1 -TO	409 - 413
A_1 -LO	574 - 579
E_1 -LO	583 – 591
E_2^{low}	99 – 101
E_2^{high}	437 - 438

2.6. Doping of ZnO

Transparent conductive oxide materials such as ZnO have spurred widespread interest in the research community due to a variety of promising applications such as flat panel displays, touch screens and solar cells. ZnO also has applications as piezoelectric generators that convert mechanical energy into electrical energy to power devices, incorporating Fe dopant has seen them used as multiferroic materials in semiconductor spintronics and in gas sensors [34]. Pristine ZnO is however, unfavorable in the previously mentioned applications because of its inferior electrical properties such as low electron mobility [34]. To conquer this shortfall, it is frequently doped with group II and III elements such as Magnesium, Cadmium, Aluminum and Gallium. We discuss only on magnesium (Mg) and gallium (Ga) as dopants in ZnO.

2.6.1. Magnesium doping in ZnO

The addition of Mg in the ZnO lattice has been found to expand the optical band gap [35] of ZnO thereby making the compound a transparent material active in the UV region [36]. Therefore, the ability to tune the band gap makes ZnO a very appealing material for numerous applications [36]. The incorporation of Mg in ZnO is preferred for various reasons, which include; (i) the larger ionic radius of Zn^{2+} (0.74 Å) is comparable to that of Mg^{2+} (0.66 Å) [37].

(ii) Adding Mg into Zn lattice does not significantly change lattice constants.

(iii) The MgO solubility in ZnO is high [38].

(iv) Mg-doped ZnO has been reported to act as efficient photocatalysts in the degradation of organic pollutants in the environment.

In addition, Alexander et al. also stated that addition of ZnMgO in organic solar cell devices as an electron transport layer can improve the efficiency of the devices [39]. The continued addition of Mg dopant to ZnO does however have negative impacts on the conductivity of the semiconductor.

2.6.2. Gallium doping in ZnO

Replacing Zn^{2+} ions in ZnO by trivalent ions such as Ga^{3+} can greatly improve the electrical properties by increasing the carrier concentration and thus in turn reducing the electrical resistivity of ZnO. Furthermore, Ga^{3+} doping has been found to improve stability of ZnO for use in applications such as solar cells [40]. Ga in n-type ZnO has been found to be an effective dopant for the following reasons; (i) the ionic radius of Zn (0.74 Å) and that of Ga (0.76 Å) are almost similar. (ii) The substitution of Zn^{2+} with Ga^{3+} provides an extra electron into the lattice [41]. (iii) The bond length of Zn-O (1.97Å) is comparable to that of Ga-O (1.92 Å), therefore, the addition of Ga^{3+} can substitute Zn^{2+} over a broad doping range as compared to other elements without causing significant distortion to the ZnO lattice [42]. Gallium is also selected as a dopant in ZnO because it offers better oxidation resistance which can be beneficial in improving OSC device stability.

2.7. Photovoltaic parameters measurement

To characterize the performance of organic photovoltaic cells, the current density as a function of voltage is measured under illumination of AM1.5G (100 mW/cm^2) solar spectrum, where AM1.5G refers to the mass of air light from the sun has to travel through, which is 1.5 times larger than the light incident on the surface that faces the sun with zenith angle of 48.2° and a temperature of 25°C [43]. This spectrum is shown in figure 2.9 below. The photovoltaic parameters that can be directly measured are power maximum **(P_{max}),** the open circuit voltage (V_{oc}), the short-circuit current density (J_{sc}), and the fill factor (FF), while the power conversion efficiency (η) is determined from these parameters.

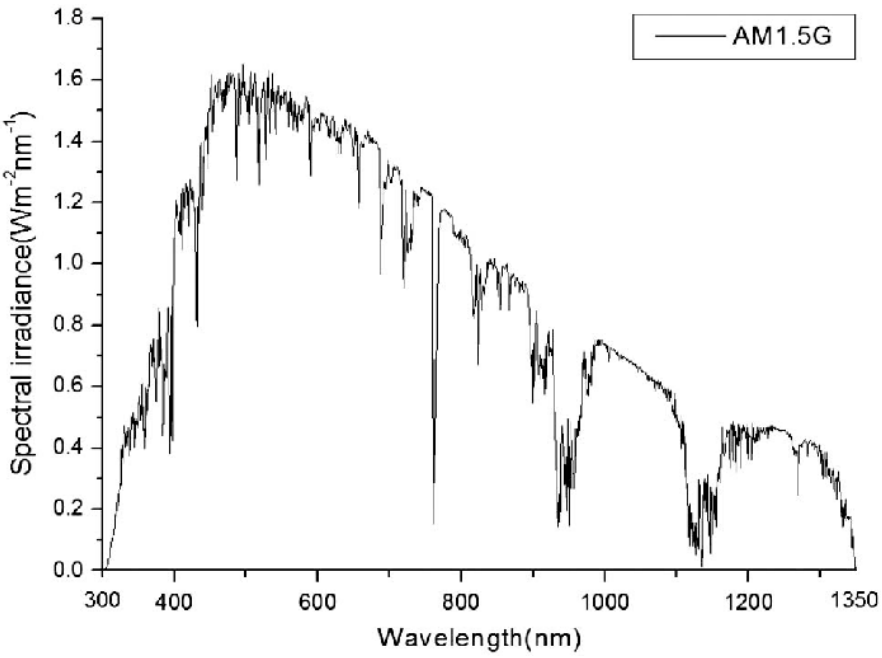

Figure 2. 9. AM1.5G solar spectrum.

- **Open circuit voltage (V_{oc})**

  The voltage that is obtained when no current flows through the circuit is known as the open circuit voltage [44]. It depends on the photo-generated current density (J_{ph}) and can be determined using the equation:

$$V_{OC} = \frac{K_B T}{q} \ln\left(\frac{J_{ph}}{J_0} + 1\right) \approx \frac{K_B T}{q} \ln\left(\frac{J_{ph}}{J_0}\right), \qquad (2.2)$$

  Where q is the elementary charge, k_B is the Boltzmann constant, T is the temperature in Kelvin, J_0 is the saturation current density and Jph is the photon current density.

- **Short circuit current density (J_{sc})**

  The current that flows through the solar cell when no voltage is applied (V = 0) is known as the short-circuit current density. This current arises from light generated charge carriers [45]. It is dependent on the photon flux incident on the solar cell that is determined by the spectrum of the incident light.

- **Maximum power point (P_{max})**

  The point on the J-V curve that maximizes the product $J_{max} \times V_{max}$ is known as the maximum power point **(P_{max})**. At this point, the maximum electrical power is delivered to the load at the level of irradiation. This point is depicted in blue shaded area in figure 2.10 below [45].

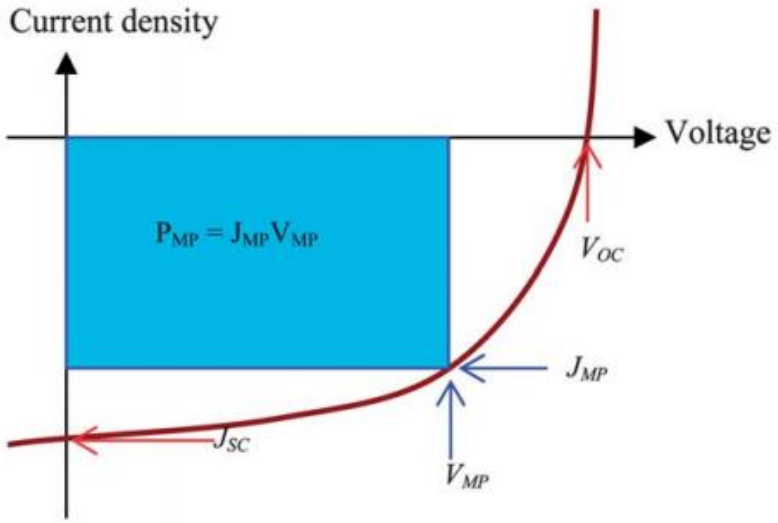

Figure 2. 10. Current density–voltage (J–V) characteristic of a solar cell under illumination[46]

- **Fill Factor**

  The ratio between the maximum power generated by the device ($J_{max} \times V_{max}$) and the product of J_{sc} and V_{oc} is known as the fill factor (FF). The FF is calculated using the equation:

$$FF = \frac{J_{max} * V_{max}}{J_{sc} * V_{oc}} = \frac{P_{max}}{J_{sc} * V_{oc}} \qquad (2.3)$$

- **Power conversion efficiency (PCE, η)**

  The ratio of the maximum output power (P_{max}) to the input power (P_{in}) gives the power conversion efficiency η of a solar cell, i.e.

$$\eta = \frac{J_{max} * V_{max}}{P_{in}} = \frac{P_{max}}{P_{in}} \quad \textbf{(2.4)}$$

PCE relates to V_{oc} and J_{sc} when the FF is used,

$$\eta = \frac{J_{sc} * V_{oc} * FF}{P_{in}} \quad \textbf{(2.5)}$$

Parasitic Resistances

- **Series Resistance (R_s)**

  Resistances that arise from the front surface contacts and the cell material's resistance to current flow are known as series resistances. These particularly cause problems at high values of J_{sc}, such as under concentrated light [45]. This value is found by calculating the inverse of the slope at V_{OC} parallel to the y-axis in J-V curves, this is illustrated in figure 2.11.

- **Shunt Resistance (R_{sh})**

  Parallel or shunt resistance arises as a result of alternative pathways for current through the solar cell device. These paths could be around the edges of the device, through cracks that may form through the active layer and between the contacts of different polarities [45]. This value is obtained by calculating the inverse of the slope at J_{SC} parallel to the x-axis as shown in figure 2.11

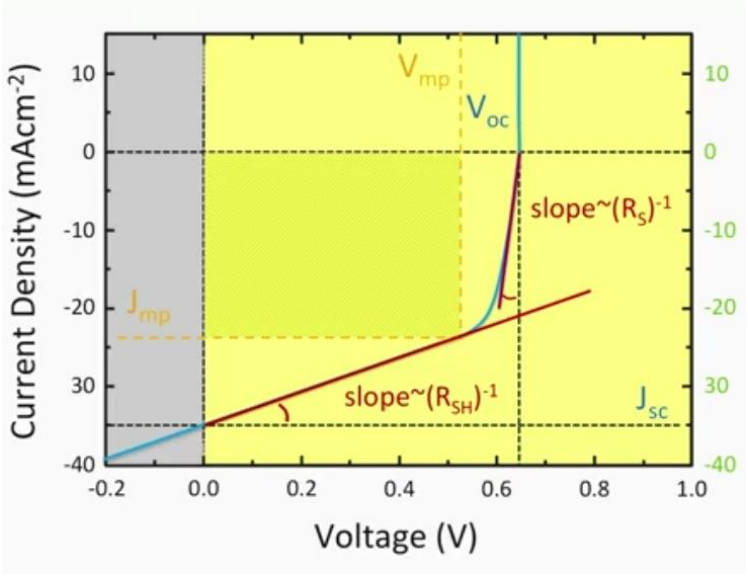

Figure 2. 11. The current density and Vs. voltage curve that depict how the series (R_s) and shunt (R_{Sh}) resistances are obtained from slopes at Voc and J_{SC}.[47]

References

[1] "Organic Photovoltaics — Optoelectronics." https://www.oe.phy.cam.ac.uk/research/photovoltaics/ophotovoltaics (accessed Oct. 26, 2020).

[2] I. Arbouch, Y. Karzazi, and B. Hammouti, "Organic photovoltaic cells: Operating principles, recent developments and current challenges – review," *Phys. Chem. News*, vol. 72, no. 4, pp. 73–84, 2014.

[3] S. Rafique, S. M. Abdullah, K. Sulaiman, and M. Iwamoto, "Fundamentals of bulk heterojunction organic solar cells: An overview of stability/degradation issues and strategies for improvement," *Renewable and Sustainable Energy Reviews*, vol. 84. Elsevier Ltd, pp. 43–53, Mar. 01, 2018, doi: 10.1016/j.rser.2017.12.008.

[4] Y. W. Su, S. C. Lan, and K. H. Wei, "Organic photovoltaics," *Mater. Today*, vol. 15, no. 12, pp. 554–562, 2012, doi: 10.1016/S1369-7021(13)70013-0.

[5] T. Ameri, P. Khoram, J. Min, C. J. Brabec, and M. O. E. L. U. Mo, "Organic Ternary Solar Cells : A Review," pp. 4245–4266, 2013, doi: 10.1002/adma.201300623.

[6] J. Cirák, "Concept of Organic Photovoltaics: Operational Principles and Materials," *Acta Electrotech. Inform.*, vol. 13, no. 1, 2013, doi: 10.2478/aeei-2013-0006.

[7] A. Sciences, "The effects of the ZnO nanoparticles buffer layer on organic solar cells By," no. July, 2013.

[8] H. Kim, W.-W. So, and S.-J. Moon, "The importance of post-annealing process in the device performance of poly(3-hexylthiophene): Methanofullerene polymer solar cell," *Sol. Energy Mater. Sol. Cells*, vol. 91, pp. 581–587, 2007, doi: 10.1016/j.solmat.2006.11.010.

[9] L. Qian *et al.*, “c0jm03799k 3814..3817,” *J. Mater. Chem*, vol. 21, 2011, doi: 10.1039/c0jm03799k.

[10] O. M. Ntwaeaborwa *et al.*, “Post-fabrication annealing effects on the performance of P3HT:PCBM solar cells with/without ZnO nanoparticles,” 2011, doi: 10.1016/j.physb.2011.09.103.

[11] P. S. Mbule, T. H. Kim, B. S. Kim, H. C. Swart, and O. M. Ntwaeaborwa, “Effects of particle morphology of ZnO buffer layer on the performance of organic solar cell devices,” 2013, doi: 10.1016/j.solmat.2013.01.010.

[12] M. D. McCluskey, *Defects in ZnO*, no. 0. Elsevier Ltd, 2018.

[13] J. Shadia, “1 . Introduction to II-VI Compounds,” vol. 661, no. 2, 2014.

[14] Ü. Özgür *et al.*, “A comprehensive review of ZnO materials and devices,” *J. Appl. Phys.*, vol. 98, no. 4, pp. 1–103, 2005, doi: 10.1063/1.1992666.

[15] H. Morkoç and Ü. Özgür, “ZnO Nanostructures,” in *Zinc Oxide*, Wiley, 2009, pp. 365–386.

[16] Ü. Ozgur, D. Hofstetter, and H. Morkoç, “ZnO devices and applications: A review of current status and future prospects,” *Proc. IEEE*, vol. 98, no. 7, pp. 1255–1268, 2010, doi: 10.1109/JPROC.2010.2044550.

[17] P. Xu, Y. Sun, C. Shi, F. Xu, and H. Pan, “Electronic structure of ZnO and its defects,” *Sci. China, Ser. A Math. Physics, Astron.*, vol. 44, no. 9, pp. 1174–1181, 2001, doi: 10.1007/bf02877436.

[18] Z. Zhi-yong, “Electronic structure and optical properties of,” vol. 16, no. 9, pp. 2791–

2797, 2007.

[19] A. Janotti and C. G. Van De Walle, “Fundamentals of zinc oxide as a semiconductor,” *Reports Prog. Phys.*, vol. 72, no. 12, 2009, doi: 10.1088/0034-4885/72/12/126501.

[20] R. Raji and K. G. Gopchandran, “ZnO nanostructures with tunable visible luminescence: Effects of kinetics of chemical reduction and annealing,” *J. Sci. Adv. Mater. Devices*, vol. 2, no. 1, pp. 51–58, Mar. 2017, doi: 10.1016/j.jsamd.2017.02.002.

[21] N. C. Gatsi, “Spectroscopy of trivalent neodymium ions (Nd3+) in zinc oxide (ZnO) thin films and powders,” no. May, 2019.

[22] P. A. Rodnyi and I. V. Khodyuk, “Optical and luminescence properties of zinc oxide (Review),” *Opt. Spectrosc. (English Transl. Opt. i Spektrosk.*, vol. 111, no. 5, pp. 776–785, 2011, doi: 10.1134/S0030400X11120216.

[23] “spectral conversion and application to solar cells . By Francis Otieno Otieno In the School of Physics Faculty of Science University of the Witwatersrand Johannesburg – South Africa Supervisor : Prof . Daniel Wamwangi.”

[24] F. Oba, M. Choi, A. Togo, and I. Tanaka, “Point defects in ZnO: An approach from first principles,” *Sci. Technol. Adv. Mater.*, vol. 12, no. 3, 2011, doi: 10.1088/1468-6996/12/3/034302.

[25] M. D. McCluskey and S. J. Jokela, “Defects in ZnO,” *J. Appl. Phys.*, vol. 106, no. 7, pp. 1–13, 2009, doi: 10.1063/1.3216464.

[26] T. M. Børseth, B. G. Svensson, A. Y. Kuznetsov, P. Klason, Q. X. Zhao, and M. Willander, “Identification of oxygen and zinc vacancy optical signals in ZnO,” *Appl.*

Phys. Lett., vol. 89, no. 26, pp. 18–21, 2006, doi: 10.1063/1.2424641.

[27] K. E. Knutsen *et al.*, “Zinc vacancy and oxygen interstitial in ZnO revealed by sequential annealing and electron irradiation,” *Phys. Rev. B - Condens. Matter Mater. Phys.*, vol. 86, no. 12, pp. 1–5, 2012, doi: 10.1103/PhysRevB.86.121203.

[28] A. Janotti and C. G. Van De Walle, “New insights into the role of native point defects in ZnO,” *J. Cryst. Growth*, vol. 287, no. 1, pp. 58–65, 2006, doi: 10.1016/j.jcrysgro.2005.10.043.

[29] M. Silambarasan, S. Saravanan, and T. Soga, “Raman and photoluminescence studies of Ag and Fe-doped ZnO nanoparticles,” *Int. J. ChemTech Res.*, vol. 7, no. 3, pp. 1644–1650, 2015.

[30] V. Russo, M. Ghidelli, P. Gondoni, C. S. Casari, and A. L. Bassi, “Multi-wavelength Raman scattering of nanostructured Al-doped zinc oxide.”

[31] C. Bundesmann *et al.*, “Raman scattering in ZnO thin films doped with Fe, Sb, Al, Ga, and Li,” *Appl. Phys. Lett.*, vol. 83, no. 10, pp. 1974–1976, 2003, doi: 10.1063/1.1609251.

[32] “No Titleسکولاریسم و تلویزیون رسانه مقالات خلاصه,” pp. 1–27, 1387, [Online]. Available: http://www.ghbook.ir/index.php?name=سراسری اندیشی هم دومین مقالات مجموعه و تلویزیون رسانه سکولاریسم &option=com_dbook&task=readonline&book_id=13629&page=108&chkhashk=03C706812F&Itemid=218&lang=fa&tmpl=component.

[33] Y. Song, S. Zhang, C. Zhang, Y. Yang, and K. Lv, “Raman spectra and microstructure of zinc oxide irradiated with swift heavy ion,” *Crystals*, vol. 9, no. 8, 2019, doi:

10.3390/cryst9080395.

[34] H. Q. Le and S. J. Chua, “Gallium and indium co-doping of epitaxial zinc oxide thin films grown in water at 90 °c,” *J. Phys. D. Appl. Phys.*, vol. 44, no. 12, Mar. 2011, doi: 10.1088/0022-3727/44/12/125104.

[35] M. Caglar, Y. Caglar, and S. Ilican, “Investigation of the effect of Mg doping for improvements of optical and electrical properties,” *Phys. B Condens. Matter*, vol. 485, pp. 6–13, Mar. 2016, doi: 10.1016/j.physb.2015.12.049.

[36] S. B. Woodley, A. A. Sokol, C. R. A. Catlow, A. A. Al-sunaidi, and S. M. Woodley, “Structural and Optical Properties of Mg and Cd Doped ZnO Nanoclusters,” 2013.

[37] G. Kasi and J. Seo, “Influence of Mg doping on the structural, morphological, optical, thermal, and visible-light responsive antibacterial properties of ZnO nanoparticles synthesized via co-precipitation,” *Mater. Sci. Eng. C*, vol. 98, no. January, pp. 717–725, 2019, doi: 10.1016/j.msec.2019.01.035.

[38] F. Tian *et al.*, “Miscibility and ordered structures of MgO-ZnO alloys under high pressure,” *Sci. Rep.*, vol. 4, pp. 1–6, 2014, doi: 10.1038/srep05759.

[39] A. Alexandrov, M. Zvaigzne, D. Lypenko, I. Nabiev, and P. Samokhvalov, “Al-, Ga-, Mg-, or Li-doped zinc oxide nanoparticles as electron transport layers for quantum dot light-emitting diodes,” *Sci. Rep.*, vol. 10, no. 1, pp. 1–11, 2020, doi: 10.1038/s41598-020-64263-2.

[40] S. Das and T. L. Alford, “Optimization of the zinc oxide electron transport layer in P3HT:PC61BM based organic solar cells by annealing and yttrium doping,” *RSC Adv.*,

vol. 5, no. 57, pp. 45586–45591, 2015, doi: 10.1039/c5ra05258k.

[41] R. E. Marotti, D. N. Guerra, C. Bello, G. Machado, and E. A. Dalchiele, “Bandgap energy tuning of electrochemically grown ZnO thin films by thickness and electrodeposition potential,” *Sol. Energy Mater. Sol. Cells*, vol. 82, no. 1–2, pp. 85–103, 2004, doi: 10.1016/j.solmat.2004.01.008.

[42] C. Khaywimut, C. Bhoomanee, S. Choopun, and P. Ruankham, “Effects of GA doping concentration on morphological and optical properties of hydrothermally grown ZnO nanorods,” *Mater. Today Proc.*, vol. 17, pp. 1231–1239, 2019, doi: 10.1016/j.matpr.2019.06.011.

[43] J. M. Kroon, M. M. Wienk, W. J. H. Verhees, and J. C. Hummelen, “Accurate efficiency determination and stability studies of conjugated polymer/fullerene solar cells,” *Thin Solid Films*, vol. 403–404, pp. 223–228, 2002, doi: 10.1016/S0040-6090(01)01589-9.

[44] C. J. Brabec, N. S. Sariciftci, and J. C. Hummelen, “Plastic Solar Cells,” *Adv. Funct. Mater.*, vol. 11, no. 1, pp. 15–26, Feb. 2001, doi: 10.1002/1616-3028(200102)11:1<15::AID-ADFM15>3.0.CO;2-A.

[45] J. Nelson, *The Physics of Solar Cells*. PUBLISHED BY IMPERIAL COLLEGE PRESS AND DISTRIBUTED BY WORLD SCIENTIFIC PUBLISHING CO., 2003.

[46] J. L. Huang, “Energy & Applications of ZnO in organic and hybrid solar cells,” no. January 2021, 2011, doi: 10.1039/C1EE01873F.

[47] A. Smets, K. Jäger, O. Isabella, R. Swaaij, and M. Zeman, “Solar Energy: The Physics and Engineering of Photovoltaic Conversion, Technologies and Systems,” *undefined*,

2016.

Chapter 3 – Material Preparation and Experimental Techniques

3.1. Introduction

Powder samples of undoped,1 mol % Mg doped, 3 mol % Mg doped, 1mol % Ga doped, 3 mol% Ga doped, 1 mol % Mg and 3 mol% Ga mol co-doped ZnO were used in this study. The samples were annealed at 500 and 900°C. A sol-gel method was used to synthesize the samples as illustrated in section 3.2. The crystal structure, chemical composition and particle morphology were determined using X-ray diffraction, Raman spectroscopy, Energy dispersive spectroscopy, Scanning electron microscopy and Transmission electron microscopy, respectively. The optical and magnetic properties were determined using UV-visible spectrophotometry, Photoluminescence spectroscopy and Physical Property Measurement System. The basic principles of these characterization techniques are discussed in section 3.3.

3.2. Synthesis of Undoped and doped ZnO

From the ratio of grams to atomic mass units of Zinc, Magnesium, Gallium and Oxygen, the number of moles was obtained. From the product of these number of moles and atomic mass units of the precursors zinc acetate, magnesium acetate and gallium (III) Nitrite hydrate set amounts in grams of precursor could be measured on a balance. For example, for 3mol% doping of ZnO, 2.3 grams of zinc acetate and 0.054 grams of magnesium acetate were measured and dissolved in 10 milliliters of distilled water. 4 grams of sodium hydroxide pellets were then dissolved in 15 milliliters of distilled water in a separate beaker and the two mixtures added together while stirring over a magnetic stirrer at room temperature until a clear mixture was obtained. Ethanol of 99.8% purity was added drop wise using a burette to the clear mixture leading to the formation of a white gel-like precipitate. This precipitate is then decanted into centrifuge tubes and centrifuged at 800 rpm for 5 minutes to separate the solute from the ethanoic solution. The solute was then washed 5 times with distilled water and then dried in an oven at 100°C overnight. The dry white solute is then crushed into fine powder and taken for annealing at 500°C (for annealed samples) and then characterization. The schematic of the sample preparation procedure is depicted in figure 3.1.

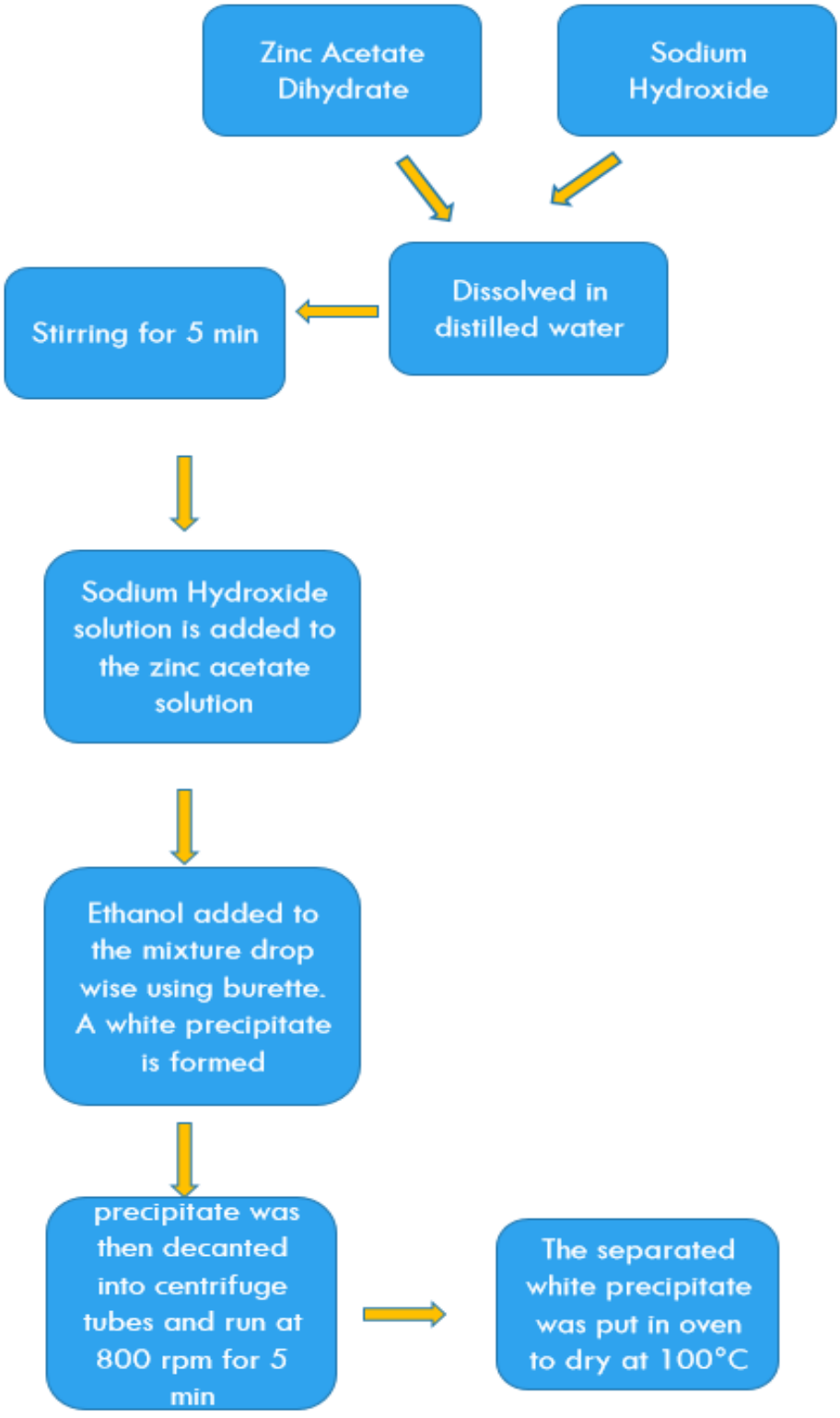

Figure 3.1 Schematic diagram of Sol-gel Synthesis of powder samples

3.3. Characterization Techniques

3.3.1. X-ray Diffraction

Powder X-ray diffraction (XRD) is a rapid, non-destructive analytical technique used to determine the phase identity, preferred crystal orientations as well as other structural parameters such as crystallinity, average grain size and micro-strain in ordered and disordered solids [2]. Crystalline materials have regularly packed atoms which can be characterized by an inter-planar spacing, d, as shown in figure 3.2 below.

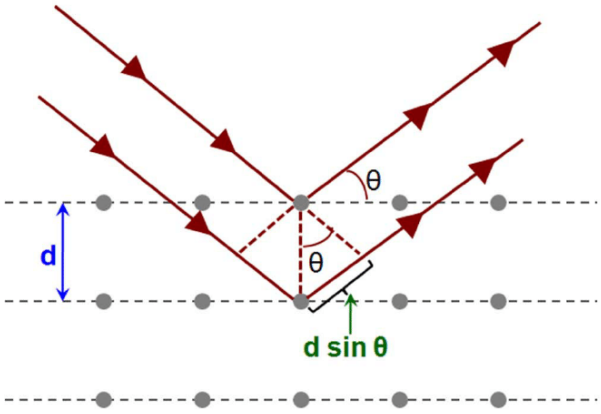

Figure 3.2. Diffraction of x-rays by a crystal [3]

X-rays are used to probe crystalline materials because their wavelength is of the same order as the d spacing between atoms [4]. The electrons in these atoms act therefore as scattering centers for incident x-rays. Though most of the scattered rays interfere destructively, there are particular angles of incidence that result in constructive interference which leads to diffraction patterns. This diffraction only occurs if Bragg's relation is satisfied:

$$2dsin\theta = n\lambda \qquad (3.1)$$

where n is an integer that defines the order of reflection, d is the plane spacing given by Miller indices *h*, *k* and *l*, λ, wavelength of incident x-rays and θ, the Bragg angle. With regard to the ZnO hexagonal structure, d is related to lattice parameters a, c and Miller indices by the following relation [5]:

$$\frac{1}{d^2_{(hkl)}} = \frac{4}{3}\left(\frac{h^2+hk+k^2}{a^2}\right) + \frac{l^2}{c^2} \qquad \textbf{(3.2)}$$

Using the first-order approximation [5], $\boldsymbol{n}$ = 1

$$\boldsymbol{sin^2\theta = \frac{\lambda^2}{4a^2}\left[\frac{4}{3}(h^2 + hk + k^2) + (\frac{a}{c})^2 l^2\right]} \qquad \textbf{(3.3)}$$

The lattice constant ***a,*** is calculated for the (100) plane by [5],

$$\boldsymbol{a = \frac{\lambda}{\sqrt{3}\sin\theta_{(100)}}} \qquad \textbf{(3.4)}$$

And for the (002) plane the lattice constant ***c*** is calculated as follows [5],

$$\boldsymbol{c = \frac{\lambda}{\sin\theta_{(002)}}} \qquad \textbf{(3.5)}$$

In order to obtain the crystallite size and the lattice strain, the Williamson-Hall method is used. Williamson and Hall postulated that the broadening of the diffraction peak is due to the strain and crystallite size contributions [6]. This method differentiates between the strain-induced and size-induced peak broadening by taking peak width as a function of $2\boldsymbol{\theta}$. Broadening in powders due to strain caused by distortions and crystal imperfection was calculated using,

$$\boldsymbol{\varepsilon = \frac{\beta}{4tan\theta}} \qquad \textbf{(3.6)}$$

From the XRD peak width of (101) the average crystallite size values can be determined using the Debye-Scherrer equation,

$$\boldsymbol{D = \frac{\kappa\lambda}{\beta cos\theta}} \qquad \textbf{(3.7)}$$

The overall peak broadening is given by the sum of the contributions of strain and that of crystallite size in the material and can be represented as,

$$\boldsymbol{\beta_{hkl} = \beta_D + \beta_\varepsilon} \qquad \textbf{(3.8)}$$

where $\boldsymbol{\beta}_D$ represents the contribution of crystallite size, $\boldsymbol{\beta}\varepsilon$ is strain-induced broadening and $\boldsymbol{\beta}_{hkl}$ is the instrument corrected broadening of the width at half maximum intensity. When assuming the strain and particle size contributions to line broadening as being independent of each other, we have the observed line breadth as a sum of equations (6) and (7),

$$\boldsymbol{\beta_{hkl} = \frac{\kappa\lambda}{D\cos\theta} + 4\varepsilon\tan\theta} \qquad \textbf{(3.9)}$$

Rearranging (9) we get,

$$\boldsymbol{\beta_{hkl}\cos\theta_{hkl} = \frac{\kappa\lambda}{D} + 4\varepsilon\sin\theta_{hkl}} \qquad \textbf{(3.10)}$$

Equation (10) is the **Williamson-Hall** equation, representing the uniform deformation model (UDM). In this model the crystal is considered as being isotropic in nature and the direction in which measurements are taken does not affect the properties.

The basic components of an X-ray diffractometer comprise of an X-ray source, a sample holder and an X-ray detector are depicted. A cathode ray tube produces X-rays by heating a tungsten filament which produces electrons [7]. The electrons are then accelerated towards the target by applying a voltage thus bombarding the target material with electrons. When the electrons carry enough energy to knock out inner shell electrons in the target, the characteristic X-ray spectrum is produced. All the components of the diffractometer lie within the circumference of a circle, commonly referred to as the focusing circle as depicted in figure 3.3 below.

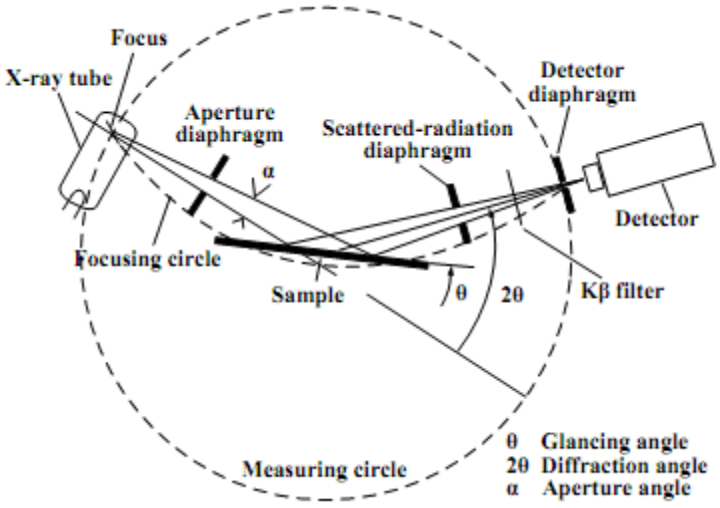

Figure 3.3. The geometry of an x-ray diffractometer [8]

In the Bragg – Brentano (**θ**-2**θ**) geometry, the X–ray source is fixed while the detector and sample sweep through angles in such a way that the **θ**-2**θ** condition is maintained [9]. The most commonly used source of X-rays is copper. However, cobalt, chromium and molybdenum are other sources which can be used.

In this study, a Bruker D2 Phaser Benchtop diffractometer shown in figure 3.4 was used for characterization of the powder samples which uses a CuKα source with the wavelength of 1.541 Å This instrument uses X-ray powder diffraction in the Bragg-Brentano configuration to collect high quality data [10].

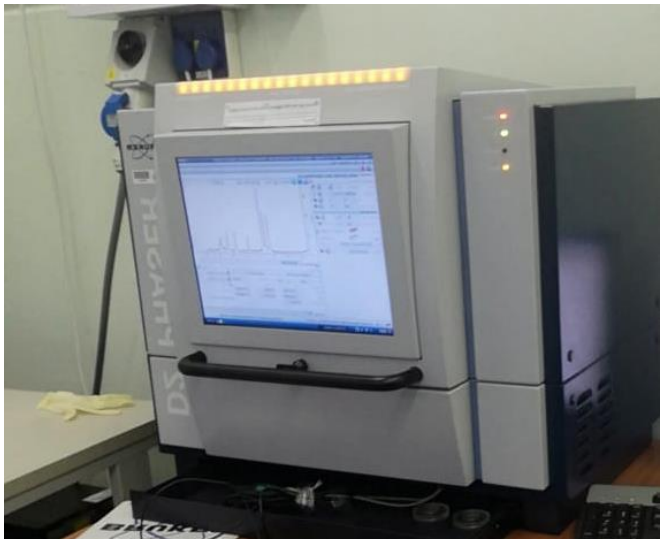

Figure 3.4. The Bruker D2 Phaser Benchtop Diffractometer

3.3.2. Raman Spectroscopy

Raman spectroscopy is a characterization technique used to determine the vibrational properties of solids by measuring the frequency shift during inelastic scattering of light by phonons in a sample. This occurs when a photon from light incident on the sample strikes a molecule in the sample and produces either: A scattered photon having a lower frequency than the original photon, a process known as Stokes Raman scattering or a higher frequency than the original photon referred to as anti-Stokes Raman scattering [11]. In the latter, the photon acquires its energy from the molecular bond when it already exists in an excited state. Generally, Raman spectroscopy measures the energy shift of the outgoing photon. Chemical composition of the molecules determines the shift in wavelength of the scattered light. The magnitude of the change in molecular polarization is determined by the intensity in Raman scattering.

A Raman spectrometer has four basic components, a radiation source, filters, sample (Raman) tube and spectrograph. A schematic diagram of the components is depicted in figure 3.5.

Radiation source

Due to the weak nature of Raman line, radiation of high intensity such as a laser is used. An excitation frequency which is high enough but will not result in photodecomposition is required. The mercury arc lamp was a preferable radiation source for meeting this requirement in the early 21th century. However, lasers are proving to be a more ideal radiation source and are quickly replacing mercury arc lamps. Using Helium-ion laser sources have thus become very common.

Argon-ion lasers are frequently employed when high intensity Raman lines are to be produced [11].

Filters

When non-monochromatic incident radiation is used as a source, there would be overlapping Raman shifts which would make interpreting the spectrum difficult. Therefore, using monochromatic light is of the essence. Monochromatic radiation is obtained through the use of filters. Common filters include quartz and nickel oxide.

Sample (Raman) Tube

Raman spectroscopy uses several different varieties of Raman tubes. Each with a size and shape that depends on the incident radiation, available amount of sample and the nature of the sample.

Spectrograph

In Raman spectroscopy the spectrograph used has to have high gathering power. Therefore, prisms of high resolving power as well as a short focus camera are used. The scattered radiation is directed to the slit of the spectrograph using a lens and the Raman lines obtained on a photographic plate. Although there are spectrographs that use photomultipliers or photographic emulsions, the photographic method is preferred due to high sensitivity to the low intensity of Raman lines.

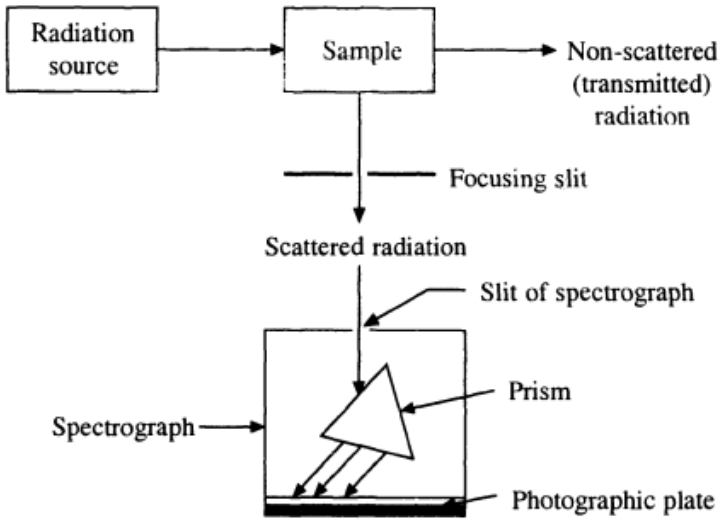

Figure 3.5. Schematic diagram of a Raman Spectrometer[11]

3.3.3. Transmission Electron Microscopy (TEM)

Transmission electron microscopy follows the same basic principle as that of an optical microscope but instead of light it uses electrons [12]. Due to the shorter wavelength of electrons as compared to those of light, the attainable resolutions for TEM are several orders of magnitude higher than that of the optical microscope. Three essential systems make up the TEM; (i) An electron gun, used for the production of the electron beam and a corresponding condenser system whose role is to focus the beam onto the sample, (ii) a system for imaging consisting of an objective lens, a movable specimen stage, a projector and intermediate lenses which focus the electrons that pass through the specimen forming a highly magnified real image, and (iii) and image-recording system used in converting the image from electrons into a form that can more easily be interpreted by the eye. The image-recording system normally consists of a fluorescent screen to enable focusing and viewing the image as well as a camera to capture permanent records. Different components of the TEM are shown in figure 3.6.

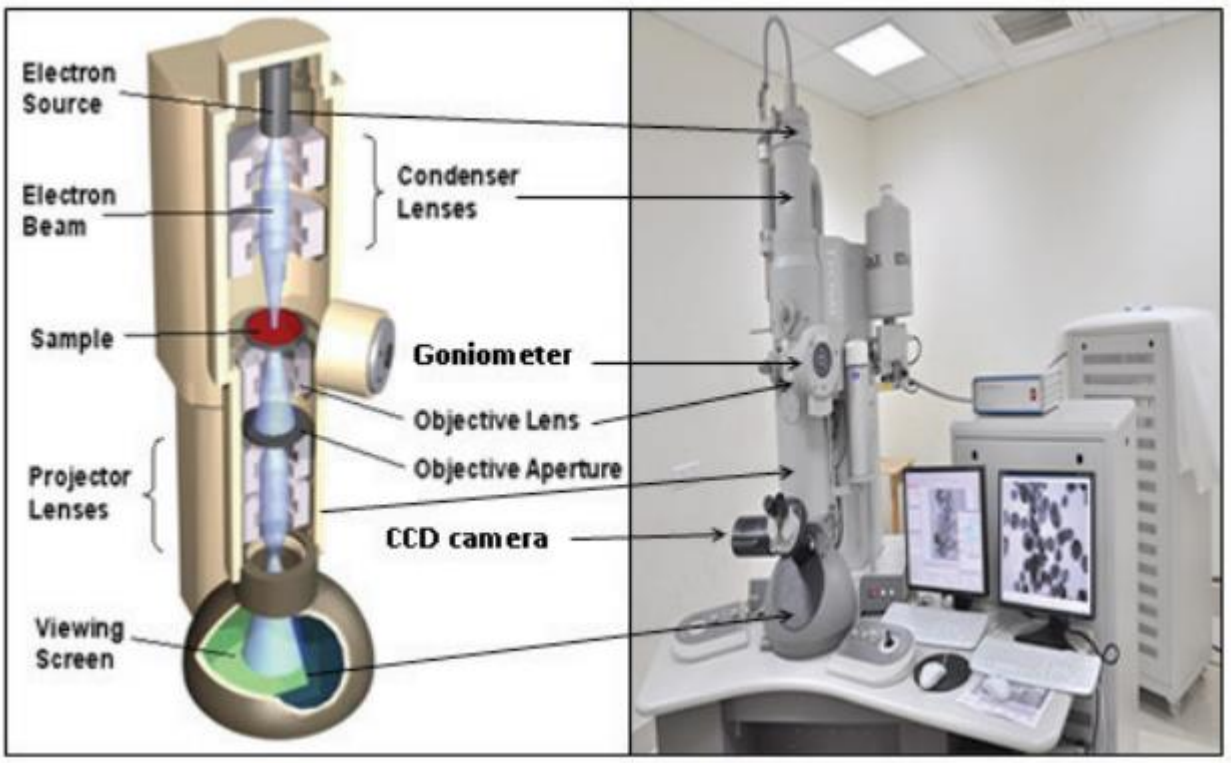

Figure 3.6 Transmission electron microscope[12]

3.3.4. Scanning Electron Microscopy (SEM)

The scanning electron microscope is a useful instrument for the analysis and examination of chemical composition characterizations and microstructure morphology at relatively high magnifications in comparison to traditional optical microscopes[12]. Figure 3.7 depicts the schematic diagram of a SEM system. The two basic components are (i) a microscope column and (ii) imaging controls.

The microscope column encloses the electron gun as well as lenses responsible for focusing the beam of electrons onto the surface of the specimen along with a detector. Typical electron energies used are in the 0.1 – 30 keV range. Two pairs of electromagnetic deflection coils comprise what is called the scan coils, these sweep the electron beam across the specimen. One pair deflects the beam off the optical axis while the other pair bends the electron beam back to the axis onto the focal point. Thus the beam is allowed to move in such a way that it forms a 'raster' on the specimen, which is viewed on the screen as it is generated. In this study a Zeiss GeminiSEM is used for surface imaging, this is shown in figure 3.7 (b).

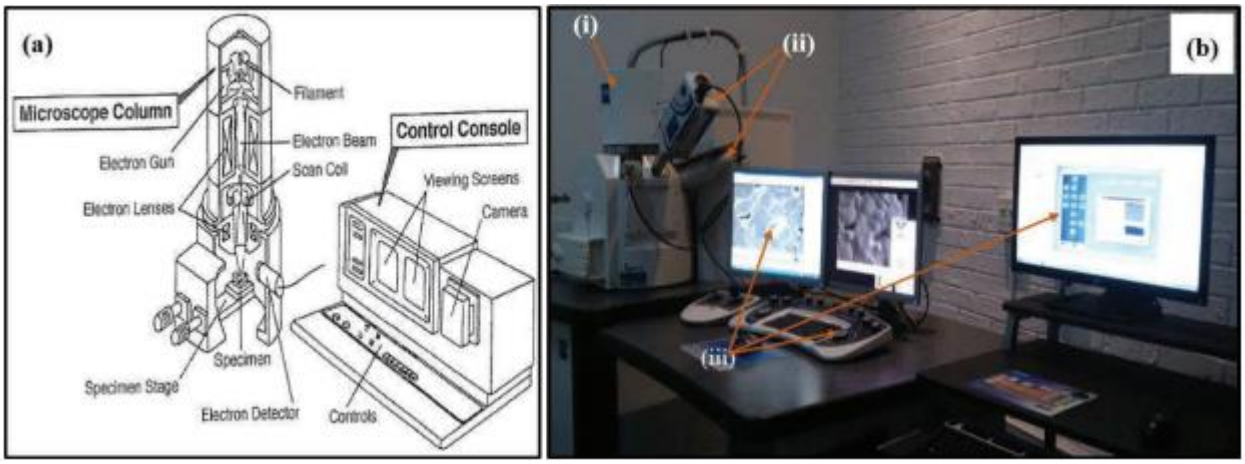

Figure 3.7. (a) primary components of a scanning electron microscope. (b) Zeiss GeminiSEM: (i) –the microscope column, (ii) – detector and (iii) – the screens with controls

3.3.5. Energy-Dispersive X-ray Spectroscopy (EDS)

For the identification of materials and contaminants they may contain, along with estimations of their relative concentration on the specimen's surface, energy-dispersive X-ray spectroscopy is used (EDS). Within SEM, the specimen is bombarded with a focused beam of electrons. The collision of the electron beam with the electrons in the specimen's atoms leads to their ejection from their bound energy levels. The unoccupied inner energy levels (holes) resulting from the electronic collision and ejection are subsequently occupied through electronic transitions from the outer shell leading to x-ray emission [13]. The process of transition is governed by quantum mechanical selection rules. The amount of energy in the x-rays being emitted from these transitions can be used to directly identify the atom from which the x-ray was released. This measurement is done during beam bombardment of the specimen.

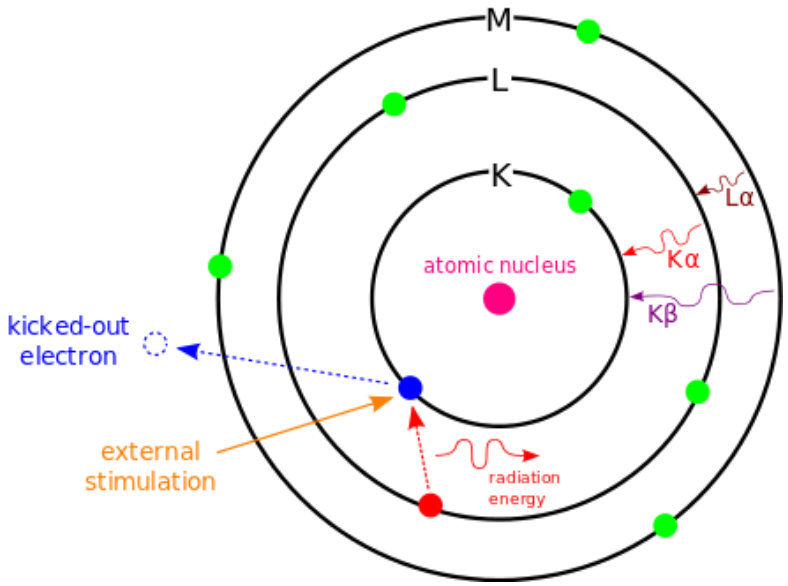

Figure 3.8. illustration of processes occurring during electronic excitation in EDS[14]

Each peak displayed in an EDS spectrum is unique fingerprint of an atom, this means each peak represents an individual element. The peak height in a spectrum determines the concentration of the element in the specimen. An EDS spectrum on top of identifying the element also gives the type of X-ray to which it corresponds. An electron of the higher energy shells will drop down to fill this vacancy and in doing so an x-ray photon is released with an energy equal to the difference

between the two levels involved. An example considering L to K transition is illustrated in figure 3.8. The same principle being valid for other X-ray energies.

3.3.6. UV-Visible Spectrometry (UV-Vis)

Spectroscopy can be defined as the study of the quantized interaction of electromagnetic radiations with matter. When the absorption of radiations in the visible and ultraviolet (UV) regions of the electromagnetic spectrum are of interest, UV and visible spectroscopy is employed. The visible region is in the 400 - 800 nm range while the UV region extends from 10 – 400nm in the electromagnetic spectrum [11]. When electromagnetic radiation is absorbed in the visible and UV regions electrons may move from lower valence band to higher energy conduction band. Because electronic transitions are involved, it is sometimes called electronic spectroscopy.

A plot of wavelength versus absorption intensity in terms of molar extinction coefficient ε or optical density A (for solutions and solids respectively) as defined by Lambert-Beer law is then retrieved from a UV-visible spectrophotometer. Lamberts law states that the ratio of incident monochromatic radiation which a homogeneous medium absorbs is independent of intensity of radiation. According to Beer's law, the monochromatic radiation absorbed by a homogeneous medium is proportional to the number of absorbing molecules. The Lambert-Beer law can be expressed as follows,

` $log\frac{I_0}{I} = A = \varepsilon cl,$

where I represents the intensity of the radiation which is transmitted, I_0 is the intensity of the incident radiation, A the optical density, ε the molar extinction coefficient, c the concentration and l is the path length in centimeters.

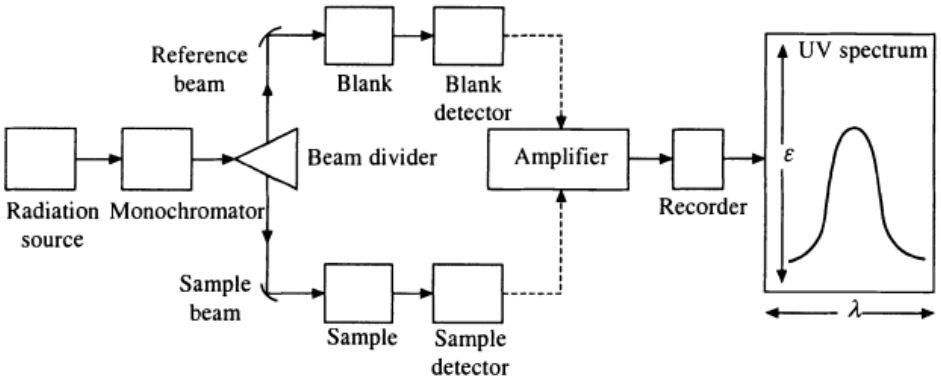

Figure 3.9. Schematic diagram of a UV-visible spectrophotometer

UV-visible spectrophotometers are usually double-beam instruments (for increased accuracy when measuring the absorption of samples) consisting of a radiation source, detectors, monochromator, recording system and amplifiers as depicted in figure 3.9. A hydrogen/ deuterium-discharge lamp is used as a source in the UV region (100 - 400nm) and a tungsten-filament lamp which is used in the visible region. A monochromator disperses the radiation from source to their separate wavelengths. Detectors use photomultipliers tubes to generate voltages which are proportional to the energy of radiation that strikes them. An amplifier then subtracts the absorption due to solvent from that of solution electronically and the recorder automatically plots the wavelength of absorbance radiation versus molar absorptivity ε or the optical density A. Absorption and reflectance spectra used in this study were taken using the Varian Cary 500 Uv-vis NIR spectrophotometer with measurements taken between 200 and 800 nm. This is depicted in figure 3.10.



Figure 3.10. Cary 500 UV-Vis NIR Spectrophotometer used in this study

3.3.7. Photoluminescence Spectroscopy

Photoluminescence spectroscopy (PL) is a non-destructive characterization technique whereby photons of light stimulate the emission of a photon from a material [15]. Light is then directed onto a sample and as photons from the incoming light are absorbed, a process known as photo-excitation occurs. Photo-excitation causes electrons in the material to move from a lower energy electronic state to a higher energy electronic state. As these electrons relax back to the initial ground electronic state, photon energy is released. Emission of light through such a process is known as photoluminescence (PL). The principle of photoluminescence spectroscopy is depicted in figure 3.11.

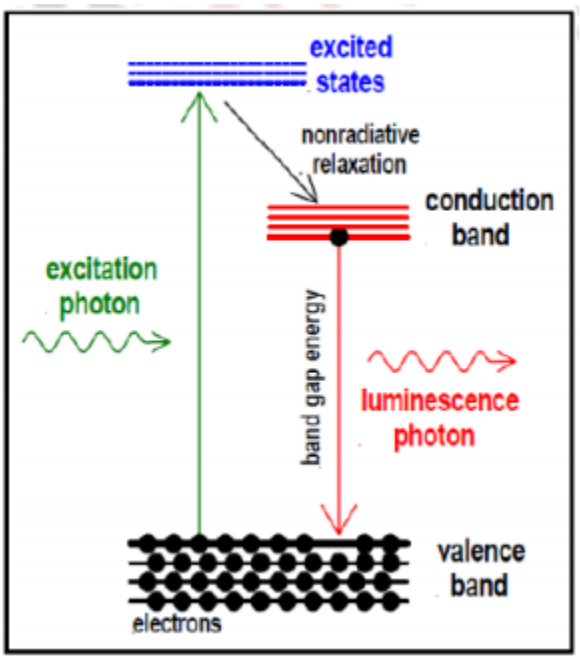

Figure 3.11. Principle of Photoluminescence spectroscopy[16]

A Photoluminescence spectrophotometer has four basic components, a radiation source, a monochromator, sample cell and a detector. A schematic diagram of the components is depicted in figure 3.12. The source can be any laser whose photon energy exceeds that of the band gap of the sample to be examined, whose power is sufficient to give an adequate signal. The monochromator selects the wavelength to transmit to the detector. In the schematic, lens L1 and L2 focus the PL signal; the filters F1 and F2 are used to block unwanted light; chopper C1 is for modulating lighting light for lock-in detection and the lamp S is for absorption spectroscopy[17] Figure 3.13 shows the Horiba system used in the study.

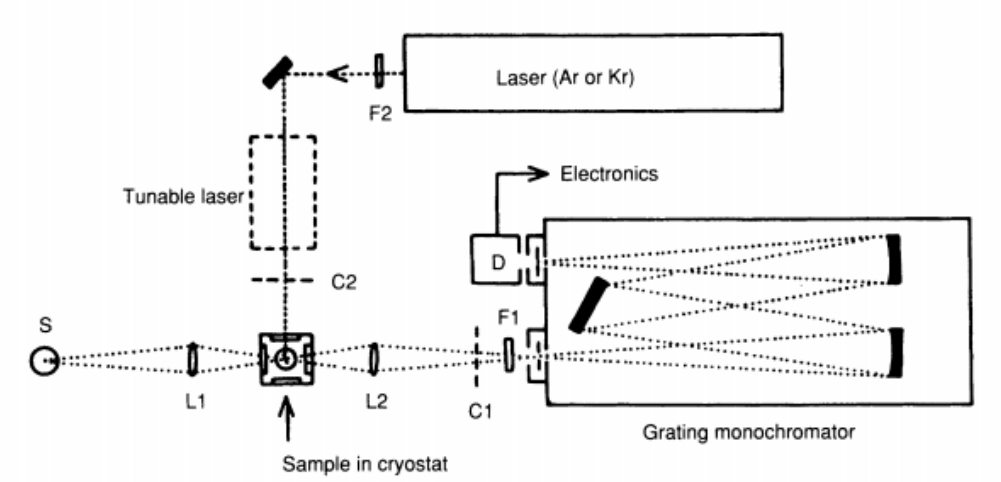

Figure 3.12. Schematic diagram of PL instrumentation[17]

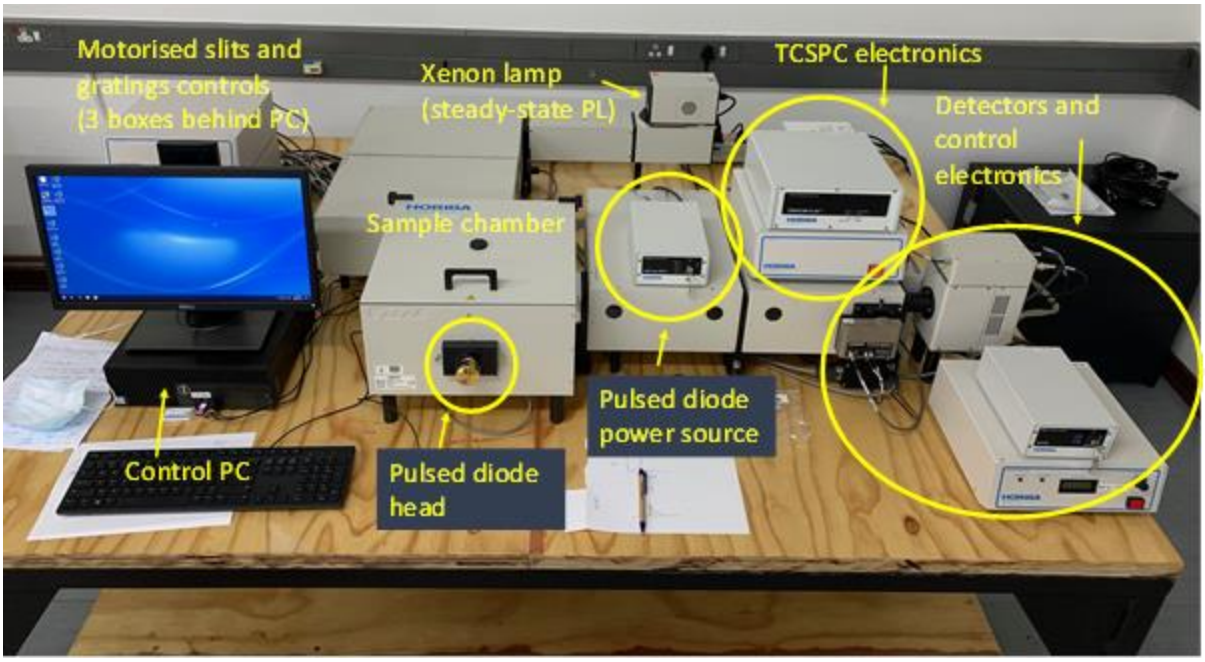

Figure 3.13. Horiba PL system used in this Study

3.3.8. Physical Property Measurement System (PPMS)

Magnetic measurements in this study were performed using the DynaCool PPMS 12T. It uses a two-stage pulse cooler to cool the temperature control system and the superconducting magnet and thus providing a low vibrational environment for sample characterization. It also provides

temperature sweep and precise field modes and continuous low temperature control. Temperature ranges from 1.8K – 400K. The DC Vibration Sample Magnetometer was used for the magnetization dependence on temperature and isothermal magnetization –field measurements. The set-up is shown in figure 3.14.



Figure 3.14. DynaCool PPMS 12T

References

[1] J. N. Hasnidawani, H. N. Azlina, H. Norita, N. N. Bonnia, S. Ratim, and E. S. Ali, "Synthesis of ZnO Nanostructures Using Sol-Gel Method," *Procedia Chem.*, vol. 19, pp. 211–216, 2016, doi: 10.1016/j.proche.2016.03.095.

[2] "X-ray Powder Diffraction (XRD)." https://serc.carleton.edu/research_education/geochemsheets/techniques/XRD.html (accessed Oct. 18, 2020).

[3] "Bragg's law. A two-dimensional crystal lattice and a set of imaginary... | Download Scientific Diagram." https://www.researchgate.net/figure/Braggs-law-A-two-dimensional-crystal-lattice-and-a-set-of-imaginary-planes-is_fig10_47418334 (accessed Oct. 18, 2020).

[4] "X-Ray Crystallography." https://www.tulane.edu/~sanelson/eens211/x-ray.htm (accessed Nov. 09, 2020).

[5] P. Bindu and S. Thomas, "Estimation of lattice strain in ZnO nanoparticles: X-ray peak profile analysis," *J. Theor. Appl. Phys.*, vol. 8, no. 4, pp. 123–134, 2014, doi: 10.1007/s40094-014-0141-9.

[6] V. Mote, Y. Purushotham, and B. Dole, "Williamson-Hall analysis in estimation of lattice strain in nanometer-sized ZnO particles," *J. Theor. Appl. Phys.*, vol. 6, no. 1, pp. 1–8, Dec. 2012, doi: 10.1186/2251-7235-6-6.

[7] "X-Ray diffractometer and its various component parts for X-Ray studies." http://xrd.co/component-parts-x-ray-diffractometer/ (accessed Nov. 09, 2020).

[8] T. Nottingham, “Termtanun , Mutsee (2013) Photocatalytic degradation of pesticides using TiO2 nanoparticles . PhD thesis , University of Nottingham . PHOTOCATALYTIC DEGRADATION OF PESTICIDES USING TIO2 NANOPARTICLES BY PHILOSOPHY NOVEMBER 2013,” no. November, p. 239, 2013.

[9] N. C. Gatsi, “Spectroscopy of trivalent neodymium ions (Nd3+) in zinc oxide (ZnO) thin films and powders,” no. May, 2019.

[10] “D2 PHASER Desktop Diffractometer from Bruker XRD.” https://www.azom.com/materials-video-details.aspx?VidID=894 (accessed Oct. 19, 2020).

[11] L. D. S. Yadav, *Organic Spectroscopy*. Springer Netherlands, 2005.

[12] “Transmission Electron Microscopy (TEM).” https://warwick.ac.uk/fac/sci/physics/current/postgraduate/regs/mpagswarwick/ex5/techniques/structural/tem/ (accessed Nov. 09, 2020).

[13] M. Scimeca, S. Bischetti, H. K. Lamsira, R. Bonfiglio, and E. Bonanno, “Energy Dispersive X-ray (EDX) microanalysis: A powerful tool in biomedical research and diagnosis,” doi: 10.4081/ejh.2018.2841.

[14] “Energy-Dispersive X-ray Spectroscopy (EDS) - Chemistry LibreTexts.” https://chem.libretexts.org/Courses/Franklin_and_Marshall_College/Introduction_to_Materials_Characterization__CHM_412_Collaborative_Text/Spectroscopy/Energy-Dispersive_X-ray_Spectroscopy_(EDS) (accessed Nov. 09, 2020).

[15] “Photoluminescence (PL) & Electroluminescence (EL) - HORIBA.” https://www.horiba.com/en_en/products/by-technique/molecular-

spectroscopy/photoluminescence-pl-electroluminescence-el/ (accessed Nov. 09, 2020).

[16] V. Russo, M. Ghidelli, P. Gondoni, C. S. Casari, and A. L. Bassi, “Multi-wavelength Raman scattering of nanostructured Al-doped zinc oxide.”

[17] F. Transforms *et al.*, *Optical Characterization of Semiconductors*. 1993.

Chapter 4 – Structural, Optical and Morphological Characterizations of Mg/Ga co-doped ZnO nanoparticles

4.1. Introduction

ZnO is a semiconductor with an ionicity that lies borderline between ionic and covalent semiconductors. At room temperature and standard pressure, ZnO has a wurtzite structure as the thermodynamically stable phase [1]. The exceptional properties of ZnO such as its large free-exciton binding energy (60 meV), direct band gap 3.37 eV (at 300K) [2], thermal stability, high mechanical strength, negative electron affinity, chemical stability and high radiation hardness enables its diverse application in light emitting devices, high temperature and transparent electronics [3]. Various commercial applications have reported the use of ZnO in sensors, photodegradation and photocatalysis, solar cells and liquid crystal displays [4].

This chapter presents the results from different characterization techniques used to analyze the structure, particle morphology and optical properties of ZnO and Mg-Ga co-doped ZnO samples. These samples were annealed at 500°C to improve both their optical properties and degree of crystallinity. The results have been correlated and the fundamental properties and parameters are presented.

4.2. Morphological Studies

4.2.1. Scanning Electron Microscopy (SEM)

The morphology of the samples was analyzed using scanning electron microscopy (SEM). Figure 4.1. (a - d) shows the SEM images of undoped ZnO, 3 mol % Mg doped ZnO, 3 mol % Ga doped ZnO and 3 mol % Mg-Ga co-doped ZnO, respectively. All the samples were annealed at 500°C. Figure 4.1 (a, c, d) the powders were made up of rod like structures which agglomerated together to form nanoflowers consistent with the data reported in ref [11], while in Fig 4.1 (b) it is clear that the powder was made up of an agglomeration of nanospheres.

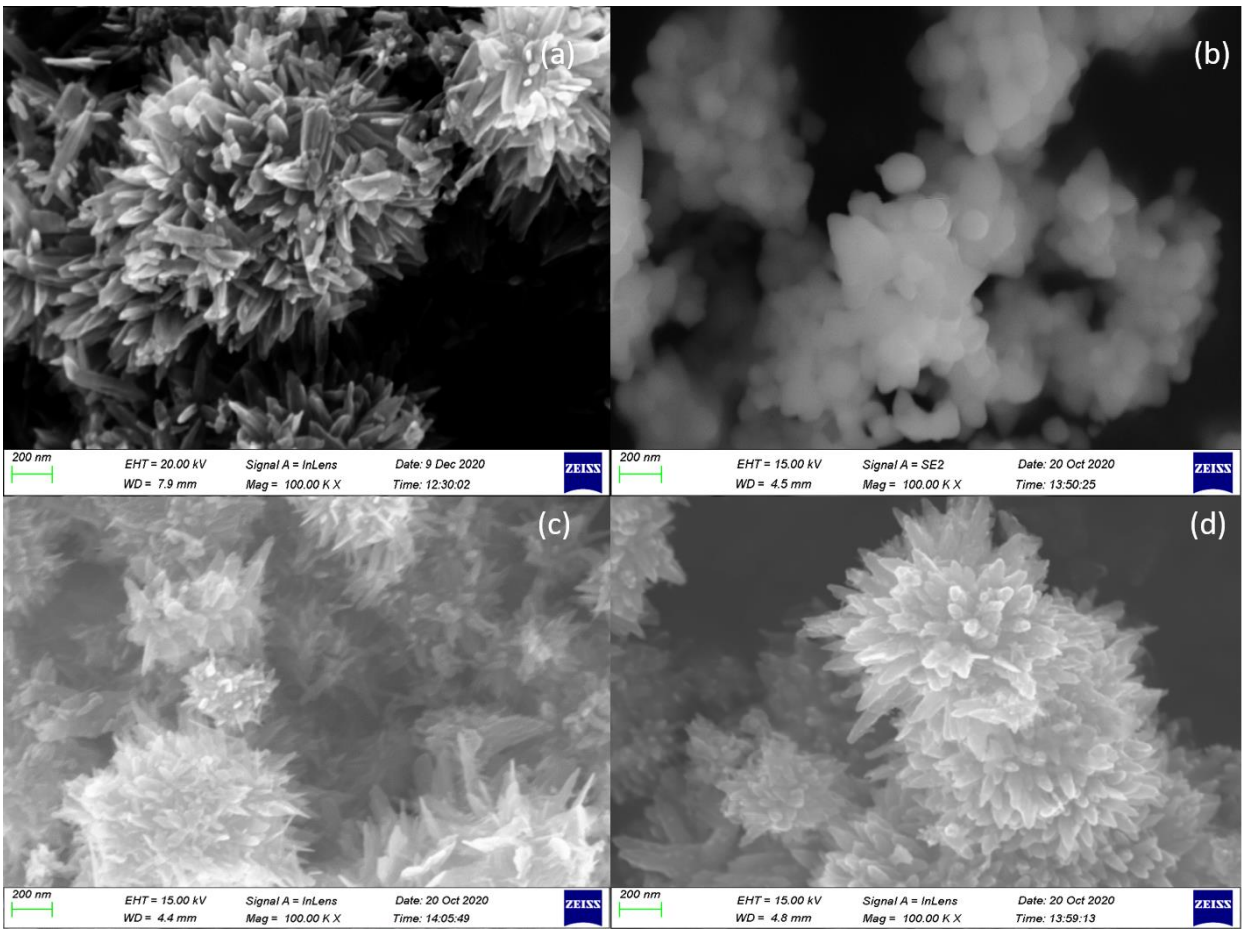

Figure 4.1. (a),(b),(c),(d) SEM images for undoped ZnO, 3% Mg doped ZnO, 3% Ga doped ZnO and 3% co-doped ZnO.

4.2.2. Energy Dispersive Spectroscopy

Figure 4.2 shows the EDS mapping of 3 mol% Mg and Ga co-doped ZnO nanoparticles. The mapping shows a non-homogeneous distribution of each element on the surface. The EDS spectra of the four samples in Fig. 4.3 confirmed the presence of elements including Zn, O, Mg and Ga. Table 4.1 shows the weight percentages of each element. Though the samples were doped with 3 mol% of either Mg or Ga., The differences in weight percentage suggests that the reaction was not 100% efficient and that some of the precursors were washed away in the solvent.

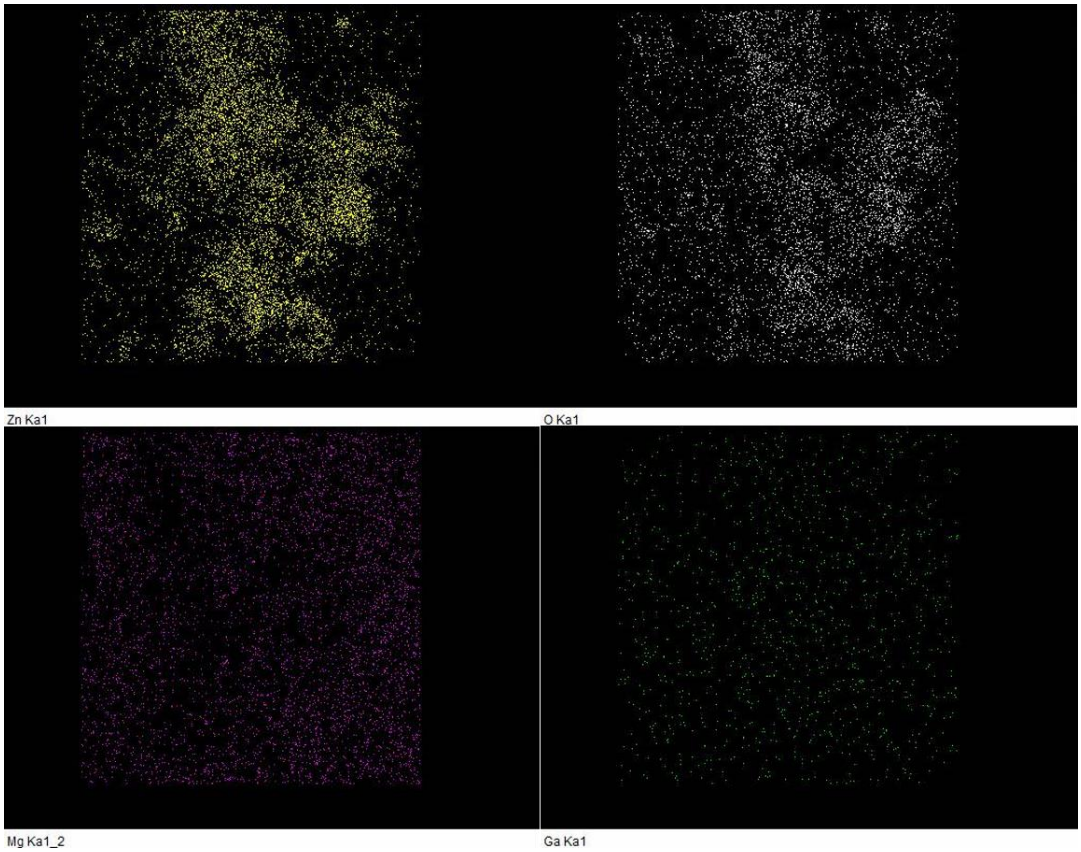

Figure 4. 2. EDS mapping of co-doped ZnO.

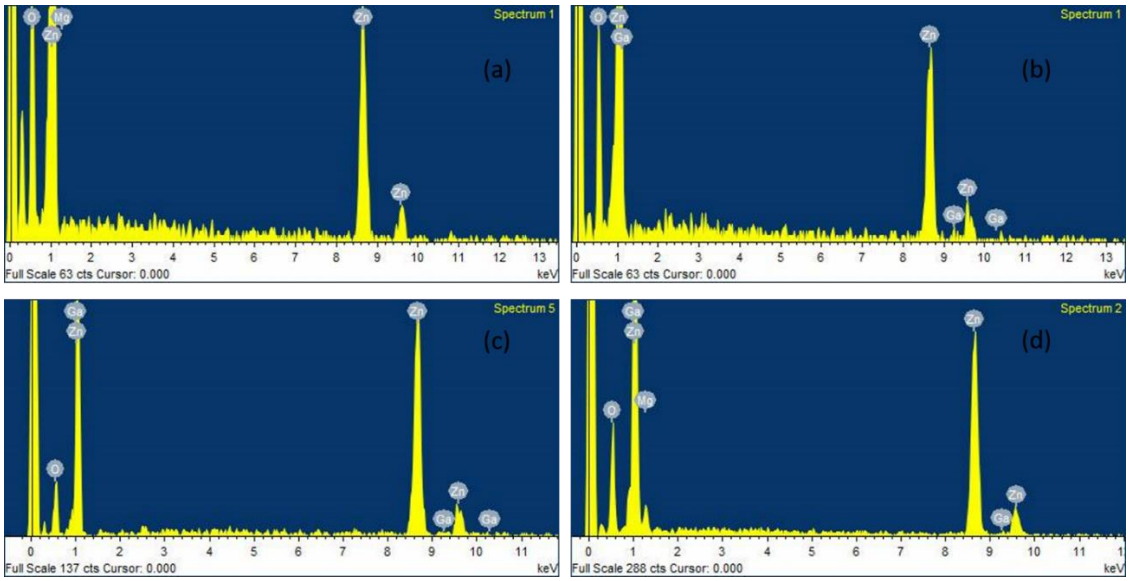

Figure 4.3. EDS spectra of Undoped ZnO, 3% Mg doped ZnO, 3% Ga doped ZnO and 3% co-doped ZnO (a-d).

Table 4.1. Elemental composition of the ZnO samples

Sample	Element	Weight %
Undoped ZnO	Zn	80.26
	O	19.74
3 mol % Mg doped ZnO	Zn	70.39
	Mg	1.15
	O	28.46
3 mol % Ga doped ZnO	Zn	82.88
	Ga	1.24
	O	15.87
3 mol % co-doped ZnO	Zn	71.07
	Mg	1.90
	Ga	6.93
	O	20.10

4.2.3. Transmission Electron Microscopy

TEM images of undoped ZnO and 3 mol% of Mg-Ga co-doped ZnO, both samples annealed at 500°C, are shown in Fig. 4.4. Consistent with the SEM images, the TEM images shows that the particles were made up of nanoflowers formed by agglomeration of rod-like nanostructures. Similar results were reported in ref [22].

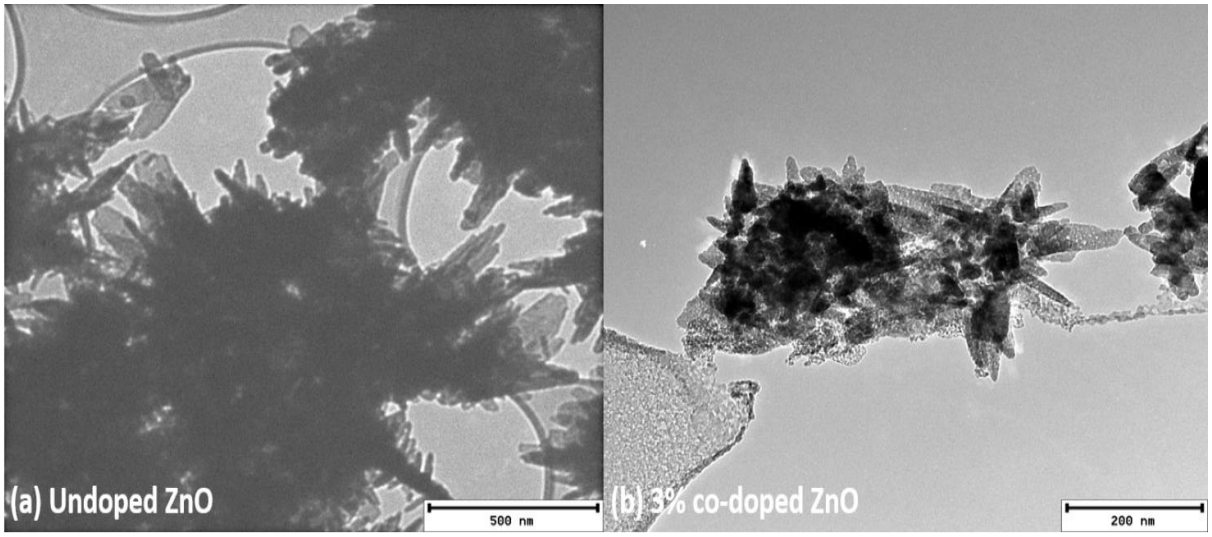

Figure 4.4. TEM images for undoped ZnO and 3% co-doped ZnO

4.3. X-Ray Diffraction (XRD)

The XRD patterns of the as prepared and annealed undoped ZnO are shown in figure 4.5. The peaks were indexed to the Miller indices (001), (002), (101), (102), (100), (110), (200), (112), (201), (004) and (202) corresponding to the wurtzite structure of ZnO. The wurtzite belongs to the space group $P6_3mc$ reported in the standard ICSD card/file no 180052 [5]. The sharp peaks suggest that the materials are highly crystalline. The most intense diffraction peak at $2\theta = 35.8°$ indicates a preferred orientation along the [101] direction of the ZnO phase [6]. The values of the interplanar spacing d_{hkl} of the ZnO samples were calculated using equation (4.1). The lattice parameters *a* and *c* of the hexagonal wurtzite structure were calculated by applying Eqns. (4.2 and 4.3) to the (100) and (002) peaks, respectively. The *u* parameter is defined as the length of the bonds parallel to the c-axis and it used as the positional parameter of the wurtzite structure. The values have been determined to be 3.25Å and 5.21Å for the undoped and annealed ZnO powder. Rietveld refinement

(carried out by FullProf software) for the annealed samples as shown in figure 4.9 and the lattice parameters determined are in agreement with those calculated using equations (4.1) – (4.3).

$$n\lambda = 2dsin\theta \qquad (4.1)$$

$$a = \frac{\lambda}{\sqrt{3}\sin\theta_{(100)}} \qquad (4.2)$$

$$c = \frac{\lambda}{\sin\theta_{(002)}} \qquad (4.3)$$

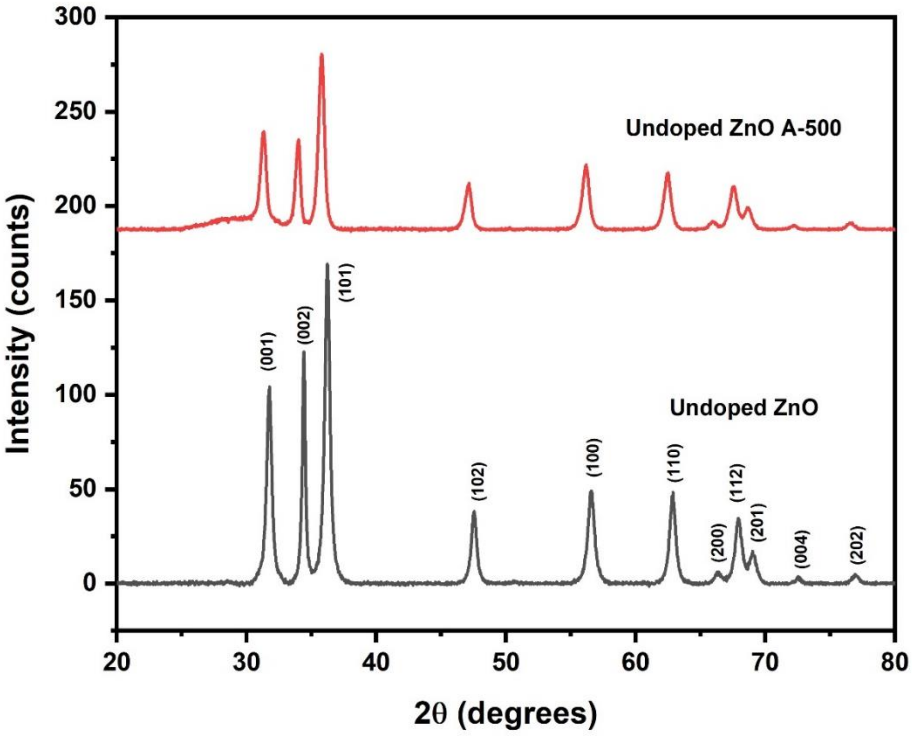

Figure 4.5. XRD pattern of as prepared ZnO and ZnO annealed at 500°C. The patterns have been stacked by Y-offset for ease of comparison of the peak positions and their intensity distributions.

Table 4.2. Crystallographic Parameters extracted from XRD analysis of ZnO, as prepared and annealed at 500°C.

Undoped ZnO powder	**2θ**	**FWHM**	**d spacing**	**Lattice Parameters (Å)**		***c/a***	**Crystallite size (S)**	***u* Parameter**
	(deg)	(rad)	(nm)	*a*	*c*		(nm)	
As prepared	34.42	4.16×10^{-3}	2.60	3.25	5.21	1.600	14.99	0.3797
Annealed 500°C	33.97	2.49×10^{-3}	2.64	3.30	5.27	1.597	22.20	0.3807

Figure 4.6 depicts the XRD patterns of annealed and unannealed 3 mol% Mg doped ZnO nanopowders. The diffraction peaks conform to the Miller indices associated with a hexagonal wurtzite structure of ZnO. The X-ray diffraction patterns do not exhibit any additional peaks corresponding to impurity phases after incorporating 3 mol% of Mg in the pristine and annealed phases. Thus a pure phase of hexagonal wurtzite ZnO is attained with 3% Mg dopants. Additionally, the diffraction pattern of the annealed sample exhibit sharper and more intense peaks than those of the unanealed samples suggesting that annealing improves the crystallinity of ZnO.

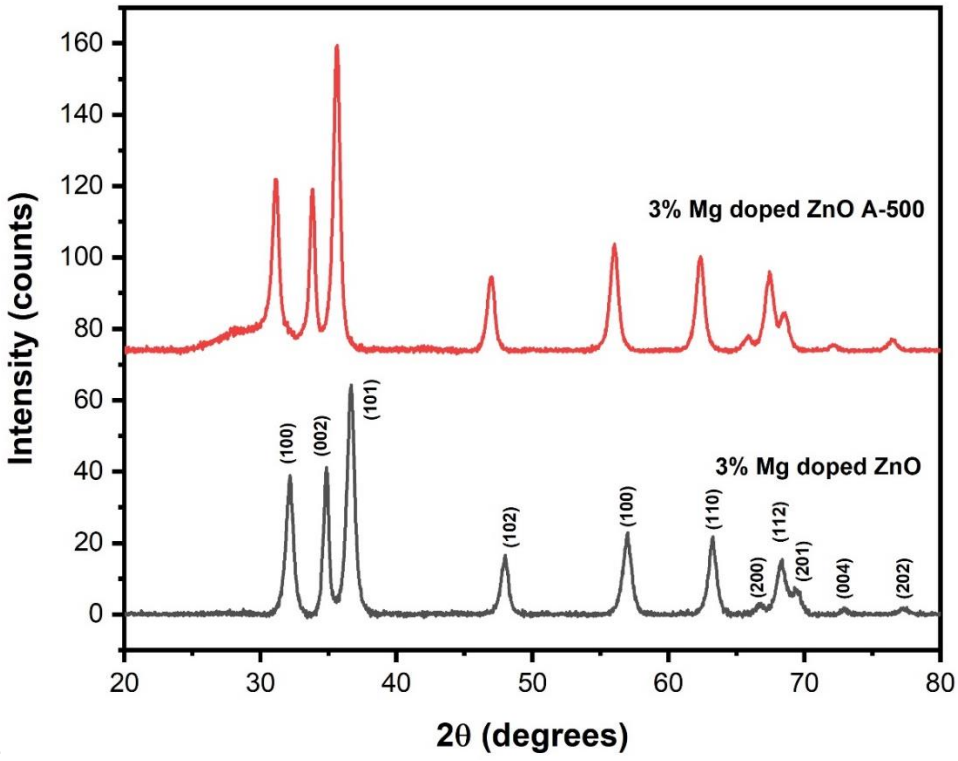

Figure 4.6. XRD patterns of as Prepared 3% Mg doped ZnO and the sample annealed at 500°C

Table 4.3 lists the lattice parameters deduced from the analysis of the XRD patterns. A 2**θ** shift of ~1.02° between the as prepared and 500°C annealed 3 mol% Mg doped ZnO is significantly larger than that between the as prepared and annealed ZnO. We attribute this shift to the incorporation of Mg^{2+} (ionic radius = 0.66 Å) in the lattice sites of Zn^{2+} whose ionic radius is larger (0.74 Å). Also, the lattice parameters a and c were different for as prepared and annealed 3% Mg doped ZnO.

Table 4.3. Lattice parameters of 3% Mg doped ZnO samples.

Powder sample	**2θ**	**FWHM**	**Plane spacing, *d***	**Lattice Parameters (Å)**		***c/a***	**Crystallite size (S)**	**U Parameter**
	(deg)	(rad)	(nm)	*A*	*c*		Nm	
3% Mg doped ZnO	34.84	4.68×10^{-3}	2.57	3.21	5.15	1.60	12.64	0.3795
3% Mg doped ZnO A-500	33.82	4.44×10^{-3}	2.65	3.32	5.30	1.60	13.16	0.3808

Figure 4.7. shows the XRD patterns of as prepared and annealed 3 mol % Ga doped ZnO samples. The pure phase of hexagonal (wurtzite) type structure of ZnO was indexed to the standard diffraction peaks and their corresponding Miller indices. Using the diffraction patterns and thermodynamic arguments based on the heats of formation of Ga_2O_3 it is reasonable to conclude that no impurity phases were observed with gallium doping.

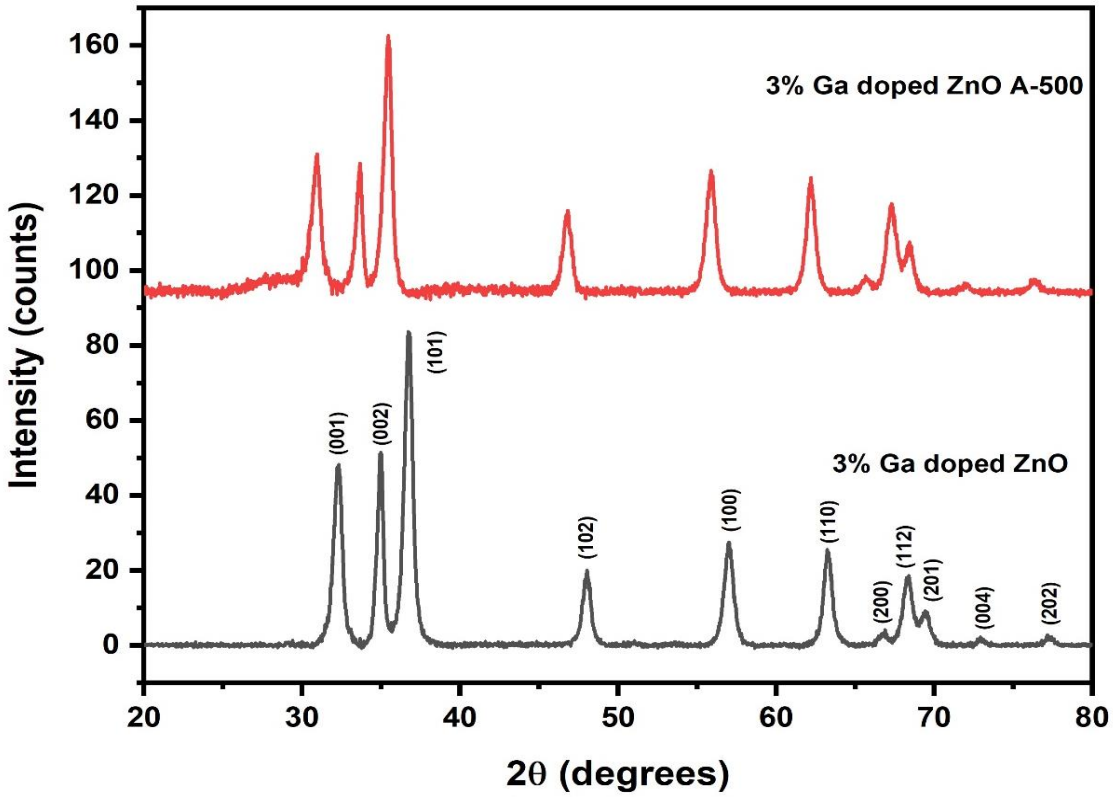

Figure 4.7. XRD patterns of as prepared and annealed 3% Ga doped ZnO.

In table 4.4, there is a significant change in the lattice parameters *a* and *c*, and the resulting c\a ratio deviates significantly from the literature value of 1.633 [7] at 1.66 and 1.59 for the as prepared and annealed samples, respectively. The change in lattice parameter values may be attributed to substitution of Ga^{3+} ions in Zn sites which cause the (M-O, M is the Zn or Ga) bonds to stretch along the a-b plane to stabilize the ZnO structure.

Table 4.4. Lattice parameters for the 3% Ga doped ZnO samples

Powder sample	**2θ**	**FWHM**	**Plane spacing, *d***	**Lattice Parameters (Å)**		***c/a***	**Crystallite size (S)**	**U Parameter**
	(deg)	(rad)	(nm)	*a*	*c*		Nm	
3% Ga doped ZnO	34.95	4.64×10^{-3}	2.57	3.21	5.34	1.66	12.34	0.3705
3% Ga doped ZnO A-500	33.62	4.42×10^{-3}	2.66	3.34	5.32	1.59	13.52	0.3814

Figure 4.8 shows the XRD patterns of as prepared and annealed Mg-Ga co-doped ZnO powder. The concentration of Mg and Ga was maintained at 3 mol% for each ion in the ZnO matrix. From the figure, the presence of peaks designated by the Miller indices confirm the hexagonal wurtzite structure of ZnO, and the sharp peaks observed indicate high crystallinity. Also, 3 mol% of Mg and Ga did not influence the crystalline structure of ZnO as no peaks corresponding to Ga and magnesium impurity phases were identified.

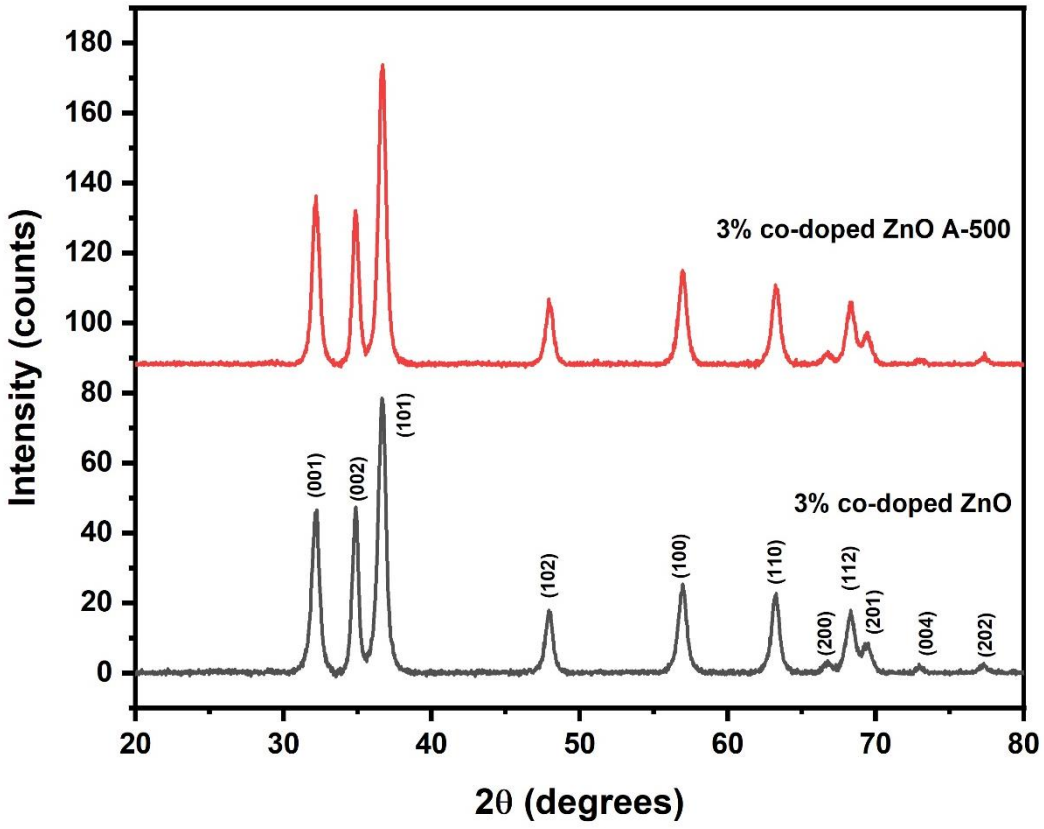

Figure 4.8. XRD patterns for as prepared 3% co-doped ZnO and 3% co-doped ZnO annealed at 500°C

Table 4.5 presents the lattice parameters derived from the XRD patterns of the 3 mol % Mg-Ga co-doped ZnO samples. Contrary to what was seen in previous patterns, there is a slightly significant shift in the 2**θ** values of the samples upon annealing. The lattice parameters a and c are seen to have no significant change.

Table 4.5. Lattice parameters obtained from XRD analysis of 3% co-doped ZnO samples.

Powder sample	**2θ**	**FWHM**	**Plane spacing, *d***	**Lattice Parameters (Å)**		***c/a***	**Crystallite size (S)**	**U Parameter**
	(deg)	(rad)	(nm)	*a*	*c*		nm	
3% co-doped ZnO	34.84	4.72×10^{-3}	2.57	3.21	5.15	1.60	13.56	0.3795
3% co-doped ZnO A-500	34.86	4.58×10^{-3}	2.57	3.21	5.14	1.60	13.99	0.3800

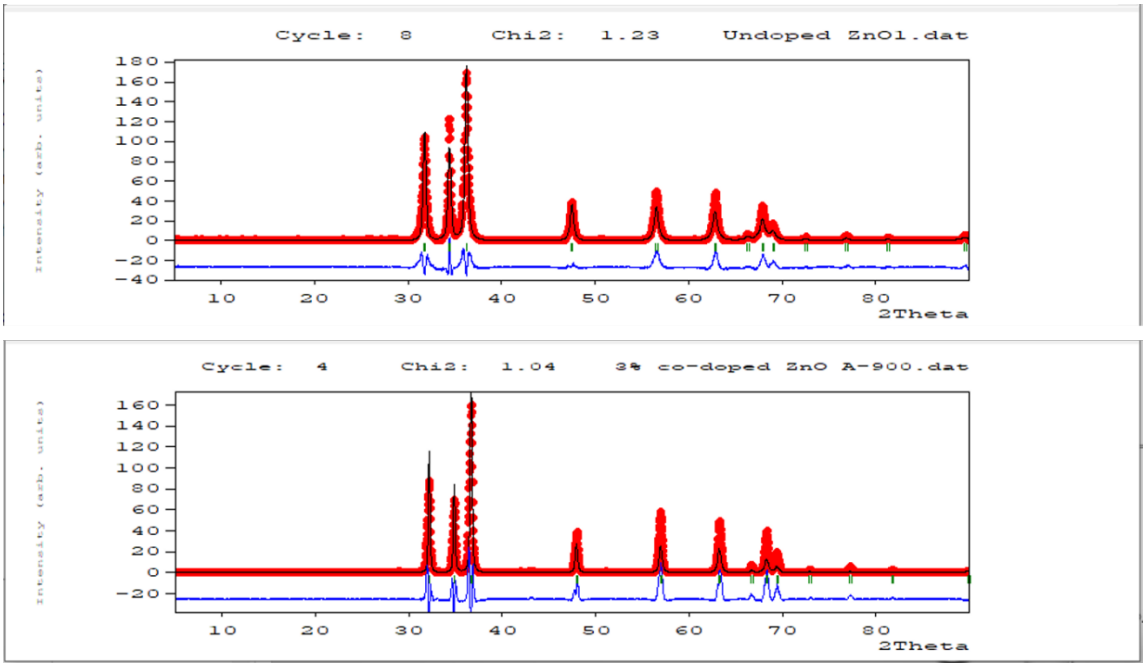

Figure 4.9. Rietveld Refinement run using using FullProf Software.

Figure 4.9 illustrates a rietveld refinement run using FullProf software. This technique was used as a verification method on the quality of lattice parameters values using the entire data set. This method utilizes the least squares fitting technique to refine a theoretical line until it matches the measured profile. The blue line represents the residue which should be a straight line if the fit quality is good. Though the χ^2 values are appropriate, the quality of the fit is lacking and could be improved through further refinement. However, for this investigation this level of quality is acceptable.

4.4. Raman Spectroscopy

Raman spectroscopy is used as an identification tool to detect vibrational modes in solids, and it is also capable of probing the chemical phase. In figure 4.10., the Raman spectra of undoped, Mg and Ga doped ZnO are plotted together stacked by a Y offset. An Argon ion laser of excitation wavelength 514.5 nm was used while recording the spectra from 89 – 1890 cm^{-1} range. The basic modes of wurtzite hexagonal ZnO were detected at 100, 381, 438 and 583 cm^{-1} which respectively

represent E_2(low), A_1(TO), E_2(high) and A_1(LO)/E_1(LO) [8]. The second order phonon mode at 203 cm^{-1} is assigned to $2E_2$(low) mode. Multi phonon modes observed at 332, 509, 660 and around 1110 cm^{-1} are assigned to E_2(high) - E_2(low), E_1(TO) + E_2(low), 2(E_2(high) – E_2(low)), and A_1(TO) + E_1(TO) + E_2(low), respectively [9].

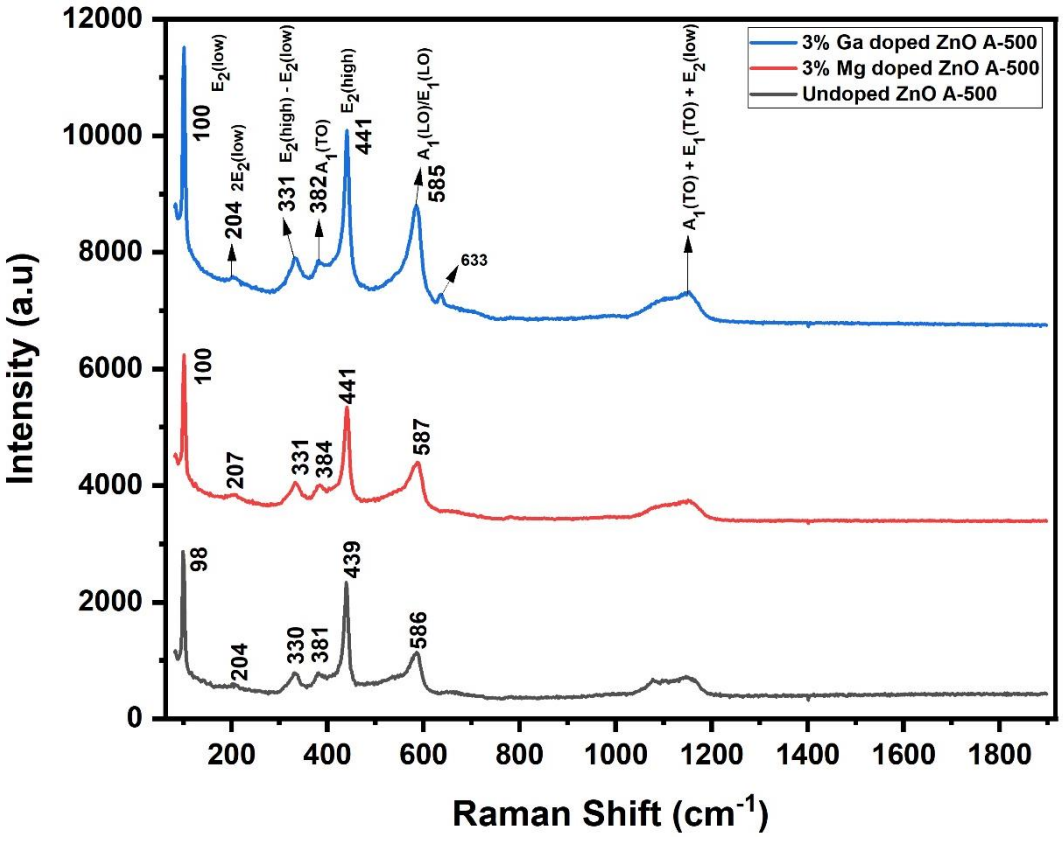

Figure 4.10. Raman spectra of undoped ZnO, 3% Mg doped and 3% Ga doped ZnO samples annealed at 500°C using excitation wavelength of 514.5 nm

All spectra show a prominent peak at 439 cm^{-1} for undoped ZnO and 441 cm^{-1} for both Mg and Ga doped ZnO samples. This prominent peak is the E_2(high) mode assigned to the hexagonal wurtzite structure of ZnO. The red shifting to 441 cm^{-1} observed in the doped samples is due to the introduction of dopants in the ZnO matrix. This E_2(high) mode is a non-polar mode associated with vibrations of oxygen atoms [10]. Another non-polar mode is the E_2(low) mode at 98 cm^{-1} in undoped ZnO and 100 cm^{-1} in Mg and Ga doped samples. The E_2(low) mode is associated with vibrations of Zn atoms and the incorporation of Mg and Ga in the lattice resulted in the peak shift. The peak at 381 cm^{-1} in undoped ZnO is caused by anisotropic nature of the force constant and the

peak position in the doped samples changes as a result of the variation of this force. The peak observed at 330 cm^{-1} is due to the acoustic overtone processes [11]. The peak at 586 cm^{-1} in undoped ZnO arises due to oxygen imperfection and broadens in the Mg doped sample while increasing in intensity in the Ga doped sample, this indicates an increase in oxygen related defects such as interstitials and vacancies [11]. A new peak is observed in the Ga doped sample at 633 cm^{-1}. Although not a Ga peak, it is attributed to intrinsic defects which likely arise due to lattice imperfections associated with the introduction of Ga [12]. The low intensity peak in the region between 1050 – 1200 cm^{-1} is assigned to optical overtones associated with the second order Raman active modes.

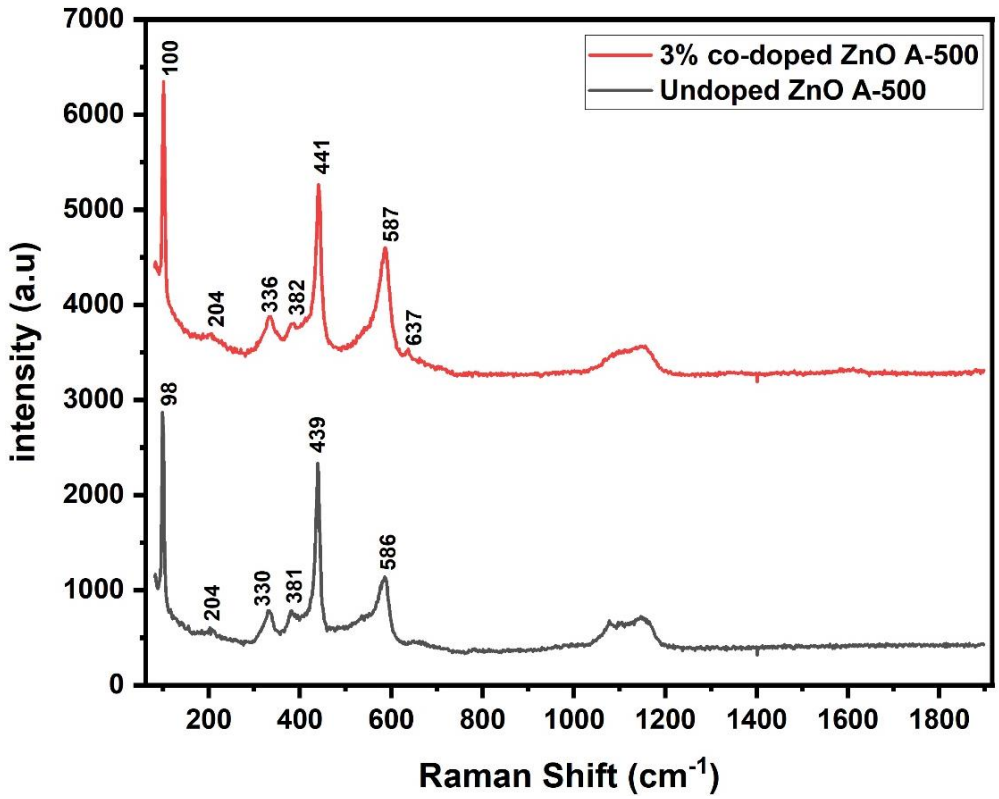

Figure 4.11. Raman spectra of undoped ZnO and co- doped ZnO samples annealed at 500°C

In figure 4.11. undoped and Mg-Ga co-doped ZnO Raman spectra is plotted stacked by Y offset. The non-polar modes E_2(low) and E_2(high) modes are observed at 98 cm^{-1} and 439 cm^{-1} in undoped ZnO and 100 cm^{-1} and 441 cm^{-1} for co-doped ZnO respectively. The peak at 330 cm^{-1} in undoped ZnO and the one at 336 cm^{-1} in Mg-Ga co-doped ZnO point to the increase in acoustic overtone processes [13]. An increased intensity of the peak at 587 cm^{-1} in the co-doped sample

indicates an increase in the amount of oxygen related defects. A peak between 633 - 640 cm^{-1} is due to asymmetry effect induced by gallium.

4.5. UV-Visible Spectroscopy

Figure 4.12 presents the diffuse reflectance spectra of undoped and Mg and Ga co-doped ZnO nanoparticles. From the spectra it is observed that there is reduced diffuse reflectance with the introduction on dopants, with the co-doped sample showing the least reflectance. This is attributed to increased crystal quality of the ZnO with the introduction of the dopants and may also be due to changes in the particle morphology of the samples [14].

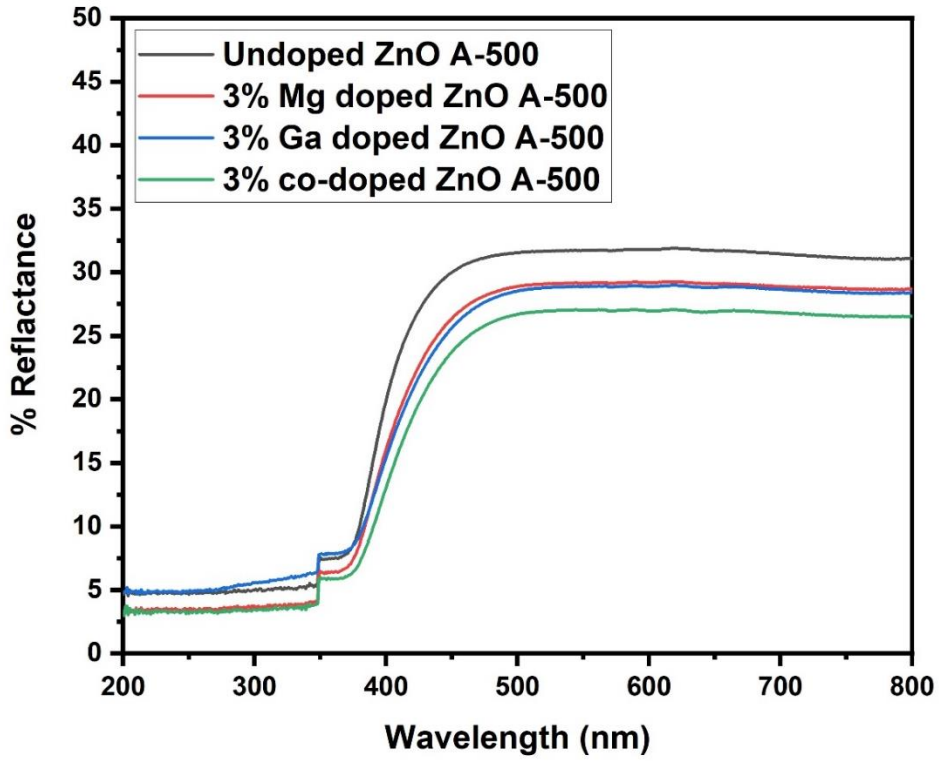

Figure 4.12. Diffuse reflectance plot of ZnO samples. The dip seen around 350 nm is an instrumental artifact due to switch over of the tungsten and deuterium lamps to allow for visible and UV illumination, respectively.

The diffuse reflectance data from figure 4.13 was used to evaluate the absorption coefficients from Kubelka-Munk function defined as follows:

$$F(R_\infty) = \frac{\alpha}{S} = \frac{(1 - R_\infty)^2}{2R}$$

Where ‘α’ is the absorption coefficient, ‘S’ the scattering coefficient and $F(R_\infty)$ denotes the Kubelka-Munk function. With regard to diffuse reflectance spectra, Kubelka-Munk function can be used instead of the absorption coefficient ‘α’ for the evaluation of the optical bandgap energies. This is done by plotting $(F(R_\infty)E)^2$ versus E(eV) which is linear near the edge for direct allowed transitions (η = 1/2) [14].

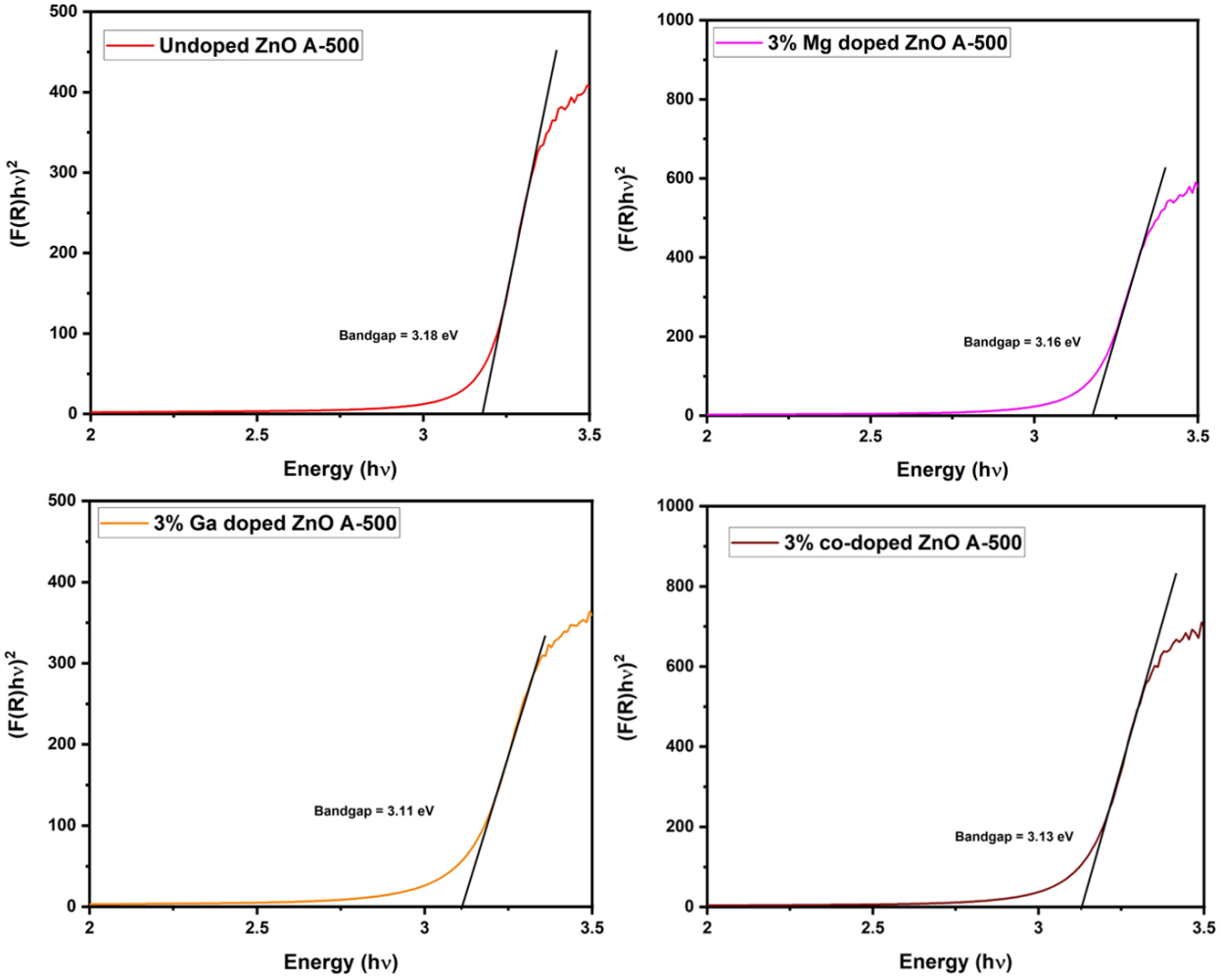

Figure 4.13. Band gap energies of ZnO samples as deduced from diffuse reflectance measurements.

In this study, the band gap energies were found to be 3.18 ± 0.01, 3.16 ± 0.02, 3.11 ± 0.05, 3.13 ± 0.01 eV for undoped ZnO, Mg doped ZnO, Ga doped ZnO and Mg-Ga co-doped ZnO, respectively as shown in figure 4.13. The 3 mol% Ga doped ZnO produced the smallest bandgap energy followed by the co-doped ZnO with the Mg and undoped with slightly higher value. This decreased

band gap energies are attributed to increased crystallinity of the samples, which is consistent with the XRD data. These values are lower that the bulk literature value of ZnO (~3.37 eV). Quantum confinement effects were not prominent as particles were of rod-like shape and not full nanoparticles as seen in TEM. The extension of energies below the band gap value is indicative of structural defects present in the samples and it is discussed in detail using the photoluminescence data.

The band gap energies with samples prepared at room temperature were compared to those annealed at 500 and 900°C (done for comparison purposes) to assess the effects of annealing on annihilation of structural defect and subsequently on the band gap. Figure 4.14 shows that the band gap energies decrease initially when temperature was increased up to 500 °C and then increases thereafter.

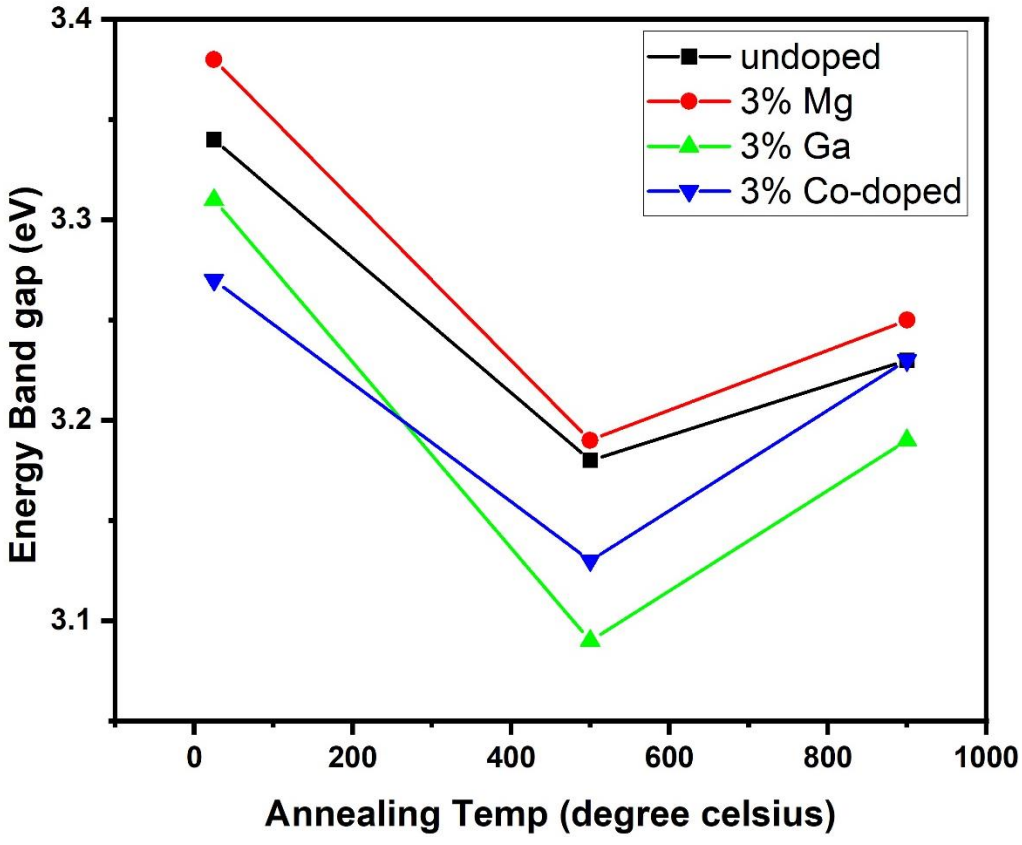

Figure 4.14. Band gap energy at various annealing temperatures for undoped and 3% doped ZnO powders.

4.6. Photoluminescence Measurement

Figure 4.15. (a-d) depicts the room temperature photoluminescence spectra of pristine and Mg/Ga doped ZnO samples recorded when exciting at the wavelength of 320 nm using a monochromatized xenon lamp. The spectra were de-convoluted using Gaussian functions.

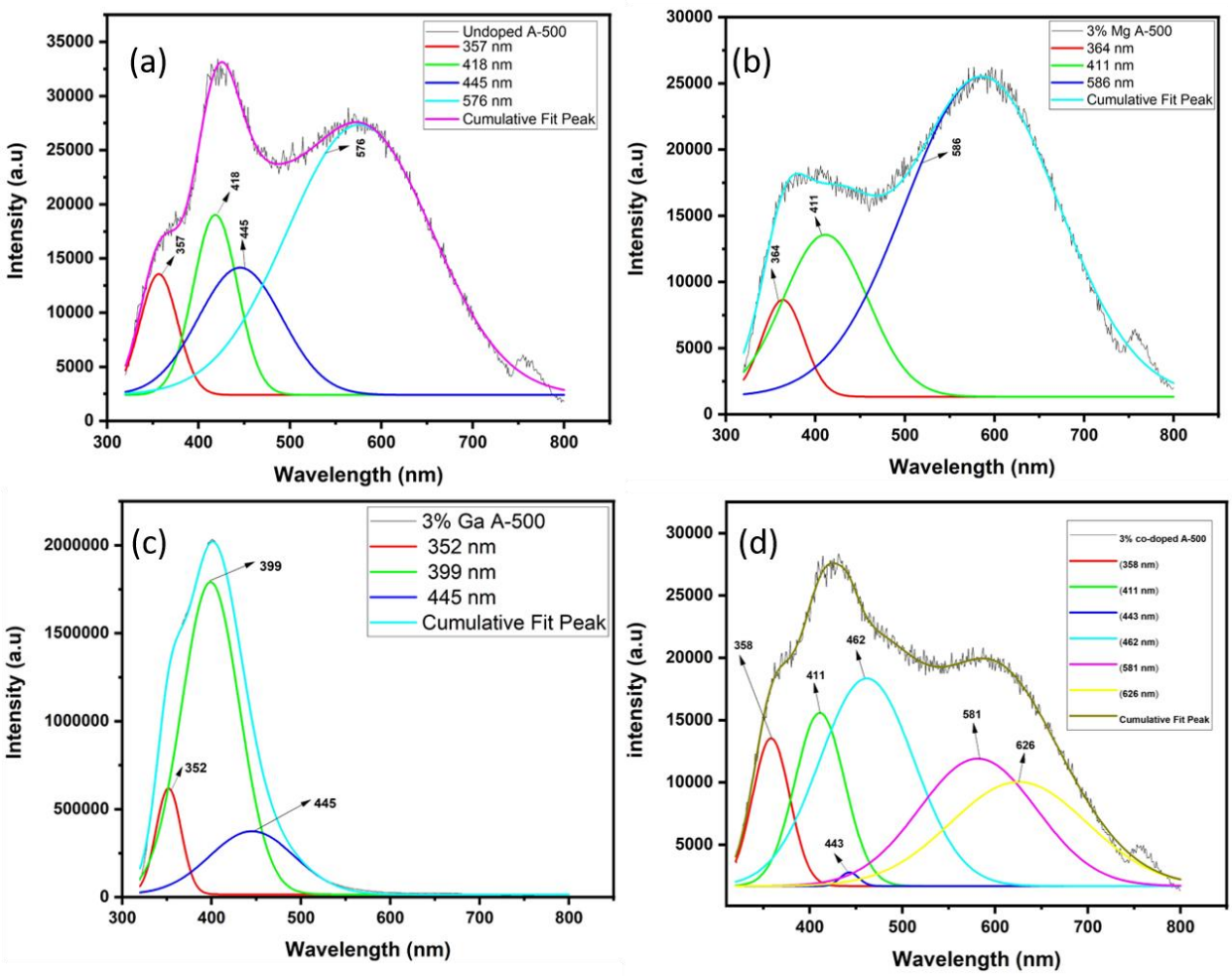

Figure 4.15. Deconvoluted PL spectra of a) Undoped, b) Mg doped, c) Ga doped and d) co-doped ZnO.

(a) Shows the PL spectra of undoped ZnO annealed at 500°C. From the curve fitting we identified peaks at 357 [15], 418 [16], 445 [17], 576 nm [18] ascribed them to inter-band transitions, electron transition from conduction band to top most level of the oxygen interstitial (O_i), zinc vacancy at ~0.21 eV above valence band and $Zn_i \rightarrow O_i$, respectively, owing to the formation energies of the defects. (b) Presents the emission spectra of 3 mol% % Mg doped ZnO. The observed emissions are at 364 [19], 411 [20] and 586 nm which are attributed to band to band transitions, conduction band to zinc vacancy (V_{Zn}) and conduction band to oxygen vacancy (V_O) transitions, respectively.

(c) Presents the PL spectra of 3 mol % Ga doped ZnO. A prominent near band edge (NBE) is seen with emission peaks at 352, 399 and 445 nm ascribed to band to band, NBE and conduction band to V_{Zn} transitions, respectively. Lastly (d) depicts the PL spectra of 3 mol % Mg-Ga co-doped ZnO. In the spectra, we observed emission peaks at 358, 411 [20], 443 [19], 462, 581 and 626 nm ascribed to band to band transitions, two valence band to zinc vacancy transitions, valence band to oxygen interstitial, conduction band to oxygen vacancy and an oxygen vacancy to zinc vacancy transition respectively [19]. These transitions are shown in figure 4.16 (a - d). All doped samples show an increased emission in the visible region which corresponds to down conversion when using a UV excitation source. This means that the inclusion of these dopants can further enhance the properties of ZnO in other applications such as down converting LEDs.

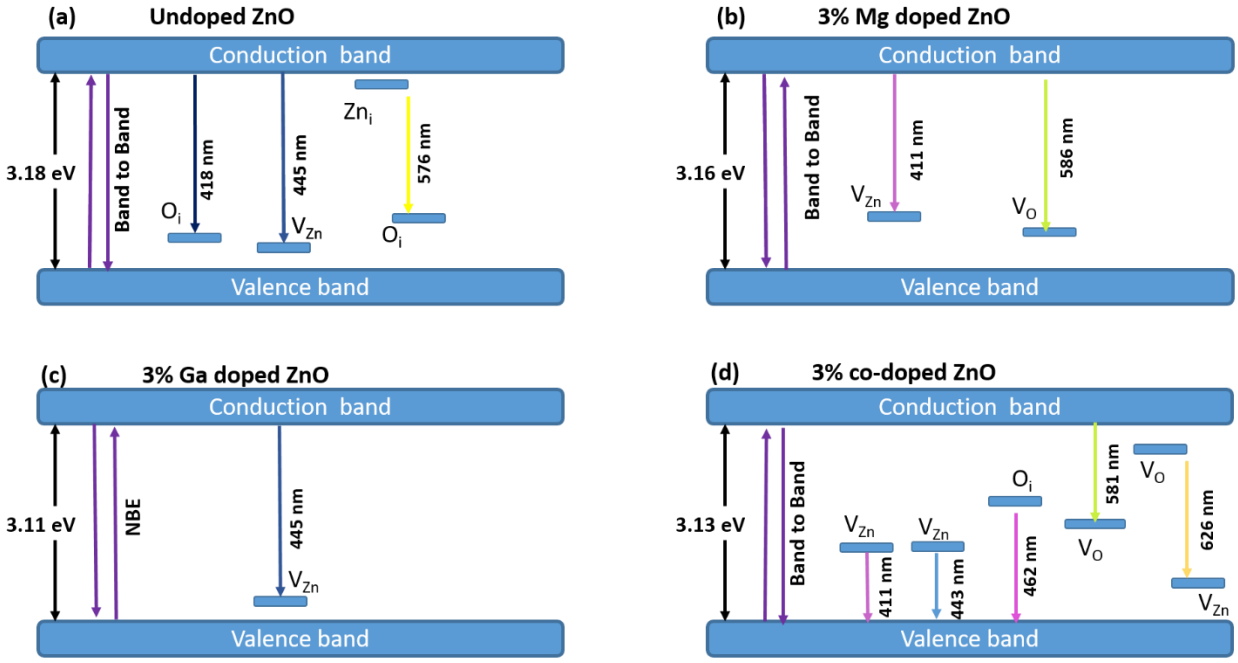

Figure 4.16. Energy diagram showing defect related transitions from ZnO samples in fig. 4.15.

4.6.1. Photoluminescence Life-time measurements

In order to determine the exciton lifetime of co-doped ZnO, time-resolved spectra was carried out at 413, 432 and 587 nm at room temperature. Time-correlated single photon counting is used to determine the single exciton lifetime and subsequently, the efficiency of the radiative

recombination. Fluorescence decay spectra of 3 mol % Mg-Ga co-doped ZnO have been carried out at 413, 432 and 587 nm excitation wavelengths and at room temperature to determine the exciton lifetime of co-doped ZnO. The results are presented in figure 4.17. A single exponential function was used to fit the fluorescence decay profiles based on the χ^2 values yielding the lifetimes given in the Table inset. These transitions closely match the zinc vacancy defect transitions and an oxygen vacancy defect transition. This method has its basis on the probability of detecting a single photon at a certain time after an excitation pulse is proportional to the fluorescence intensity at that particular time.

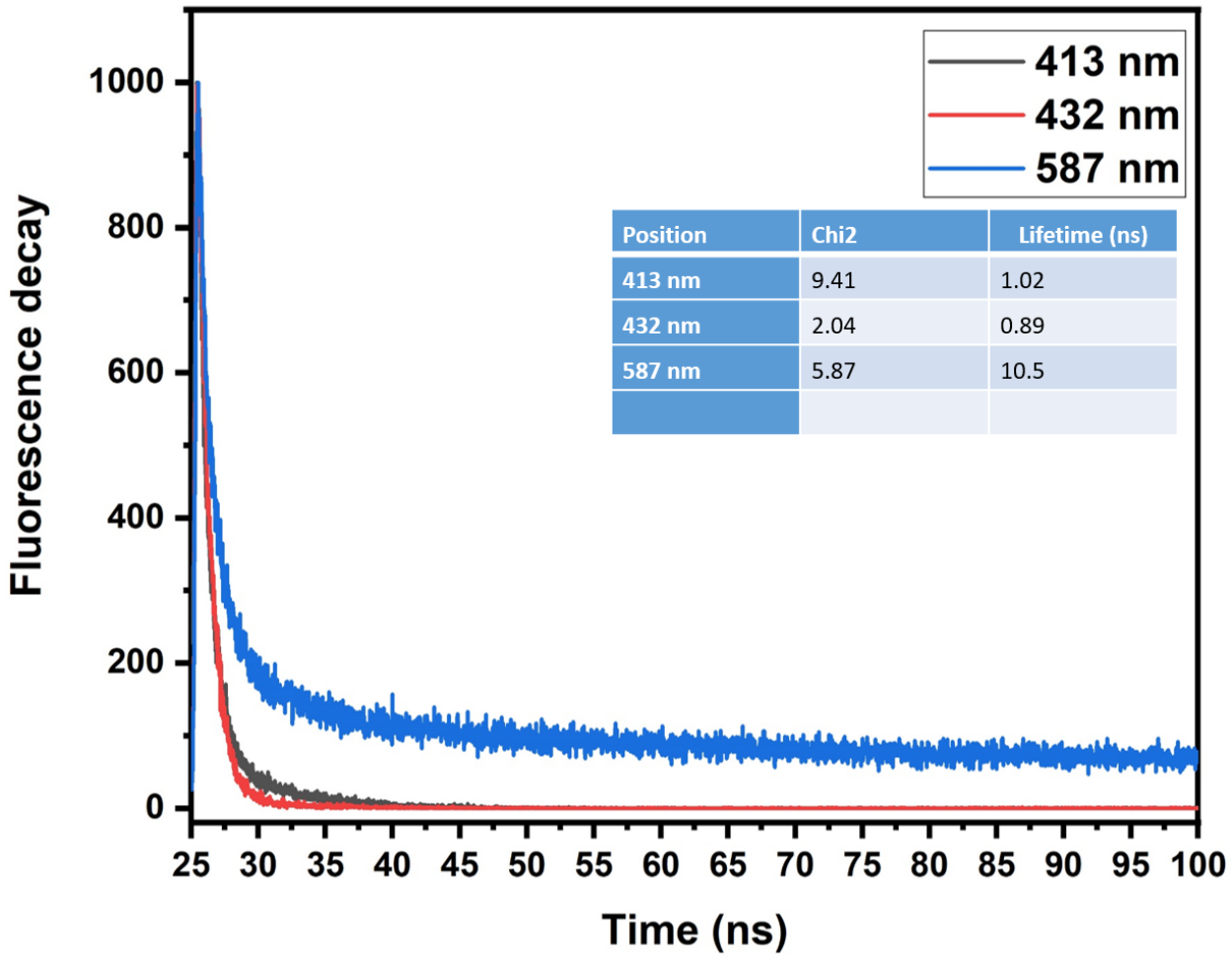

Position	Chi2	Lifetime (ns)
413 nm	9.41	1.02
432 nm	2.04	0.89
587 nm	5.87	10.5

Figure 4.17. Fluorescence decay measurements for 3% co-doped ZnO

The broad band emission has longer lifetimes which is desirable for applications in solar cells as the more time is available to extract carriers. This higher lifetime is attributed to non-radiative recombination processes [21].

Conclusion

Morphological, structural and optical properties of ZnO were investigated. From EDS and SEM we confirmed the elemental composition and their weight percentages and the surface morphology of the nanostructures. The nanostructures were agglomerated together to form rod-like structures. XRD confirmed the hexagonal wurtzite structure of ZnO with increased crystallinity when annealed to 500°C as well as the increase in crystallite size. The results by Raman spectroscopy are in agreement with the XRD data and they confirm the wurtzite phase of ZnO. Raman modes were identified and assigned and the peak shifts were attributed to incorporation of dopants. The band gap of the synthesized samples ranged from 3.11 – 3.18 eV showing no prominent effects of quantum confinement. In the Photoluminescence studies we deconvoluted the spectra and assigned the peaks to defects in ZnO. The light emission mechanisms were discussed.

References

[1] H. Morkoç and Ü. Özgür, *Zinc oxide: fundamentals, materials and device technology*. 2008.

[2] G. Cantwell, W. C. Harsch, and B. Jogai, "Valence-band ordering in zno," *Phys. Rev. B - Condens. Matter Mater. Phys.*, vol. 60, no. 4, pp. 2340–2344, 1999, doi: 10.1103/PhysRevB.60.2340.

[3] K. Nomura, H. Ohta, K. Ueda, T. Kamiya, … M. H.-, and undefined 2003, "Thin-film transistor fabricated in single-crystalline transparent oxide semiconductor." Accessed: Feb. 10, 2021. [Online]. Available: www.sciencemag.org/cgi/content/full/300/5623/1265/.

[4] R. C. Wang, C. P. Liu, J. L. Huang, S. J. Chen, Y. K. Tseng, and S. C. Kung, "ZnO nanopencils: Efficient field emitters," *Appl. Phys. Lett.*, vol. 87, no. 1, Jul. 2005, doi: 10.1063/1.1977187.

[5] S. J. Priscilla, R. Daniel, Y. Dhakshayani, S. C. Caroline, and K. Sivaji, "Effect of magnesium dopant on the structural, morphological and electrical properties of ZnO nanoparticles by sol–gel method," *Mater. Today Proc.*, no. xxxx, pp. 5–8, 2020, doi: 10.1016/j.matpr.2020.07.005.

[6] R. Zhang, P. Yin, N. Wang, and L. Guo, "Photoluminescence and Raman scattering of ZnO nanorods," *Solid State Sci.*, vol. 11, no. 4, pp. 865–869, 2009, doi: 10.1016/j.solidstatesciences.2008.10.016.

[7] Ü. Özgür *et al.*, "A comprehensive review of ZnO materials and devices," *J. Appl. Phys.*, vol. 98, no. 4, pp. 1–103, 2005, doi: 10.1063/1.1992666.

[8] V. M. Vimuna *et al.*, “Study on the structural, morphological and optical properties of RF sputtered gallium doped zinc oxide thin films,” *Mater. Today Proc.*, vol. 4, no. 2, pp. 4417–4433, 2017, doi: 10.1016/j.matpr.2017.04.014.

[9] R. N. Aljawfi, M. J. Alam, F. Rahman, S. Ahmad, A. Shahee, and S. Kumar, “Impact of annealing on the structural and optical properties of ZnO nanoparticles and tracing the formation of clusters via DFT calculation,” *Arab. J. Chem.*, vol. 13, no. 1, pp. 2207–2218, 2020, doi: 10.1016/j.arabjc.2018.04.006.

[10] C. Bundesmann *et al.*, “Raman scattering in ZnO thin films doped with Fe, Sb, Al, Ga, and Li,” *Appl. Phys. Lett.*, vol. 83, no. 10, pp. 1974–1976, 2003, doi: 10.1063/1.1609251.

[11] Y. Song, S. Zhang, C. Zhang, Y. Yang, and K. Lv, “Raman spectra and microstructure of zinc oxide irradiated with swift heavy ion,” *Crystals*, vol. 9, no. 8, 2019, doi: 10.3390/cryst9080395.

[12] A. Escobedo-Morales and U. Pal, “Effect of In, Sb and Ga doping on the structure and vibrational modes of hydrothermally grown ZnO nanostructures,” *Curr. Appl. Phys.*, vol. 11, no. 3, pp. 525–531, 2011, doi: 10.1016/j.cap.2010.09.007.

[13] M. Kahouli, A. Barhoumi, A. Bouzid, A. Al-Hajry, and S. Guermazi, “Structural and optical properties of ZnO nanoparticles prepared by direct precipitation method,” *Superlattices Microstruct.*, vol. 85, pp. 7–23, 2015, doi: 10.1016/j.spmi.2015.05.007.

[14] I. M. Alibe, K. A. Matori, E. Saion, and M. Alibe, “The Influence of Calcination Temperature on Structural and Optical Properties of ZnO Nanoparticles via Simple Polymer Synthesis Route The Influence of Calcination Temperature on Structural and Optical Properties of ZnO Nanoparticles via Simple Polymer Syn,” no. September, 2017,

doi: 10.2298/SOS1703263A.

[15] J. Kaur, P. Kumar, T. S. Sathiaraj, and R. Thangaraj, “Structural , optical and fluorescence properties of wet chemically synthesized ZnO : Pd 2 + nanocrystals,” pp. 3–9, 2013.

[16] Y. Zhao, S. Li, Y. Zeng, and Y. Jiang, “Synthesis and properties of Ag / ZnO core / shell nanostructures prepared by excimer laser ablation in liquid Synthesis and properties of Ag / ZnO core / shell nanostructures prepared by excimer laser ablation in liquid,” vol. 086103, pp. 1–8, 2015.

[17] S. K. Mishra, R. K. Srivastava, S. G. Prakash, R. S. Yadav, and A. C. Panday, “Photoluminescence and photoconductive characteristics of hydrothermally synthesized ZnO nanoparticles,” vol. 18, no. 4, pp. 467–473, 2010, doi: 10.2478/s11772.

[18] S. Vempati, J. Mitra, and P. Dawson, “One-step synthesis of ZnO nanosheets : a blue-white fluorophore,” pp. 1–10, 2012.

[19] N. Shakti, C. Devi, A. K. Patra, P. S. Gupta, and S. Kumar, “Lithium nanorods doping and photoluminescence properties of ZnO,” doi: 10.1063/1.5008863.

[20] M. Science, “Optical and Magnetic Properties of ZnO-based Semiconductors Regulated by Cu Ions,” vol. 51, no. 1, pp. 143–150, 2013, doi: 10.6122/CJP.51.143.

[21] P. Mondal, “Effect of Oxygen vacancy induced defect on the optical emission and excitonic lifetime of intrinsic ZnO,” *Opt. Mater. (Amst).*, vol. 98, no. August, p. 109476, 2019, doi: 10.1016/j.optmat.2019.109476.

[22] N. Against, E. H, M. Saliani, and R. Jalal, “Effects of pH and Temperature on Antibacterial Activity of Zinc Oxide Effects of pH and Temperature on Antibacterial

Activity of Zinc Oxide Nanofluid Against Escherichia coli O157 : H7 and Staphylococcus aureus," no. February, 2015, doi: 10.5812/jjm.17115.

Chapter 5 – Magnetic Properties of pristine ZnO and co-doped ZnO

5.1. Introduction

Wide bandgap semiconductors such as ZnO have a large range of applications in optoelectronics. Changes in electrical, optical as well as magnetic properties can be achieved by introducing impurities through doping processes. Enhancing the magnetic properties of ZnO nanoparticles promises a crucial role in improving device performance through increased exciton dissociation and reduction of recombination channels through triplet energy states that are aided by the induced magnetic field. Studies have shown the role of spin, energetic and delocalization of electronic transitions could be used to suppress recombination losses in organic semiconductors [1-3]. Additionally, time resolved spectroscopy studies have shown that the molecular triplet exciton energy state is much lower than the intermolecular charge transfer states of high efficiency polymer –fullerene systems. Hence these studies provide opportunities to increase the understanding on the interlink of the relative positions of the intermediate energy levels with the global recombination rates using magnetic excitation [4]. The effect of the magnetic field on the intersystem crossing and or the formation of the triplet exciton state on the photocurrent can be studied directly in a magnetic field environment or indirectly using ferromagnetic transparent conducting electrodes.

Studies on room temperature ferromagnetic behavior of ZnO have attracted extensive interest driven primarily by its high potential for spintronic applications and magnetic sensors [5-8]. Bulk ZnO have shown ferromagnetic effects and they have been associated with vacancies or grain boundaries. Similar effects were found in ZnO thin films and nanoparticles after doping with transition metal elements following theoretical predictions of high curie temperature in these material configuration [6-7]. Therefore. room ferromagnetism in ZnO remains a topic of great research interest owing to the long spin coherence time, higher dopant solubility and free carrier concentrations which makes ZnO a promising candidate material as a dilute magnetic semiconductors.

After various theoretical efforts and experiments, the exact mechanisms causing these behaviors are still subject to much debate. Numerous studies have also attributed the ferromagnetic properties in ZnO to either grain boundaries, clustering of ferromagnetic dopants, threshold electron/hole

concentrations and intrinsic defects [9]. Another report ascribed ferromagnetism in the materials to exchange interactions between localized spin moments resulting from oxygen vacancies in the surface of nanoparticles [2]. Thus, implying that surface magnetism could play a significant role in ZnO nanostructured materials. As ZnO is used as electrode transport layer, its magnetic properties could affect the photocurrent generated in organic photovoltaic devices. Hence combining this effect with the probable evidence of triplet states in organic semiconductors, gives the driving force for the renewed interest particularly in the consideration of triplet charge states as recombination pathways during exciton dissociation. This idea is further anchored on the prevalence of low energy triplet exciton states which confirm bimolecular recombination and thus curtail the enhancement of photo conversion efficiency in organic photovoltaic devices. The present study explores the effect of doping ZnO with a group II and III element on the opto-electrical and structural properties. Since doping changes the fermi energy levels and subsequently introduces additional charge carriers, we thus study the magnetic properties of ZnO doped with Ga and Mg using temperature dependence magnetization and isothermal magnetization field curves at room temperature and after annealing at 500 °C.

5.2. Pristine co-doped ZnO (un-annealed)

The incorporation of ZnO either as an electron transport layer or as an electron acceptor in the hybrid solar cell is used as a strategy to increase the performance and lifetime of organic solar cell devices. Hence it is essential that their magnetic properties are investigated to determine whether the presence of triplet exciton charge state of lower energy could be eligible for recombination losses [10]. Therefore, we have investigated the magnetic properties of ZnO upon co-doping with Mg and Ga at various sample conditions. The ferromagnetism in ZnO at room temperature remains a topic of great interest for a wide variety of applications. The magnetic behavior of the co-doped ZnO nanostructures is investigated from the field cooling curves which represent the temperature dependence of magnetization in low and high magnetic fields 0.5 T and 2 T. These measurements are intended to show magnetic transition at critical temperatures (Figures 5.1 a) and b).

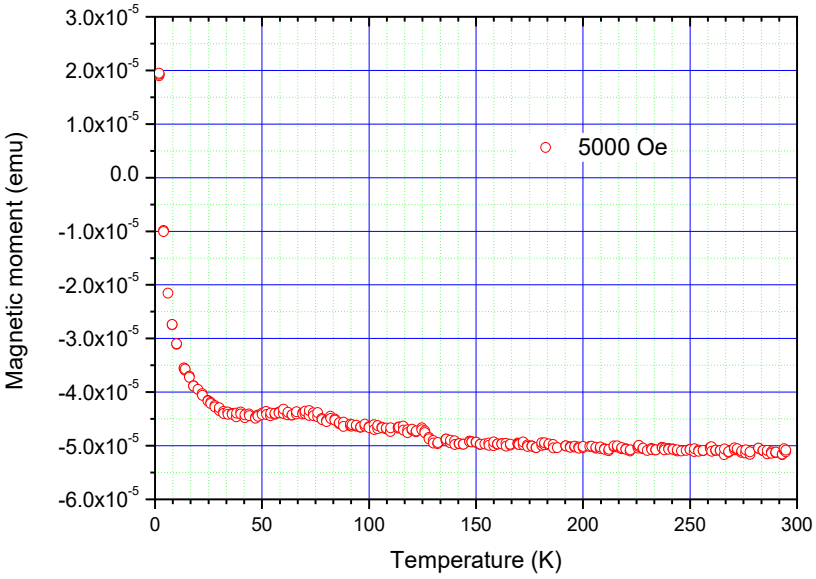

(a)

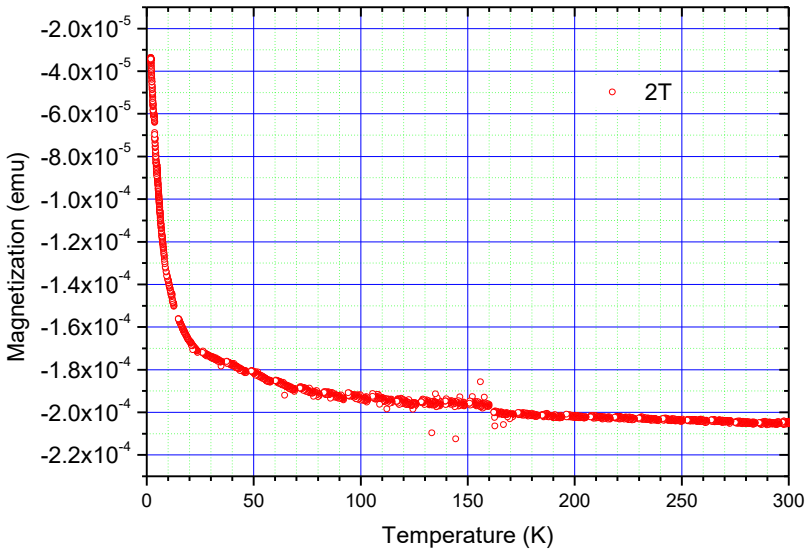

(b)

Figure 5.1 a) showing the magnetization dependence with temperature at 0.5T and b) 2T. It is evident that at room temperature pristine co-doped ZnO exhibit diamagnetic behavior.

It is evident that there is a diamagnetic to superparamagnetic transition at 3K. This is also supported by the d^2M/dT^2 which confirms a transition at 3K for lower magnetic fields. Additionally, the isothermal magnetization versus the applied field curves were used to verify this transition. These curves have been measured for room temperature (300 K) and 2 K as shown in Figure 5.2 a) and b), respectively for the pristine (un-annealed) co-doped ZnO nano-powders. It is evident that the un-annealed co-doped ZnO exhibits weak diamagnetic behavior at 300K while a weak ferromagnetic behavior coupled with diamagnetic or antiferromagnetic correlations coexist at 2 K. The source magnetization at low temperatures could be attributed to the presence of defects that might introduce exchange interactions with delocalized free electrons due to oxygen vacancies or zinc interstitials [12]. This associates defects with magnetism which increase with co-doping as shown by Photoluminescence results. Additionally, the role of dangling bonds of surface oxygen coupled with 2 Zn cations and dopants could also contribute to surface state driven magnetism [11].

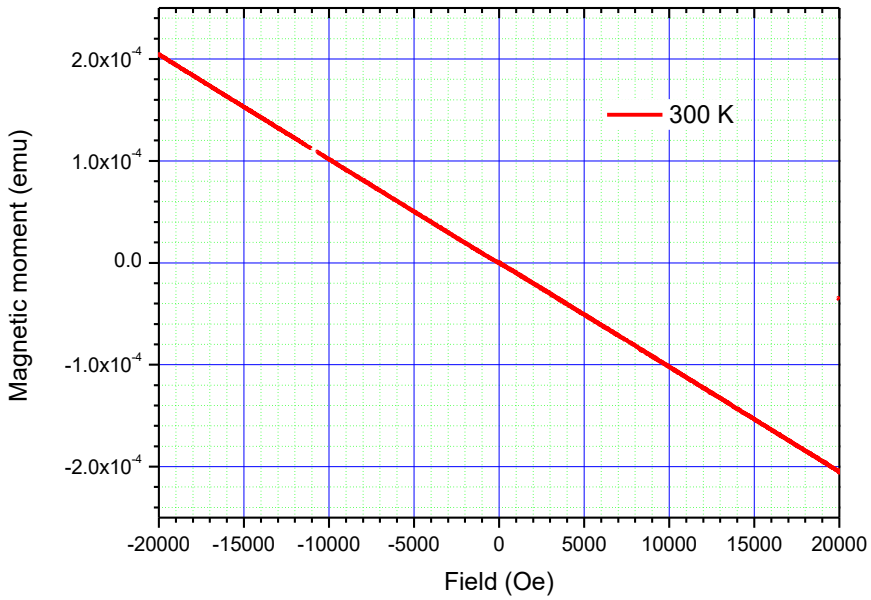

Figure 5.2 a) Magnetization versus field dependence for pristine co-doped ZnO at 300 K. It is evident that the ZnO nanoparticles exhibit diamagnetic behavior even at higher applied fields.

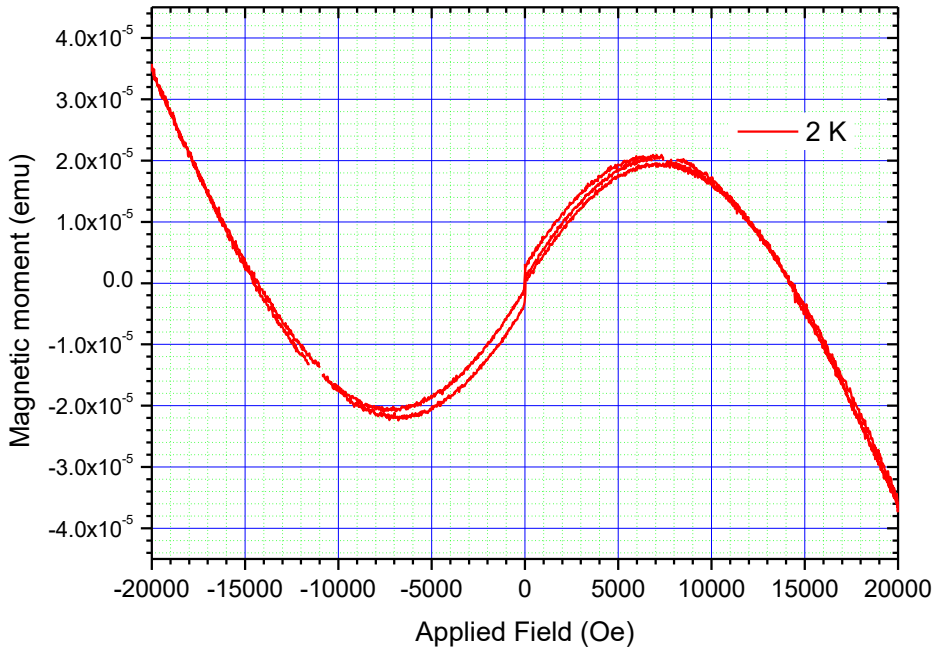

Figure 5.2 b) Isothermal magnetization versus field dependence curves for pristine co-doped ZnO at 2 K showing a mixed magnetic signatures of ferromagnetism with diamagnetic phases. The applied fields have been ramped between ±2 T.

5.3. Magnetic properties of annealed co-doped ZnO.

The annealing of co-doped ZnO nanoparticles have not shown any significant changes in the grain size (section 4.8). Thus any changes in magnetization cannot be attributed to grain boundaries related effects as seen in Figure 5.3 a) and b).

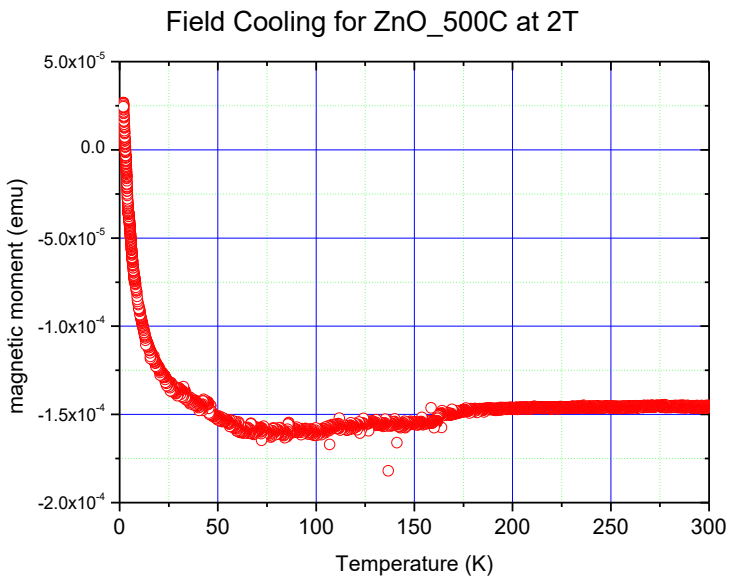

Figure 5.3 Magnetization dependence on the temperature for co-doped ZnO upon cooling at 2T.

Figure 5.3 shows the temperature dependence of the induced magnetization in the presence of an applied field (20000 Oe). It is evident that upon annealing at higher temperature co-doped ZnO behaves like a diamagnetic material up to very low temperatures for which the incidence of super paramagnetism becomes apparent and fits to the Brillouin function at H < 1 T. This is seen when the experiment is repeated at a higher field 2T in which transition temperature is further shifted to higher values (2.5 $x10^{-4}$ emu) in the vicinity of 4 K.

Figure 5.4 a) and b) show the isothermal magnetization measurements of annealed co-doped ZnO nano-powders. The measurements have been carried out at 2K by sweeping the field between ±2T. It is evident that there are competing interactions of super-paramagnetism and diamagnetism at higher fields. At room temperature ZnO is diamagnetic as seen from the magnetic moment dependence with applied field the magnetic susceptibility is negative and can be estimated to have a magnetic permeability slightly less than 1.

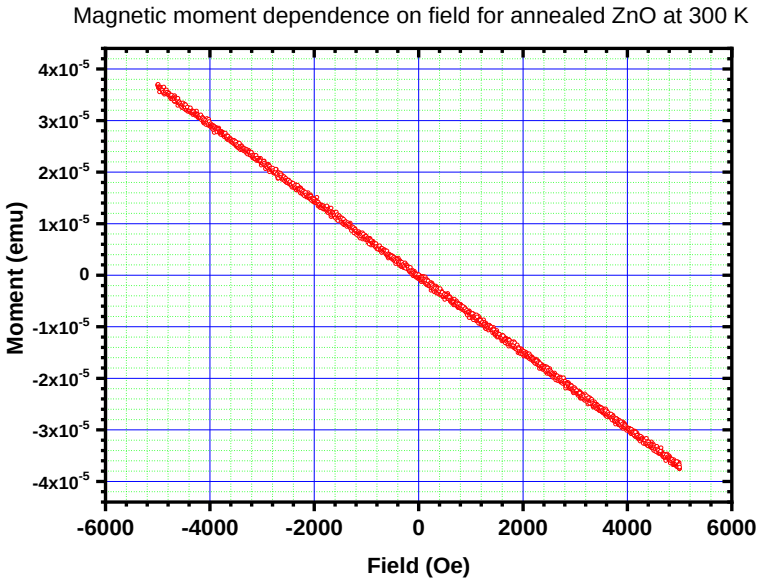

(a)

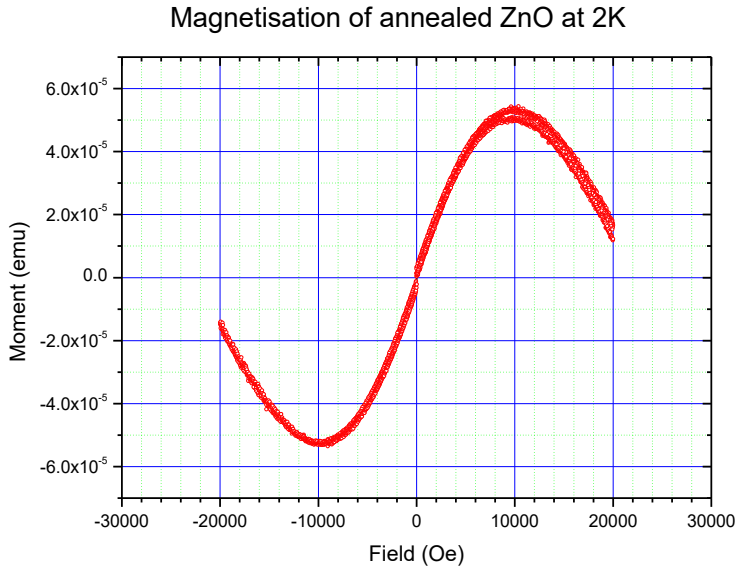

(b)

Fig. 5.4 a) and b) Isothermal magnetization curves of co-doped ZnO annealed at 500C. At 2 K it is evident that the hysteresis depicts paramagnetic behavior owing to the lack of the coercive field.

At higher values of applied field the behavior does not change there is no incidence of alternate magnetic center at 300K and higher field. The transition to super-paramagnetism is seen at lower T possibly in the M(T) curves below at 2-3 K. It is also probable that at H > 1 T leads to the randomization of the magnetic moments due to the lack of exchange correlation.

Conclusion

At room temperature ZnO is diamagnetic as seen from the magnetic moment dependence on the applied field where the magnetic susceptibility is negative and can be estimated to have a magnetic permeability slightly less than 1. Temperature dependence of the induced moment in the presence of a magnetic field (20000 Oe) was evaluated. It was evident that upon annealing at higher temperature co-doped ZnO behaves like a diamagnetic material up to very low temperatures for which the incidence of super paramagnetism becomes apparent. This is observed when the experiment was repeated at a higher field 2T in which transition temperature shifted to higher values (4K)

References

[1] M.A. Garcia, J.M. Merino, E. Fernandez Pinel, A. Quesada, J. de la Venta, M.L.Ruiz Gonzalez, G.R. Castro, P. Crespo, J. Llopis, J.M. Gonzalez-Calbet and A. Hernando, Magnetic Properties of ZnO nanoparticles, Nanoletters, pp 1489-1494, 2007.

[2] R. Akshay, P. C. Chow, S. Gelinas, C.W. Schlenkerm C-Z. Li., H-L Yip, A. K-Y. Jen, D. S. Ginger and R. H. Friend, The role of spin in the kinetic control of recombination in organic photovoltaics, Nature, 500, pp 435 - 439 (2013).

[3] Z. L. Lu, H. S. Hsu, Y. H. Tzeng, F. M. Zhang, Y. W. Du, and J. C. A. Huang, The origins of ferromagnetism in Co-doped ZnO single crystalline films: From bound magnetic polaron to free carrier-mediated exchange interaction, Appl. Phys. Lett. **95**, 102501 (2009)

[4] S. Oviedo-Casado, A. Urbina and J. Prior, Magnetic fields: A tool for the study of organic solar cells, The European Physical Journal Special Topics, 227, pp 259- 268 (2018)

[5] T. Dietl, Origin of ferromagnetism in Dilute Magnetic semiconductors and oxides, J. Appl. Phys. 103, 07D111 (2008).

[6] K. Ueda, H. Tabata and T. Kawai, Magnetic and electric properties of transition metal doped ZnO films, Appl. Phys. Lett. 79, pp. 988 -990 (2001).

[7] V. Gandhi, R. Ganesan, H. H. A. Syedahamed and M. Thaiyan, Effect of Co- doping on

structural, optical and magnetic properties of ZnO nanoparticle synthesized by Co-precipitation Method, J. Phys. Chem. C. 2014, 118,18,18 pp 9715-9725

[8] H. Polymer and S. Cells, “Effects of Magnetic Nanoparticles and External Magnetostatic Field on the Bulk,” pp. 1–9, 2015, doi: 10.1038/srep09265.

[9] A. Sundaresan, R. Bhargavi, N. Rangarajan, U. Siddesh, and C. N. R. Rao, “Ferromagnetism as a universal feature of nanoparticles of the otherwise nonmagnetic oxides,” pp. 1–4, 2006, doi: 10.1103/PhysRevB.74.161306.

[10] S. Oviedo-Casado, A. Urbina and J. Prior, magnetic field enhancement of organic photovoltaic cells performance, Scientific reports 7, 4297,pp1-9 (2017).

[11] J. A. Phys, “Surface defects induced ferromagnetism in mechanically milled nanocrystalline ZnO,” vol. 073516, no. April, 2013, doi: 10.1063/1.4818802.

[12] Q. Xu, H. Schmidt, S. Zhou, K. Potzger, M. Helm, H. Hochmuth, M. Lorenz, A. Setzer, P. Esquinazi, C. Meinecke and M. Grundmann, Room Temperature ferromagnetism in ZnO films due to defects, 92, 082508 (2008).

Chapter 6 – Effect of Mg-Ga Co-doped ZnO nanoparticles on the Photovoltaic Properties of P3HT:PCBM Based Organic Solar Cells

6.1. Introduction

Organic photovoltaic (OPV) cells usually show poor device stability due to two reasons: (i) metal atoms diffusion from the top cathode electrode to the photoactive layer and (ii) use of low work function and air-sensitive metals such as Al and Ca as the top cathode. As a result, metal oxides nanoparticles such as ZnO have been inserted as a buffer layer between the top electrode and the photoactive layer to block, simultaneously, the diffusion of atomic species from the top electrode to the photoactive layer and holes from reaching the top electrode, and they also act as electron transport layer due to their relatively high electron mobility. In addition, the ZnO nanoparticles can also be blended with the photoactive layer to suppress charge recombination and enhance charge collection at the top electrode-photoactive layer interface. Ferreira et al. reported improved efficiency of a hybrid zinc oxide nanoparticle:poly(3-hexylthiophene) blended solar cells attributed to improved interfacial morphology in the vicinity of the donor and acceptor molecules [1]. A similar approach was adopted in this study, with Mg-Ga co-doped ZnO nanoparticles blended with P3HT:PCBM molecules and their effect on the photovoltaic properties of the OPV devices were investigated. In this respect, ZnO was used to replace the electron acceptor in the bulk heterojunction at mass ratios of 3 to 7 mg with the active layer component PCBM. Important to the function of the OPV device is the morphology of the interconnected network. Particle morphology determines the efficiency of the exciton diffusion and dissociation and thus the photocurrent after charge transport. Therefore, the co-doped ZnO nanoparticles have not exhibited diamagnetic behavior at 300 K and the effects of the magnetic field on the photocurrent was not investigated.

6.2. Experimental

6.2.1. Device Fabrication

The procedure for fabricating organic photovoltaic devices on patterned ITO substrates (30 - 60 Ω-square) is outlined as follows: etched indium tin oxide (ITO) coated glass substrates were first

cleaned by sonication using acetone and ethanol in that order to remove any organic contaminants on the surface. This was followed by repeated rinsing of the ITO coated glass slides with distilled H_2O. The hole transport layer (PEDOT:PSS) was subsequently spin coated on the ITO at 2000 rpm for 1 minute and annealed over a hot plate at 100 ^oC for 2 minutes to remove any residual water. This was followed by spin coating of a layer of P3HT:PCBM blend mixture at 2000 rpm for 1 minute. The blend composition ratio was fixed by mass at 1.1 in a concentration of 20 mg/ml. The synthesized nanoparticles were added to the PCBM at mass ratio of 3 to 7 mg. Finally, an aluminum top electrode (100 nm) was thermally evaporated at a pressure of 2×10^{-5} Pa. The devices were then annealed at 100 ^oC for 15 minutes under Ar ambient to remove any organic solvents and further promote the intermixing of the donor and acceptor polymers. This device is referred to as the reference device. Similarly, three other devices with blends of ZnO:P3HT:PCBM (ZnO device), Ga/ZnO:P3HT:PCBM (Ga/ZnO device) and Mg-Ga/ZnO:P3HT:PCBM (Mg-Ga/ZnO device) were fabricated. The concentration of ZnO, Ga doped ZnO (Ga/ZnO) and Mg,Ga co-doped ZnO nanoparticles was maintained at 3 mol%. The schematic diagrams of these devices are depicted in Figures 6.1 (a - d).

The devices were characterized by Raman spectroscopy, UV-vis spectroscopy and photo luminescence spectroscopy. To measure the current density-voltage (J-V) characteristics of the devices, a HP 4141B source measure unit (SMU) under 100 mW/cm^2 illumination was used. All measurements were carried out under standard conditions at room temperature.

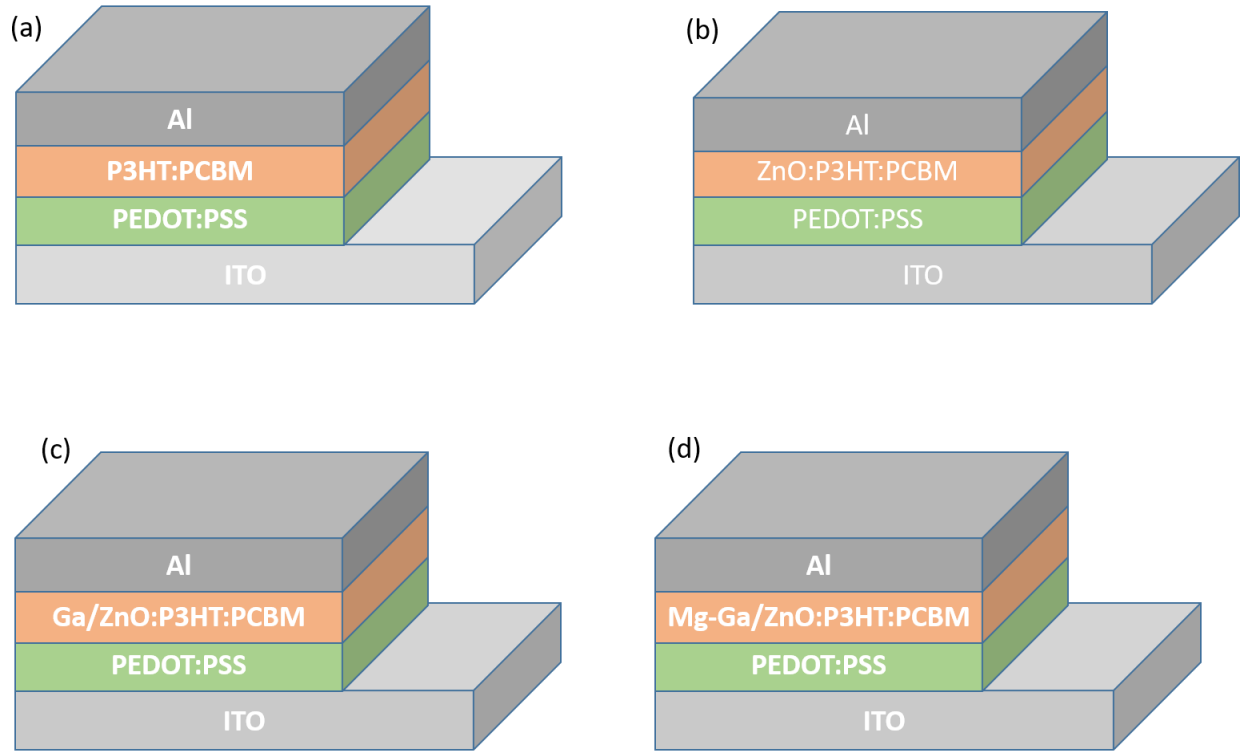

Figure 6. 1. Schematic diagrams of the layered device architecture.

6.3. Raman Spectroscopy

The observed Raman spectra of undoped and Mg-Ga co-doped ZnO nanoparticles incorporated P3HT:PCBM devices shown in figure 6.2 contains all Raman modes similar to those reported by S. Falke et.al. [2]. The most intense peak is located at 1444 cm^{-1} and is attributed to aggregated P3HT $C_\alpha - C_\beta$ stretching of a thiophene ring. The peak at 1377 cm^{-1} is assigned to has C_β - C_β stretching mode and is consistent with result reported by Giulianini et al. [3]. Other less intense peaks observed at 1004, 1080, 1184, 1210 and 1516 cm^{-1} are attributed to $C_\beta - C_{alkyl}$ stretching mode [4], a combination of $C_\beta - H$ [5] and $C_\alpha - C_\alpha$ stretching modes, and the $C_\alpha = C_\beta$ antisymmetric stretch modes, respectively [6]. The peak observed at 727 cm^{-1} is attributed to an antisymmetric $C_\alpha - S - C_\alpha$ in-phase deformation in thiophene ring of the P3HT polymer [7]. The insets are the surface micrographs taken with Raman camera showing the distribution of nanoparticles over device surface. The area measured is from -10 to 10 μm on the x-axis and -10 to 10 μm on the y-axis. Since the P3HT surface layer is smooth (inset (d)), it is reasonable to assign the particles

distributed on the surface of the other three Raman micrographs to ZnO and Ga-Mg co-doped ZnO.

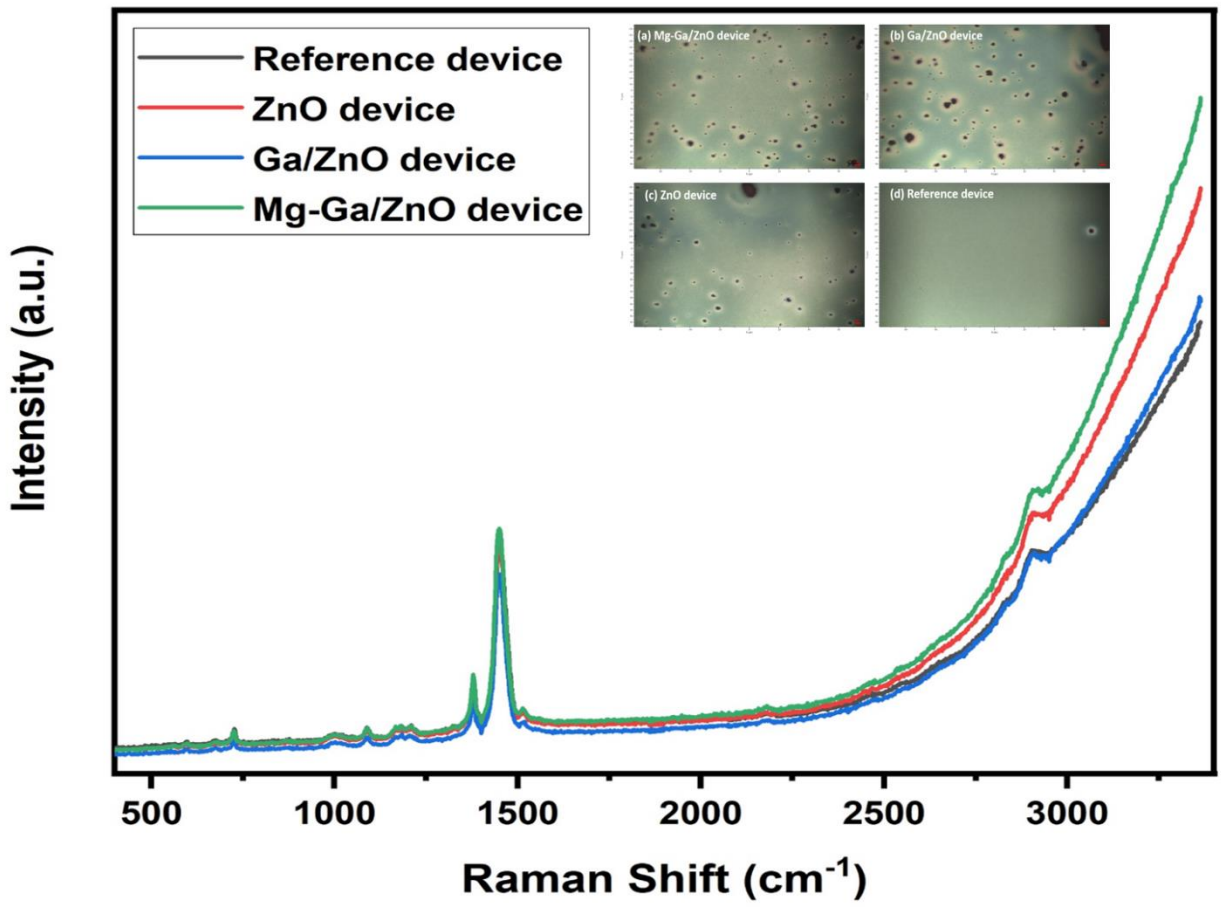

Figure 6.2. Raman spectra of the reference, ZnO, Ga/ZnO and Mg-Ga/ZnO devices. The insets are the Raman micrographs of these devices. The presence of the dark spots is indicative of the lack of solubility of ZnO in the solvent and hence the presence of hillocks and pinholes.

6.4. UV-Vis spectroscopy

Figure 6.3 shows the absorption spectra of the layered OPV devices. The spectra are characterized by a broad absorption peak ranging from 438 – 570nm with a maximum at 513 nm, and a minor peak at 600 nm. An increase in absorption is seen in the Ga/ZnO and Mg-Ga co-doped ZnO devices. This increase in absorption with introduction of dopants in ZnO indicates that defect emissions augment the absorption of P3HT through reabsorption to enable the π-π^* transitions in

P3HT [8]. The Mg-Ga/ZnO device ZnO shows relatively high absorbance. This can be attributed to increased interchain interactions between P3HT chains from more delocalized electrons [9] induced by the presence of Mg^{2+} and Ga^{3+}. The undoped ZnO containing device shows the least absorbance with a maximum absorbance at 515 nm. All film thickness were constant in devices and in accordance with Beer's law and optical density.

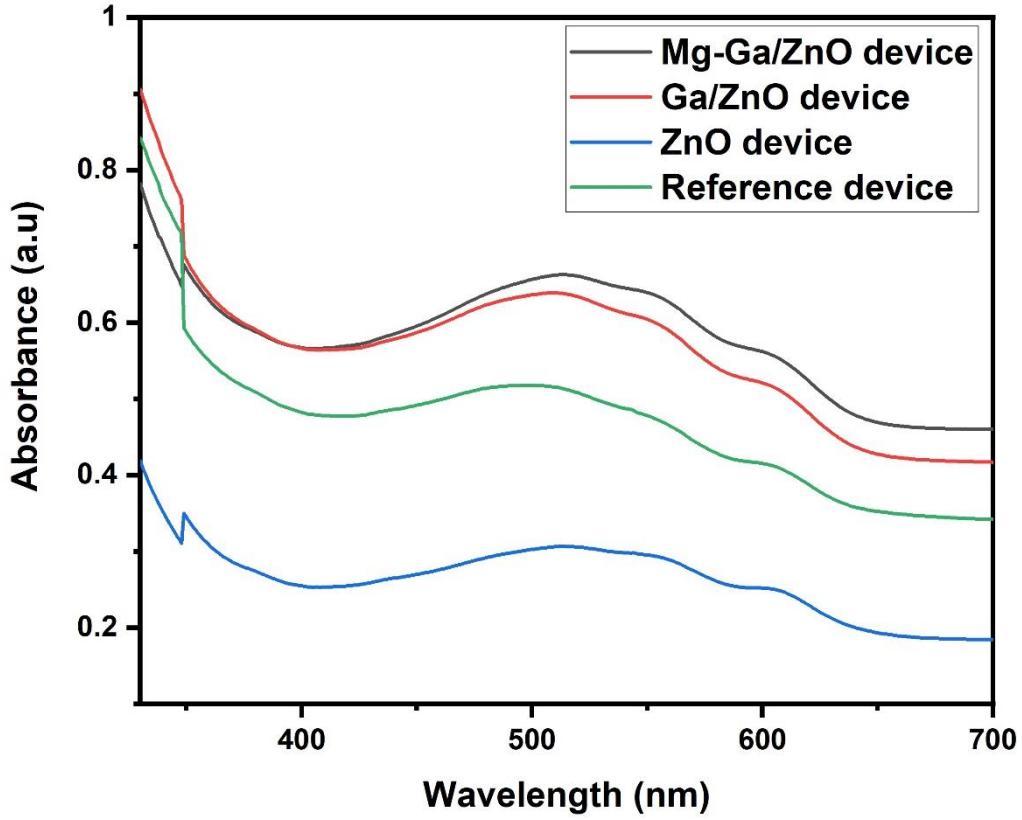

Figure 6.3. Absorbance measurements of fabricated devices. The step at 350 nm is an artifact of measurement due the switch over from Tungsten to deuterium lamp

6.5. Photoluminescence spectroscopy

Figure 6.4 shows the PL emission spectra of the reference, ZnO, Ga:ZnO and Mg-Ga:ZnO devices measured when exciting the samples at the wavelength of 517 nm using a monochromatized xenon lamp thereby exciting the P3HT and the defect emission centres in ZnO. All the spectra consist of two distinct emission peaks at 651 nm and 702 nm and a minor emission peak at 663 nm. Kabongo et al [10] have attributed the major emission peaks at 651 nm and 702 nm, respectively,

to (0-0) and (0-1) transitions of H-aggregates in regio-regular P3HT. The highest PL intensity was recorded from the ZnO and Mg,Ga/ZnO device compared to the reference and Ga/ZnO devices. The increase in the PL intensity suggests that the exciton dissociation was suppressed and that both Mg, Ga/ZnO and ZnO acted as recombination centres leading to increased generation and emission of visible photons. Considerable quenching of the PL emission intensity of the reference and Ga/ZnO devices points to enhanced exciton dissociation and subsequent charge carriers transfer to both the cathode and anode. Similar observation and explanation are reported in [11]. In addition, the PL data is consistent with the PCE values where the lower values were recorded from the samples with higher PL intensities, while the samples with lower PL intensities gave higher values of the PCE (see Table 6.1).

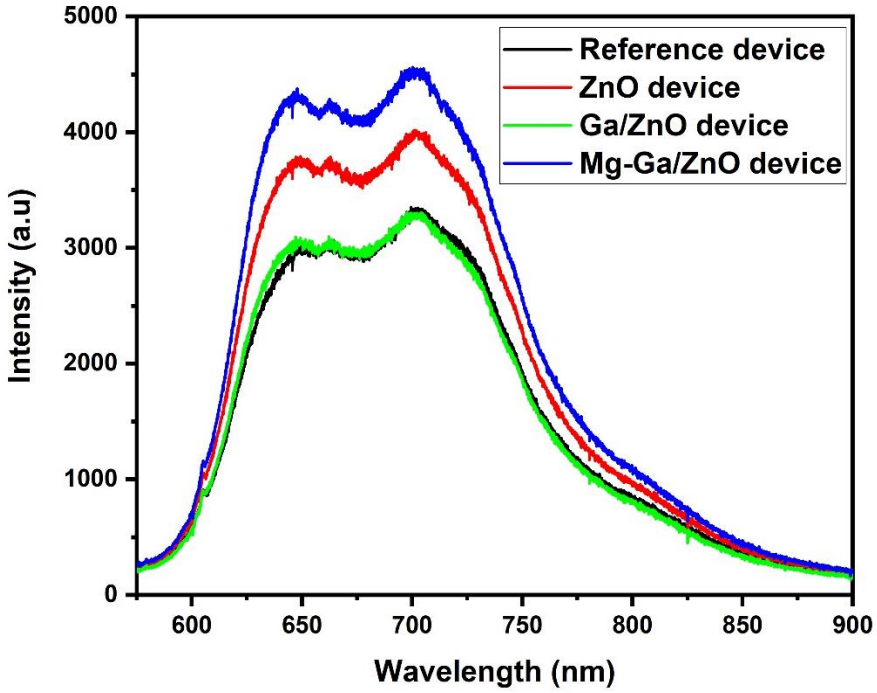

Figure 6.4. ZnO nanoparticle incorporated P3HT:PCBM devices

6.6. Current density – Voltage (J-V) curves

Figure 6.5 – 6.8 show the current-voltage (J-V) curves used as a proof of concept for the application of magnesium and Mg-Ga co-doped ZnO as electron extracting compound in organic

solar cells, of the architectural structure: ITO/PEDOT:PSS/ Mg,Ga/ZnO:P3HT:PCBM/Al. The devices were annealed at 100°C for 15 minutes after fabrication to decrease the correlation length and thus improve the interconnected network within the exciton diffusion length. Annealing improves the diffusion of PCBM into the P3HT. Table 6.1 shows the performance parameters of the solar cells. It can be observed that the reference and ZnO devices have similar values for V_{oc}, which implies that the ZnO did not affect the amount of charge carriers dissociating in the active layer. Similarly, the value of V_{oc}, though much lower, is the same for the Ga/ZnO Mg,Ga/ZnO devices. Depicted in figure 6.9 are the power conversion efficiencies (PCE) of each device. The reference device shows the highest efficiency at 7%, followed respectively by ZnO, Ga/ZnO and Mg,Ga/ZnO devices at 0.13, 0.0062 and 0.0008%. As mentioned earlier (section 6.5), the relatively lower values of the PCE for devices incorporating ZnO and Mg,Ga co-doped ZnO nanoparticles is attributed to poor exciton dissociation in such devices. The introduction of ZnO nanoparticles to the active-layer blend is seen to act in a counter-productive manner in greatly reducing the PCE of the devices [17]. This drop can be attributed to the nanoparticles causing cracks probably due to differing particle sizes and non-homogeneous distribution which form alternative pathways for current to flow in the device, and they can also affect the contact between the active layer and the top aluminum electrode. The latter is justified by the low shunt and high series resistances observed in the J-V curves. The nanoparticles could have also caused defect centers that act as carrier trapping sites, increasing the diffusion lengths making it difficult for excitons to travel. Incorporating the ZnO nanoparticles in the device by spin coating the blend has a limitation by not ensuring homogeneous distribution of nanoparticles over the active-layer and may be a contributing factor as particles may have formed agglomerations and not dispersing evenly over the device area.

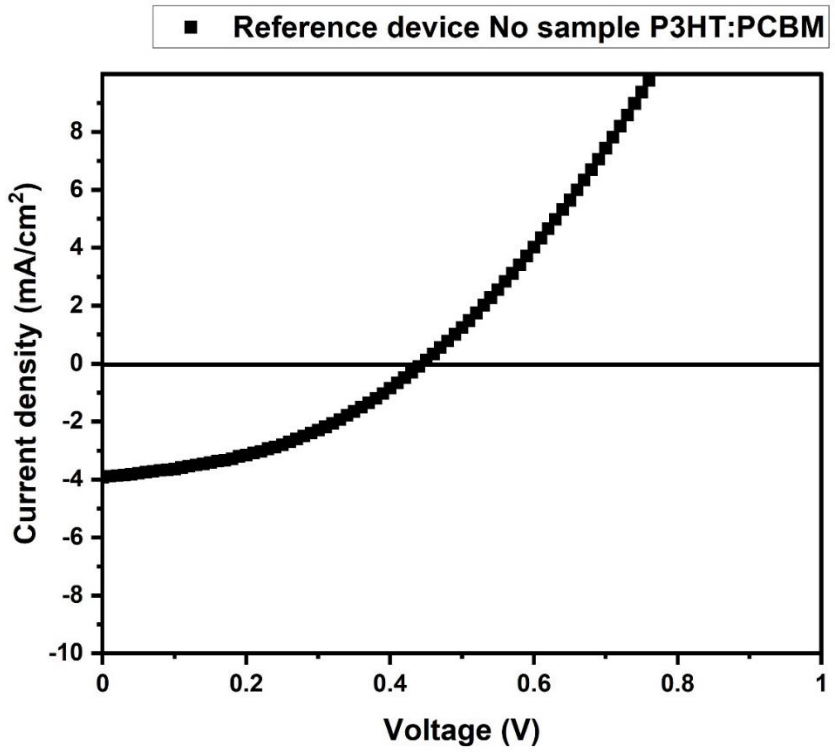

Figure 6.5. J-V curve for the reference device with only the P3HT:PCBM active layer blend.

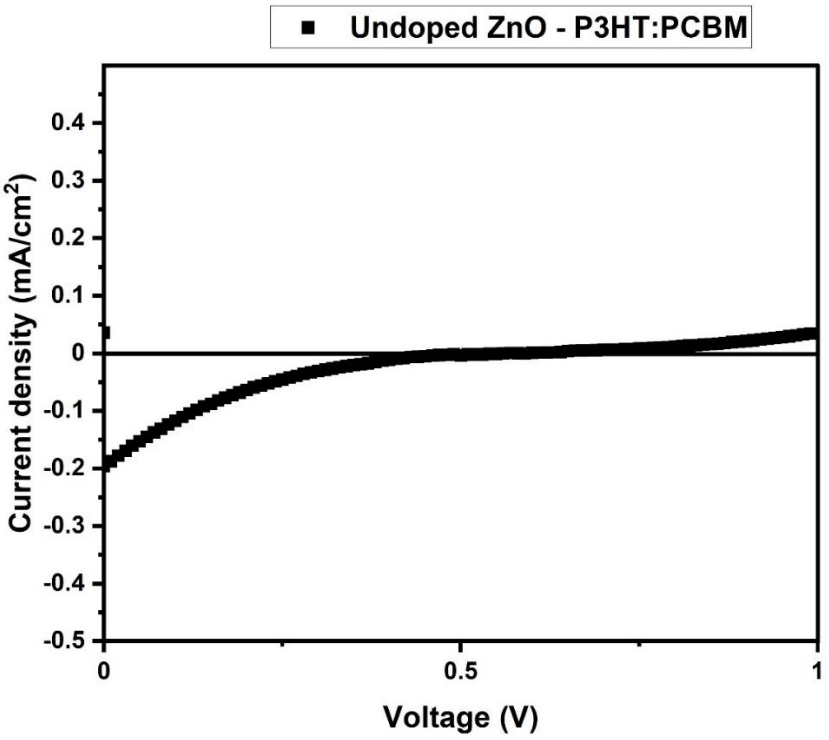

Figure 6.6. J-V curve of ZnO:P3HT:PCBM device

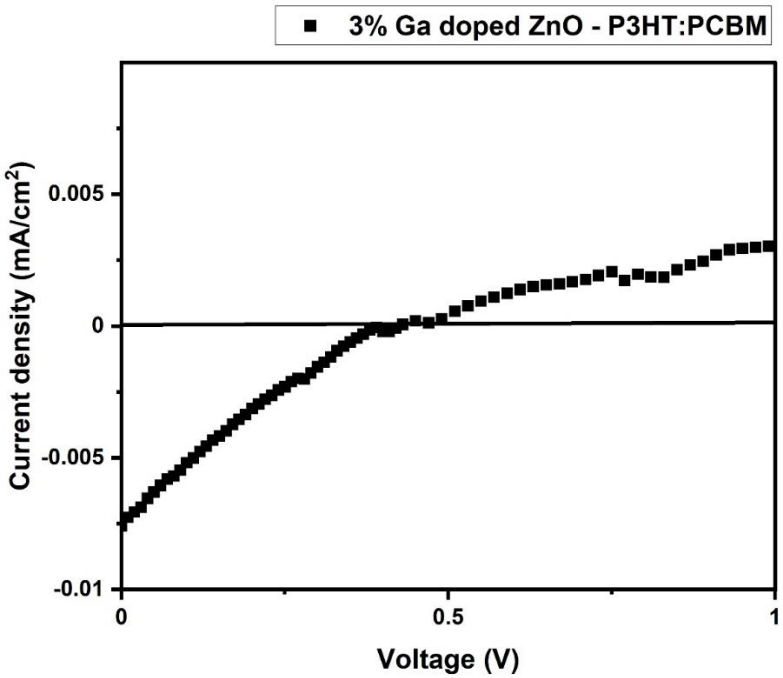

Figure 6.7. J-V curve for 3% Ga doped ZnO:P3HT:PCBM device

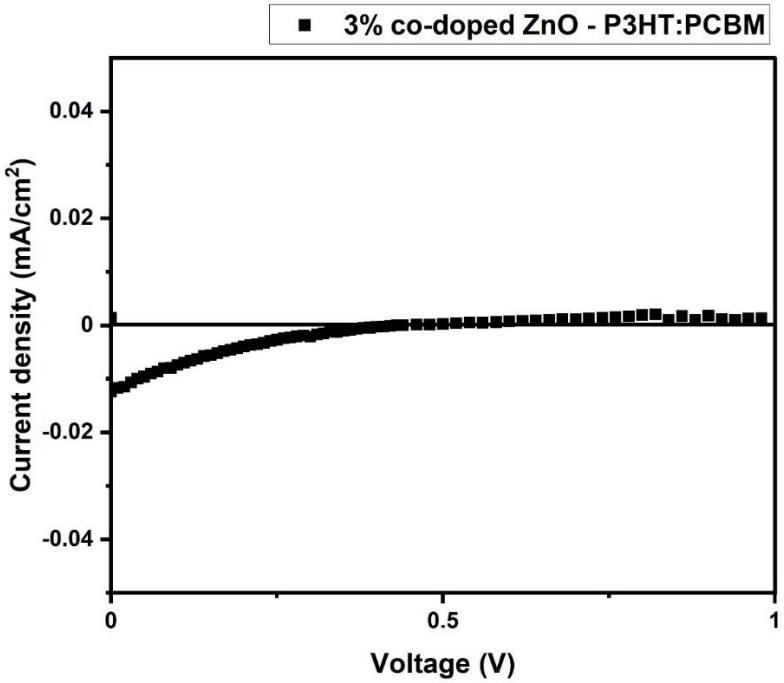

Figure 6.8. J-V curve for 3% co-doped ZnO:P3HT:PCBM device.

Table 6. 1. Summary of performance parameters for the fabricated devices

Device	J_{SC} *(mA/cm²)*	V_{OC} *(mV)*	R_S *KΩ cm²*	R_{Sh} *KΩ cm²*	*FF (%)*	*PCE (%)*
Ref.	**3.92 ± 0.01**	**440 ± 2**	**53.3 ± 0.4**	**357 ± 2**	**41.2 ± 0.6**	**7.02 ± 0.05**
Device						
ZnO	**0.195 ± 0.004**	**460 ± 2**	**5127.1 ± 1.2**	**893 ± 1.1**	**14.4 ± 0.2**	**0.13**
ZnO:Ga	**0.0075 ± 0.004**	**150 ± 2**	**17.3 ± 0.4**	**36.4 ± 0.2**	**22.4 ± 0.6**	**0.0062± 0.0004**
ZnO:Mg:Ga	**0.012 ± 0.002**	**150 ± 3**	**1177.2 ± 0.3**	**322.4 ± 1.1**	**15.4 ± 0.3**	**0.0008 ± 0.0002**

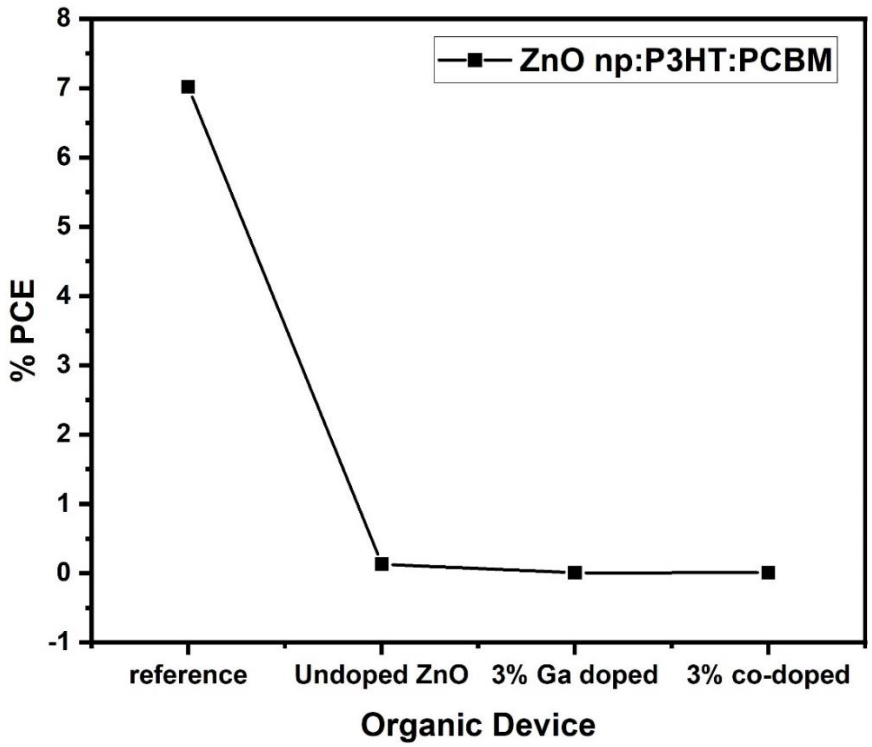

Figure 6.9. Power conversion efficiencies of the fabricated devices.

Conclusion

By incorporating doped ZnO nanoparticles in the active layer P3HT:PCBM blend, our aim was to improve the power conversion efficiencies in bulk hetero junction solar cells. However, it turned out that the incorporation of the nanoparticles affected the PCE values negatively and this was attributed to non-homogeneous distribution and poor exciton dissociation. Raman spectroscopy studies identified all modes of P3HT. Absorption measurements shows the greatest absorbance from the Mg,Ga/ ZnO in the visible region. The highest photoluminescence intensity was recorded from the Mg,Ga/ZnO device. Due to this device giving the lowest PCE and it is reasonable to conclude that Mg-Ga/ZnO nanoparticles acted as recombination centres for photoemission.

References

[1] S. R. Ferreira, R. J. Davis, Y. Lee, P. Lu, and J. W. P. Hsu, "Effect of device architecture on hybrid zinc oxide nanoparticle : poly (3-hexylthiophene) blend solar cell performance and stability," *Org. Electron.*, vol. 12, no. 7, pp. 1258–1263, 2011, doi: 10.1016/j.orgel.2011.04.008.

[2] S. Falke, P. Eravuchira, and C. Lienau, "Raman spectroscopic identification of fullerene inclusions in polymer / fullerene blends †," vol. 2011, no. May, pp. 1897–1900, 2011, doi: 10.1002/jrs.2966.

[3] J. M. Bell, P. Castrucci, M. De Crescenzi, and N. Motta, "Microscopic and Spectroscopic Investigation of Poly(3-hexylthiophene) Interaction with Carbon Nanotubes," no. December 2014, 2011, doi: 10.3390/polym3031433.

[4] M. Baibarac, M. Lapkowski, A. Pron, S. Lefrant, and I. Baltog, "SERS Spectra of Poly(3-Hexylthiophene) in Oxidized and Unoxidized States," *J. Raman Spectrosc.*, vol. 29, no. 9, pp. 825–832, 1998, doi: 10.1002/(sici)1097-4555(199809)29:9<825::aid-jrs309>3.0.co;2-2.

[5] E. Klimov, W. Li, X. Yang, G. G. Hoffmann, and J. Loos, "Scanning near-field and confocal Raman microscopic investigation of P3HT-PCBM systems for solar cell applications," *Macromolecules*, vol. 39, no. 13, pp. 4493–4496, 2006, doi: 10.1021/ma052590x.

[6] V. Saini *et al.*, "Electrical, optical, and morphological properties of p3ht-mwnt nanocomposites prepared by In situ polymerization," *J. Phys. Chem. C*, vol. 113, no. 19, pp. 8023–8029, 2009, doi: 10.1021/jp809479a.

[7] G. Louarn *et al.*, “Raman spectroscopic studies of regioregular poly(3-alkylthiophenes),” *J. Phys. Chem.*, vol. 100, no. 30, pp. 12532–12539, 1996, doi: 10.1021/jp960104p.

[8] F. Otieno *et al.*, “Improved efficiency of organic solar cells using Au NPs incorporated into PEDOT : PSS buffer layer,” vol. 085302, no. August 2017, 2018, doi: 10.1063/1.4995803.

[9] F. Otieno, B. K. Mutuma, M. Airo, K. Ranganathan, and R. Erasmus, “Enhancement of organic photovoltaic device performance via P3HT : PCBM solution heat treatment Enhancement of organic photovoltaic device performance via P3HT : PCBM solution heat treatment,” *Thin Solid Films*, vol. 625, no. January, pp. 62–69, 2017, doi: 10.1016/j.tsf.2017.01.047.

[10] G. L. Kabongo, P. S. Mbule, G. H. Mhlongo, B. M. Mothudi, and M. S. Dhlamini, “Time-resolved fluorescence decay and Gaussian analysis of P3HT-derived Ho 3 + - and Tm 3 + -doped ZnO nanostructures,” *Bull. Mater. Sci.*, 2020, doi: 10.1007/s12034-019-2020-0.

[11] N. A. Nismy, “Control of nanocrystal surface defects for efficient charge extraction in polymer-ZnO photovoltaic systems,” no. June 2014, 2012, doi: 10.1063/1.4751432.

[12] J. M. Kroon, M. M. Wienk, W. J. H. Verhees, and J. C. Hummelen, “Accurate efficiency determination and stability studies of conjugated polymer/fullerene solar cells,” *Thin Solid Films*, vol. 403–404, pp. 223–228, 2002, doi: 10.1016/S0040-6090(01)01589-9.

[13] C. J. Brabec, N. S. Sariciftci, and J. C. Hummelen, “Plastic Solar Cells,” *Adv. Funct. Mater.*, vol. 11, no. 1, pp. 15–26, Feb. 2001, doi: 10.1002/1616-3028(200102)11:1<15::AID-ADFM15>3.0.CO;2-A.

[14] J. Nelson, *The Physics of Solar Cells*. PUBLISHED BY IMPERIAL COLLEGE PRESS AND DISTRIBUTED BY WORLD SCIENTIFIC PUBLISHING CO., 2003.

[15] J. L. Huang, "Energy & Applications of ZnO in organic and hybrid solar cells," no. January 2021, 2011, doi: 10.1039/C1EE01873F.

[16] A. Smets, K. Jäger, O. Isabella, R. Swaaij, and M. Zeman, "Solar Energy: The Physics and Engineering of Photovoltaic Conversion, Technologies and Systems," *undefined*, 2016.

[17] F. C. Krebs, Y. Thomann, and R. Thomann, "A simple nanostructured polymer / ZnO hybrid solar cell - Preparation and operation in air," no. October, 2008, doi: 10.1088/0957-4484/19/42/424013.

Chapter 7 - Conclusions and Future Work

The crystal structure, particle morphology, optical, luminescence and magnetic properties of magnesium and gallium doped zinc oxide nanoparticles were investigated. Structural, optical, luminescence and efficiency parameters of organic solar cells incorporating the ZnO nanoparticles were also analyzed. Magnesium and gallium were chosen as dopants due to their unique abilities of improving the optical and electrical properties of ZnO. Tuning the properties of ZnO in this manner offers potential in improving power conversion efficiencies of organic photovoltaic devices that incorporate ZnO either as an electron transport layer or in hybrid devices where ZnO nanoparticles are added to the photoactive layer blend to facilitate electron extraction. Enhancing the magnetic properties of ZnO offers further benefits in potentially aiding exciton dissociation in OPV active layers.

XRD measurements confirmed that the synthesized powders are of the hexagonal wurtzite structure of ZnO. SEM studies confirmed powders to be made of rod-like structures agglomerated together to form nanoflowers and nanospheres. Elemental mapping studies showed elements to be distributed homogeneously over the nanoparticles while the elemental composition studies revealed the weight percentages of elements in the samples. Raman spectroscopy further confirmed all modes corresponding to hexagonal wurtzite structure of ZnO. Peak shifts and broadening was seen on incorporating Mg and Ga dopants into ZnO matrix. The band gaps energies of the samples determined from diffuse reflectance data were found to be in the range of 3.11 – 3.18 eV. A decrease in the band gap values was noticed as the samples were annealed from room temperature to 500°C. The decrease in these values was ascribed to increase in crystallinity which was confirmed from the XRD data.

Photoluminescence studies revealed similar spectral characteristics to those from literature with near band edge and broad band emissions in the visible region. This implies that emissions originate from similar defects transitions. These transitions broad band emissions were mostly due to oxygen related defects. Addition of dopants varied the emission properties, with the Ga doped sample predominately displaying near band edge emissions with minimal emission in the broad band. TEM images were consistent with SEM images showing that the particles together to form nanoflowers.

The ZnO nanoparticles were then incorporated into the active layer blend of the BHJ organic solar cells and the efficiency parameters were investigated. A large decrease in the PCE was seen upon introduction of the doped nanoparticles into the active layer blend. This drop was attributed to the nanoparticles causing cracks probably due to differing particle sizes of the nanoparticles and non-homogeneous distribution which form alternative pathways for current to flow in the device, and they can also affect the contact between the active layer and the top aluminum electrode. This was confirmed by low shunt and high series resistances determined from the J-V curves.The poor device performance was also attributed to ZnO nanoparticles that failed to completely dissolve in the chlorobenzene and thus formed hillocks and pinholes in the active layer of the device.

Future Work

The quality of ZnO incorporating Mg and Ga dopants can be improved by refining the synthesis methods, e.g. monitoring closely the reaction time homogenous and monodispersed particles. Also by monitoring the pH and temperature during the synthesis in order to achieve suitable morphology to improve harvesting of photogenerated charge carriers. More devices can be fabricated to promote the overall device repeatability as well as optimization of precursors in order to fabricate as many devices as possible in the cheapest possible way. The devices need to be fabricated in clean environment (like clean room) to avoid contamination and subsequent photo-degradation.

Doped ZnO has shown high potential owing to its excellent optoelectronic properties thus making it as a suitable candidate for charge transport and extraction. These dual functions are essential in the enhancement of the photoconversion efficiency of organic photovoltaic devices. We thus propose that the effect of ZnO addition as an acceptor in the hybrid device on the morphology and subsequently on the bulk heterojunction be investigated. This should follow the optimization of the mass ratio of ZnO and PCBM. Additionally, the suitable device architecture essentially in the inverted geometry should also be investigated in detail in which doped ZnO will be functionalized on the transparent conducting electrode (ITO) for efficient electron transport and hole blockade of the resulting PV device.